Development of Methods for Evaluation and Optimization of Chest Tomosynthesis

Angelica Svalkvist

Department of Radiation Physics, Institute of Clinical Sciences
Sahlgrenska Academy, University of Gothenburg
Gothenburg, Sweden, 2011

Doctoral Thesis, 2011
Department of Radiation Physics
Institute of Clinical Sciences at Sahlgrenska Academy
University of Gothenburg
SE-413 45 Gothenburg
Sweden

ISBN 978-91-628-8375-1
E-publication: http://hdl.handle.net/2077/26593
Printed in Sweden by
Geson Hylte tryck AB, Gothenburg 2011

"When you are a Bear of Very Little Brain, and you Think of Things, you find sometimes that a Thing which seemed very Thingish inside you is quite different when it gets out into the open and has other people looking at it."

-A.A. Milne

Development of Methods for Evaluation and Optimization of Chest Tomosynthesis

Angelica Svalkvist
Department of Radiation Physics, Institute of Clinical Sciences at Sahlgrenska Academy, University of Gothenburg, SE−413 45 Gothenburg, Sweden

Abstract

Tomosynthesis is a low-dose technique that has attracted increasing interest from the medical imaging community during the past decade. Tomosynthesis refers to the technique of acquiring a number of projection radiographs using extremely low exposure over a limited angular range, and using these radiographs to reconstruct slices of the imaged object. These reconstructed slices contain much less overlaying anatomical structures than conventional radiographs, which improves the possibility of obtaining relevant diagnostic information from the examination. The work described in this thesis concerns the development of methods for the evaluation and optimization of tomosynthesis for chest imaging.

Conversion factors between exposure and the resulting effective dose to the patient are available for established X-ray procedures. In the present work, corresponding conversion factors were determined for different chest tomosynthesis system configurations and patient sizes using the Monte Carlo technique. Using these conversion factors, the resulting effective dose from a tomosynthesis examination can be estimated using only information on the total exposure resulting from the examination.

According to the ALARA (as low as reasonably achievable) principle, all medical imaging should be performed using the lowest possible exposure of the patients to produce images of satisfactory diagnostic quality. To determine the lowest reasonably achievable exposure it is necessary to evaluate images acquired using various amounts of exposure. A method of simulating dose reduction in tomosynthesis was developed in this work. The method is based on the creation of a noise image that can be added to an image to simulate acquisition of the image at a lower dose. By using information about the noise power spectrum (NPS) of the system at different detector dose levels, and by establishing the relationship between pixel value and pixel variance as a function of dose, the noise image can be filtered with a frequency filter to obtain the correct NPS and pixel values. In this way, possible variations in detective quantum efficiency can be accounted for in the dose simulation process. Results from an evaluation of the method indicate that the method is appropriate for simulating dose reduction of tomosynthesis projection radiographs.

In order to thoroughly evaluate the performance of chest tomosynthesis in nodule detection, images containing nodules of different sizes and densities, located in different regions of the lung parenchyma, are needed. A method of simulating lung nodules in chest tomosynthesis was developed and evaluated. The method is based on the creation of three-dimensional artificial nodules that are inserted into the tomosynthesis projection images before reconstruction of the section images. The signal spread in the detector, the scattered radiation and patient motion were accounted for in the simulation process. The sensitivity for the simulated nodules was shown to be similar to that for real nodules, and experienced radiologists had difficulty in visually differentiating between real and simulated nodules. The nodule simulation method can be used to investigate the limitations in detection of lung nodules in chest tomosynthesis, without introducing any substantial bias compared to the use of clinical images.

ISBN: 978-91-628-8223-5
E-publication: http://hdl.handle.net/2077/26593

List of Papers

This thesis is based on the following four papers, which will be referred to in the text by their Roman numerals.

I. Svalkvist A, Månsson LG and Båth M
Monte Carlo simulations of the dosimetry of chest tomosynthesis
Radiat. Prot. Dosimetry 2010; 139(1-3): 144-152

II. Svalkvist A and Båth M
Simulation of dose reduction in tomosynthesis
Med. Phys. 2010; 37(1): 258-269

III. Svalkvist A, Håkansson M, Ullman G and Båth M
Simulation of lung nodules in chest tomosynthesis
Radiat. Prot. Dosimetry 2010; 139(1-3): 130-139

IV. Svalkvist A, Johnsson ÅA, Vikgren J, Håkansson M, Ullman G, Boijsen M, Fisichella V, Flinck A, Kheddache S, Molnar D, Månsson LG and Båth M
Evaluation of an improved method of simulating lung nodules in chest tomosynthesis
Submitted

Preliminary results have been presented at

Svalkvist A, Ullman G, Håkansson M, Dance DR, Sandborg M, Alm Carlsson G and Båth M
Investigation of the effect of varying scatter-to-primary ratios on nodule contrast in chest tomosynthesis
Presented at SPIE Medical Imaging 2011: Physics of Medical Imaging, February 12-17, 2011, Orlando, Florida, USA

Svalkvist A, Håkansson M, Ullman G and Båth M
Nodule simulation in chest tomosynthesis
Presented at the Third Malmö Conference on Medical Imaging, June 25-27, 2009, Malmö, Sweden

Svalkvist A and Båth M
Improved method of simulating dose reduction for digital radiographic systems
Presented at the Third Malmö Conference on Medical Imaging, June 25-27, 2009, Malmö, Sweden

Svalkvist A, Månsson LG and Båth M
Monte Carlo simulations of the dosimetry of chest tomosynthesis
Presented at the Third Malmö Conference on Medical Imaging, June 25-27, 2009, Malmö, Sweden

Svalkvist A, Zachrisson S, Vikgren J, Johnsson ÅA, Flinck A, Boijsen M, Kheddache S, Månsson LG and Båth M
Chest tomosynthesis at Sahlgrenska University Hospital: current research activities
Presented at the Tomosynthesis Imaging Symposium, April 30 to May 2, 2009, Durham, North Carolina, USA

Svalkvist A, Zachrisson S, Månsson LG and Båth M
Investigation of the dosimetry of chest tomosynthesis
Presented at SPIE Medical Imaging 2009: Physics of Medical Imaging, February 8-12, 2009, Orlando, Florida, USA

Contents

Abstract ..... **v**

List of Papers ..... **vii**

Contents ..... **ix**

Abbreviations ..... **xi**

1 Introduction **1**

1.1 Historical background of tomosynthesis 2
1.2 Chest tomosynthesis today 4
1.2.1 Commercially available chest tomosynthesis systems *4*
1.2.2 Research in the field of chest tomosynthesis *5*
1.3 Evaluation of medical imaging systems 9
1.4 Hybrid images 10
1.5 Motivation for the studies included in this thesis 10

2 Aims **13**

3 The GE tomosynthesis system **17**

4 Dosimetry **23**

4.1 Operational dose quantities 23
4.1.1 Kerma *23*
4.1.2 Energy imparted *24*
4.1.3 Absorbed dose *24*
4.1.4 Incident air kerma *24*
4.1.5 Entrance surface air kerma *25*
4.1.6 Air kerma-area product *25*
4.2 Risk-related dose quantities 25
4.2.1 Equivalent dose *26*
4.2.2 Effective dose *26*
4.2.3 Determination of the risk-related dose quantities *29*
4.3 The PCXMC software 30
4.3.1 Mathematical phantoms *30*
4.3.2 Monte Carlo simulations *31*
4.3.3 Dose calculations *32*
4.4 Conversion factors 32
4.5 Previous work on the dosimetry of chest tomosynthesis 33
4.6 Summary of Paper I 34
4.6.1 Background *34*
4.6.2 Description of the method *34*
4.6.3 Results *35*

5 Simulated dose reduction 41

5.1 Introduction to linear systems theory 42
5.1.1 The Fourier transform 43
5.1.2 The sampling theorem and aliasing 43
5.2 Metrics of system performance 43
5.2.1 Modulation transfer function 44
5.2.2 Noise power spectrum 44
5.2.3 Detective quantum efficiency 45
5.3 Previous work on simulated dose reduction in digital radiographic imaging 46
5.4 Summary of Paper II 48
5.4.1 Background 48
5.4.2 Theory 49
5.4.3 Validation 52
5.4.4 Step-by-step description of the simulated dose reduction method 56

6 Nodule simulation 61

6.1 Nodule characteristics 62
6.2 Scattered radiation in chest radiography imaging 64
6.3 MTF measurements 66
6.4 Receiver operating characteristics 70
6.5 Previous work on the simulation of lung nodules 72
6.6 Summary of Paper III 74
6.6.1 Background 74
6.6.2 Description of the method 75
6.6.3 Results 77
6.7 Short summary of Paper IV 79
6.7.1 Background 79
6.7.2 Improvements of the method 79
6.7.3 Evaluation of the method 81
6.7.4 Results 84

7 Discussion and future work 89

7.1 Dosimetry 89
7.2 Simulated dose reduction 92
7.3 Nodule simulation 96
7.4 Overall discussion of the work 100
7.5 Future work 102

8 Summary and conclusions 105

Acknowledgements 109

References 113

Abbreviations

A_z	Area under the receiver operating characteristics curve
AEC	Automatic exposure control
AFC	Alternative forced choice
AFROC	Alternative free-response receiver operating characteristics
ALARA	As low as reasonably achievable
CT	Computed tomography
DICOM	Digital Imaging and Communication in Medicine
DQE	Detective quantum efficiency
E	Effective dose
E_{KAP}	Conversion factor between kerma-area product and effective dose
FPD	Flat-panel detector
FPF	False positive fraction
FROC	Free-response receiver operating characteristics
FSD	Focal-spot-to-surface (skin) distance
FT	Fourier transform
HVL	Half-value layer
IAEA	International Atomic Energy Agency
ICRP	International Commission on Radiological Protection
ICRU	International Commission on Radiation Units and Measurements
IEC	International Electrotechnical Commission
IRF	Impulse response function
K_i	Incident air kerma
KAP	Kerma-area product
LAT	Lateral
LLF	Lesion localisation fraction
LNT	Linear non-threshold
LSA	Linear systems analysis
LSF	Line spread function
LST	Linear systems theory
MAFC	Multiple-alternative forced choice
MTF	Modulation transfer function
NEQ	Noise-equivalent number of quanta
NLF	Non-lesion localisation fraction
NNPS	Normalized noise power spectrum

NPS	Noise power spectrum
NRPB	National Radiological Protection Board
P_{KA}	Air kerma-area product
PA	Posterioanterior
PCXMC	PC program for X-ray Monte Carlo
PSF	Point spread function
RBE	Relative biological effectiveness
ROC	Receiver operating characteristics
ROI	Region of interest
SF	Scatter fraction
SID	Source-to-image distance
SNR	Signal-to-noise ratio
SPR	Scatter-to-primary ratio
STUK	Radiation and Nuclear Safety Authority in Finland
TNF	True negative fraction
TPF	True positive fraction

1 Introduction

Chest radiography is one of the most common radiological examinations performed at hospitals around the world. At the thoracic section at the department of radiology, Sahlgrenska University Hospital, Gothenburg, Sweden, approximately 50 000 chest radiography examinations are performed each year. The main advantages of chest radiography are that it is a cost-effective procedure, the examination time is short and the technique is widely available [1, 2]. An instant overview of the patient's cardiopulmonary status can be obtained, with the benefit that pneumothorax, pneumonia or pulmonary oedema, for example, can be easily diagnosed and the appropriate treatment instigated. However, it has long been known that conventional projection radiography suffers from limitations in detectability due to overlapping anatomy [3-11]. The introduction of computed tomography (CT) in the 1970s provided a solution to this problem. Since the introduction of CT, many of the developments in medical imaging have been focused on increasing the diagnostic information that can be obtained from an examination. These developments have, however, led to a steady increase in the radiation exposure to the population resulting from diagnostic procedures [12-14].

The International Commission on Radiation Protection (ICRP) states that all radiological exposures should be performed following the "As Low As Reasonably Achievable" (ALARA) principle [15]. According to this principle, medical imaging should be performed in such way that the image quality required for correct diagnosis is obtained using the lowest possible radiation exposure of the patient, taking into account economic and societal factors. In order to fulfil the ALARA principle diagnostic systems must be optimized. Diagnostic optimization should however not only include the evaluation of image quality vs. exposure, but also which radiological procedure is most suitable for a specific diagnostic purpose. In the past, not very many alternatives for different radiological procedures were available, and optimization processes were thus focused on reducing the patient exposure of the existing radiological procedures. The introduction of new techniques has, however, led to greater opportunities for more complex optimization processes in medical imaging.

Tomosynthesis is a low-dose technique that has attracted increasing interest from the medical imaging society during the past decade. Tomosynthesis refers to the technique of acquiring a number of projection radiographs, using extremely low exposure for each radiograph, over a limited angular range and using these radiographs to reconstruct sections of the imaged object. These reconstructed section images contain much less of the overlaying anatomical structures than conventional radiographs, which leads to increased possibilities for obtaining relevant diagnostic

information from this kind of examination. The work described in this thesis concerns the development of methods for the evaluation and optimization of tomosynthesis for chest imaging. In the next section, the historical background of tomosynthesis is given, followed by a review of the implementation of tomosynthesis for chest imaging.

1.1 Historical background of tomosynthesis

Many of the radiological examinations performed today are based on the production of three-dimensional images of the human body. Webb [16] provides a thorough description of the history of tomographic section imaging. The first documents describing the production of section images were published at the beginning of the 1920s. In 1921, André Edmond Marie Bocage applied for a French patent on a technique that came to be known as *planigraphy*. The technique was based on the principle that the X-ray tube and detector move in parallel planes during exposure (using linear, circular or spiral motion), so that points within a given plane parallel to the X-ray tube and detector remain in focus, while points in all other planes in the volume are blurred. Although the French patent is the first on section imaging, the Dutch researcher Bernard Ziedses des Plantes claims that he invented the method independently in 1921, but he did not publish his work until 1931. It was later discovered that Ziedses des Plantes actually submitted his idea to a röntgenologist in 1921, but was told that the method was of no interest or use. The question of who should be recognised as being the inventor of section imaging, today known as tomography, thus remains unresolved. Bocage registered the first patent of the method, while Ziedses des Plantes was the first person to actually perform experimental work on section imaging [16].

For the first time in history it was now possible to obtain three-dimensional images of the interior of the human body, and tomography was therefore quickly adopted by the medical community. However, tomography had two obvious drawbacks [16]. First, in order to visualize additional planes in the volume the exposure procedure needed to be repeated. In many cases, this resulted in high levels of X-ray exposure to the patients. The second drawback was that, although the tomographic images contained less overlaying and obscuring anatomy than conventional X-ray images, it was not possible to completely suppress out-of-plane details.

Regarding the first drawback, already in a paper by Ziedses des Plantes from 1932 [17], it is mentioned that section images at different depths in a volume may be obtained simultaneously from one single image acquisition. According to Ziedses des Plantes, this could be achieved by acquiring a number of separate radiographs of the object from different angles. Upon summing these separate radiographs, one specific plane in the object will be in focus, while all the other planes will be blurred. However, section images from different depths in the object can be obtained by

shifting these radiographs relative to each other before each summation, see Figure 1.1. This technique is referred to as shift-and-add and can also be interpreted as unfiltered backprojection. Bernard Ziedses des Plantes further described this technique in his doctoral thesis in 1934 [18]. In 1969 Garrison et al. [19] implemented the technique described by Ziedses des Plantes by building a prototype called three-dimensional roentgenography. The prototype was used to produce section images of a chimpanzee's scull and showed promising results, although the resolution was reported to be limited. Regarding the second drawback, Garrison et al. also mentioned that the disturbing effects of out-of-plane objects could possibly be further reduced by appropriate image processing.

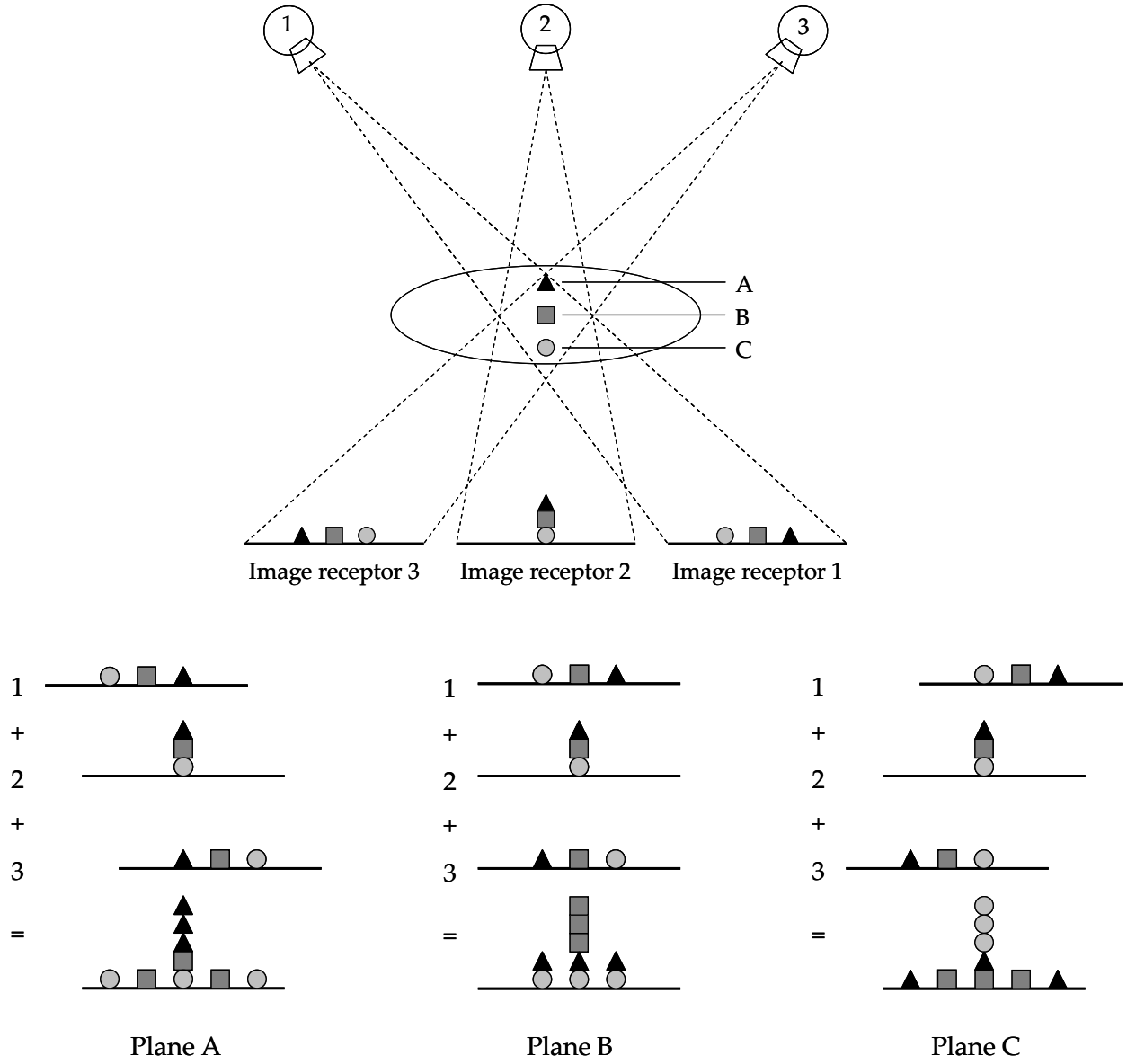

Figure 1.1 Illustration of the shift-and-add technique. By shifting the acquired projection images relative to each other before summation, objects from different planes in the patient will be in focus while objects in other planes will be smeared out.

In the early 1970s both Miller et al. [20] and Grant et al. [21] presented papers describing successful experiments producing an arbitrary number of section images of a volume using a fixed number of angular projection images of the object. Grant et al. also introduced the term 'tomosynthesis', which originates from the Greek words 'tomo' (meaning cut, slice or section) and 'synthesis' (meaning the combining of separate elements or substances to form a coherent whole). In the 1970s and 1980s much of the research in the area of tomosynthesis was focused on improving image quality (mainly by the reduction of anatomical blur caused by objects outside the plane of interest), and shortening examination times. A summary of tomosynthesis research during the 1970s and 1980s is given by Dobbins and Godfrey [22]. The introduction of CT in the 1970s had, however, resulted in decreasing interest in the development of tomosynthesis. Suddenly, the advantages of tomosynthesis over conventional tomography had been surpassed by CT, and the benefits of tomosynthesis in clinical practice were no longer obvious. The introduction of flat-panel detectors (FPDs) in the 1990s became a landmark in the history of tomosynthesis. Combining modern FPDs with modern computer technology solved the problems of poor image quality and long examination times that researchers in the field of tomosynthesis had been struggling with for decades. Using FPDs enable high-quality images to be obtained using high readout rates, while modern computer technology allows the use of new reconstruction technologies and image post-processing routines. These advantages, combined with increased dose awareness, awakened a new interest in tomosynthesis.

1.2 Chest tomosynthesis today

1.2.1 Commercially available chest tomosynthesis systems

One of the commercially available chest tomosynthesis systems is the GE Definium 8000 system with VolumeRAD option (GE Healthcare, Chalfont St. Giles, UK). A beta version of this system was installed at Sahlgrenska University Hospital in December 2006, and in September 2007 the prototype was replaced by the fully commercial product. The GE Definium 8000 system is, in its original construction, designed for planar digital radiographic imaging. The VolumeRAD option includes the implementation of tomosynthesis software. During a tomosynthesis examination using this system, the detector is stationary while the X-ray tube performs a continuous vertical motion to acquire multiple projection images of the patient from various angles. These projection images are then used to reconstruct tomosynthesis section images of the patient. As all the studies described in this thesis are based at least partly on the use of the GE tomosynthesis system, a thorough description of the system is given in Chapter 3.

Another commercially available chest tomosynthesis system is the SonialVision Safire system (Shimadzu Co., Kyoto, Japan). This system was originally designed as a digital fluoroscopy system with the additional option of tomosynthesis technology. The detector is mounted under the patient table. The table can be tilted, allowing for examinations of the patient standing up, inclined against the table, or lying down on the table. The tomosynthesis projection images are acquired by moving the X-ray tube and image detector linearly, in opposite directions. In this way, multiple projection images are acquired, which are then reconstructed to provide section images of the patient.

1.2.2 Research in the field of chest tomosynthesis

Many studies have been presented in the field of chest tomosynthesis in recent years. As the GE Definium 8000 system with VolumeRAD option was the first commercially available system, most of the clinically related research studies have been performed using this system [23-26]. Many of these studies focused on comparing the detectability of lung nodules with chest tomosynthesis and chest radiography, using CT as a reference. Dobbins et al. [27] and Yamada et al. [28] presented similar studies. Dobbins et al. used an in-house constructed tomosynthesis prototype system, while Yamada et al. [28] used the SonialVision Safire tomosynthesis system from Shimadzu.

Apart from these kinds of comparative studies, a study has been conducted to determine if additional clinical experience in chest tomosynthesis affects the possibility of fully exploiting the benefits of the technique [29]. Another study investigated the extent to which a learning session was beneficial to radiologists with limited experience of chest tomosynthesis, and also identified potential pitfalls in nodule detection using chest tomosynthesis [30]. An initial evaluation of the possibility of using chest tomosynthesis instead of CT for follow-up of lung nodules has also been presented [31]. This study was based on the evaluation of nodule size measurements in chest tomosynthesis, compared to those in CT.

As well as investigations of the clinical benefits of tomosynthesis, two studies focusing on the evaluation of the effective doses to patients from chest tomosynthesis and chest radiography examinations performed using the GE Definium 8000 system with VolumeRAD option have been published [32, 33]. In addition to the above-mentioned research studies, a number of review articles on tomosynthesis have been published [22, 34-37]. Below, short summaries of the studies related to lung nodule detection and lung nodule measurements using tomosynthesis are given. Short summaries of the studies on the effective doses resulting from chest tomosynthesis examinations are given in Section 4.5.

Studies related to lung nodule detection

Dobbins et al. presented a study aiming at investigating the visibility of lung nodules in chest tomosynthesis [27]. In the study 21 patients, with a total of 175 lung nodules in the size range 3-15 mm, were included. Two chest radiologists were given the task of identifying lung nodules found using CT, on chest radiography and chest tomosynthesis images. The results revealed that of all the nodules identified using CT, 22 % were visible in the chest radiography images, while the corresponding fraction was 70 % in chest tomosynthesis images. These results indicate that the detection of pulmonary nodules is increased when using chest tomosynthesis instead of chest radiography when performing a chest examination.

Vikgren et al. evaluated the performance of chest tomosynthesis by comparing the detectability and the visibility of lung nodules with this method and chest radiography [23]. A total of 89 patients were included in the study, in which nodules were identified in 42 patients. The remaining 47 patients were included in the study as normal cases. In total, the patient material included 131 lung nodules of various sizes. In the detection study four experienced chest radiologists were given the task of identifying suspicious lung nodules in the images. The results revealed that only 16 % of the nodules were detected using chest radiography, while the corresponding fraction using chest tomosynthesis was 56 %. In the comparison of nodule visibility it was found that 28 % of the nodules could be identified in retrospect in the chest radiography images, while almost all the nodules (92 %) were retrospectively visible in the chest tomosynthesis images. The conclusion drawn from this study was that chest tomosynthesis has superior sensitivity to chest radiography in detecting lung nodules.

Based on the results presented by Vikgren et al. [23], which were obtained only a short while (6 months) after the tomosynthesis system had been installed at the hospital, Zachrisson et al. [29] investigated whether the detectability of pulmonary nodules improved as a result of clinical experience of the system. The same tomosynthesis images as used by Vikgren et al. were used in this study (89 patients with a total of 131 lung nodules). Three of the observers who had participated in the first study by Vikgren et al. re-examined the images, with the same task of identifying suspicious lung nodules. The detectability of lung nodules obtained in this second examination of the images was then compared with the detectability reported by Vikgren et al. No statistical differences in detectability were found between the two readings. This indicates that experienced thoracic radiologists are able to exploit the benefits of chest tomosynthesis for nodule detection already after a few months of clinical experience with the technique.

As a follow-up to the study by Zachrisson et al. [29], Asplund et al. investigated the effects of learning with feedback on the detection of lung nodules in chest tomosynthesis [30]. Potential pitfalls regarding the detection of lung nodules were also

identified. Six observers with various degrees of experience in chest tomosynthesis participated in the study. Of these, three were the same as those participating in the studies by Vikgren et al. [23] and Zachrisson et al. [29]. The same patient images as used in the previous studies by Vikgren et al. and Zachrisson et al. were used (89 patients with a total of 131 lung nodules). In addition, a smaller patient material, consisting of 25 patients with a total number of 31 lung nodules, was used for a learning session. After initial evaluation of the large patient material, in which suspicious nodules were identified, all six observers individually evaluated the patient images included in the learning session. The results from the evaluations of the smaller patient material were shown to the observers together with the corresponding CT images of the patients in a collective learning session. During the learning session, all real nodules found in the patient material and additional nodules falsely identified by any of the observers during individual evaluations were evaluated and discussed. Reasons for missed true lesions and false positive markings were analysed. After the learning session, the observers once again evaluated the large patient material with the purpose of investigating whether the learning session had improved the detectability of lung nodules using chest tomosynthesis. The results revealed no significant difference in detectability resulting from the learning session for experienced observers, while a significant improvement was found for the most inexperienced readers. It was thus concluded that inexperienced observers might benefit from learning with feedback regarding the task of nodule detection using chest tomosynthesis. The main pitfalls identified during the learning session were related to the area close to the pleura, in which it was difficult to distinguish between pleural and pulmonary nodules. The reason was concluded to be the limited depth resolution of the tomosynthesis images.

Quaia et al. presented a study with the aim of investigating the value of chest tomosynthesis in the diagnosis of suspected lung nodules [24]. A total of 228 patients, all with nodule-suspected findings on chest radiography images, were included in the study. All patients underwent additional chest tomosynthesis and CT examinations. Two experienced radiologists analysed the CT examinations and found a total of 180 lung nodules in 157 of the 228 patients included in the study. The remaining 71 patients were diagnosed as normal. The two radiologists who had initially reported suspected nodules in the 228 chest radiography examinations also analysed the tomosynthesis examinations. Based on the chest radiography examinations 110 (observer 1) and 123 (observer 2) of the 180 nodules were diagnosed correctly according to the CT findings. After also analysing the chest tomosynthesis images, a total of 156 (observer 1) and 160 (observer 2) of the 180 nodules were correctly diagnosed. The nodules that were not diagnosed correctly based on chest tomosynthesis were extrapulmonary nodules that were misinterpreted as pulmonary nodules, and pulmonary nodules that were misinterpreted as pleural changes.

Kim et al. [25] also presented a study comparing the performance of chest tomosynthesis to that of chest radiography. A total number of 100 patients were included in the study, of which 65 had a known mycobacterial disease. Two chest radiologists independently analysed the chest radiography and chest tomosynthesis images, with instructions to indicate findings of mycobacterial disease in the images. The observers were also instructed to record the characteristics of the found mycobacterial disease (bronchiolitis, nodules, consolidation, cavities and volume loss). The observers later matched and compared their findings with information obtained from CT images. It was found that the percentage detection for mycobacterial disease was 97 % (observer 1) and 99 % (observer 2) using chest tomosynthesis, and 89 % (observer 1) and 93 % (observer 2) using chest radiography. A separate analysis of the fraction of cavities detected using the two methods revealed that, on average, only 19 % of the cavities were detected in chest radiography, while 77 % were detected using chest tomosynthesis. It was thus concluded that chest tomosynthesis is superior to chest radiography for the detection of cavities, in patients with known mycobacterial disease.

The performance of chest tomosynthesis in the detection of lung nodules in patients with known colorectal malignancy was evaluated by Jung et al. [26]. In total, 142 patients who had undergone surgical resection of the colon were included in the study. All the patients were examined using chest radiography, chest tomosynthesis and chest CT. Two chest radiologists evaluated the CT images and created a reference, while two other chest radiologists were given the task to identify and mark nodules in the chest radiography and chest tomosynthesis images. They found that the percentage detection for lung nodules using chest radiography was only 27 %, while the percentage detection using chest tomosynthesis was three times higher (83 %). Based on these results the authors concluded that chest tomosynthesis is a sensitive technique that is comparable to chest CT for lung nodule detection.

The benefits of the SonialVision Safire tomosynthesis system for the detection of lung nodules, compared to chest radiography, was presented by Yamada et al. [28]. In total 116 patients where included in the study. Of these, 57 patients had a total number of 117 nodules in the lung parenchyma. Three radiologists evaluated the images and were instructed to mark suspicious lung nodules in the images. The results showed that 79 % of the lung nodules were detected using tomosynthesis, while the corresponding fraction using chest radiography was only 37 %. It was thereby concluded that the diagnostic performance of tomosynthesis was significantly superior to that of chest radiography.

A study related to lung nodule measurements

The possibility of using tomosynthesis to measure the size of nodules was investigated by Johnsson et al. [31]. A Polylite® phantom with embedded spheres of various sizes and densities, developed by Svahn et al. [38], was used in the study. The phantom was scanned using both a CT and a chest tomosynthesis system. Six observers, blinded to the true sphere diameters, independently measured the diameters of the spheres in both the CT and tomosynthesis images. The results revealed no significant difference in measurement accuracy between the two techniques. The results thereby indicate that nodule size measurements could be made using tomosynthesis as an alternative to CT.

1.3 Evaluation of medical imaging systems

When evaluating an imaging system, many different measures can be used to compare the performance of one system to that of others. One way to evaluate an imaging system, and compare it to other systems available, is to perform measurements of its physical capacity. The most commonly used measure for physical image quality is the detective quantum efficiency (DQE) [39], which is a measure of the efficiency of signal transfer through a system. The determination of DQE is based on linear systems theory (LST) and includes measurements of both the resolution and noise properties of the system (for more information, see Section 5.2).

Although the DQE can be used to compare the signal transfer in one system with that of another, the connection between DQE and a clinically useful image quality is not obvious. The quality of the final clinical image will depend not only on the detector properties, but also, for example, on the image processing and the observer interpretation of the images. For example, using chest radiography images acquired with different systems, Sund et al. showed that the differences in image processing had a greater impact on clinical image quality than the difference in the DQE of the systems [40]. In addition, many studies have shown that it is the anatomical background, rather than the system noise, that limits the detection of pathology in clinical images [4-6, 8, 10, 11]. It can, therefore, be argued that the DQE is not a relevant measure when comparing the clinical usefulness of different imaging systems. This will especially be the case if the systems that are to be compared have different amounts of anatomical background present in the final clinical images.

From the summaries of the research studies on chest tomosynthesis given in Section 1.2.2, it is clear that observer performance studies are commonly used in the clinical evaluation of a new imaging technology. In an observer performance study, images from different systems are acquired and shown to a number of observers. The task assigned to the observers may differ between different studies. In a receiver operating characteristics (ROC) study, images with both normal and abnormal

findings are included. The observers participating in the ROC study are given the task of identifying the abnormal cases and grading the confidences of their answers. In an alternative forced choice (AFC) study, two or more images at a time are presented to the observers, who are given the task to determine in which of the images a signal is present. As an alternative to the observer performance studies, a study based on visual grading can be performed. In a visual grading study the observers are asked to grade the reproduction of different anatomical structures in the images according to either predefined quality criteria or in comparison to a given reference. A recent review of ROC and visual grading is given by Båth [41], while a recent review of AFC is given by Burgess [42].

1.4 Hybrid images

The most clinically relevant results from an observer performance study are obtained when clinical images are used [43, 44]. However, it may be difficult to acquire a clinical material that fulfils the desired requirements for study inclusion. Also, in studies aiming at optimizing the radiation exposure for an examination, repeated exposure of the patients participating in the study may be called for, which leads to more complex ethical considerations. The use of so-called hybrid images has proven to be a valuable complement to clinical images in such cases [5-7, 10, 11, 45-47].

In medical imaging, a hybrid image is commonly an anatomical image that has been modified, for example, by the addition of artificial noise or by the addition of simulated pathology. In order to obtain a clinically valid result from a study using hybrid images, it is important that the hybrid images in a realistic way reflect the clinical situation. Therefore, the method used to create the hybrid images should be thoroughly evaluated to ensure that the final hybrid images match the visual appearance of anatomical structures and the detectability of pathology found in real clinical images.

The methods used for the creation of the hybrid images are largely dependent on the imaging modality of interest. Hence, the methods used to create hybrid images in the case of CT differ from those used in conventional radiography. In many ways, tomosynthesis can be seen as a mixture of CT and conventional radiography and it is therefore not obvious which methods are most suitable to use in the case of tomosynthesis.

1.5 Motivation for the studies included in this thesis

As described in Section 1.2.2 above, many studies investigating the potential, limitations and usefulness of chest tomosynthesis have been performed in recent years. The results reveal that chest tomosynthesis is a promising technique. Compared to conventional chest radiography, chest tomosynthesis seems to have the

potential of improving the diagnostic outcome from a chest examination. It can thus be anticipated that the number of chest tomosynthesis examinations performed at hospitals around the world will increase in the future. For established X-ray procedures, such as chest radiography and chest CT examinations, conversion factors between a known exposure measure and the resulting effective dose to the patient have been established [48, 49]. These conversion factors can be used to translate a given exposure from the examination to an approximate effective dose to the patient. In order to more easily compare the effective doses from chest examinations using different technologies, a corresponding conversion factor for chest tomosynthesis would be beneficial. This forms the motivation of the study presented in Paper I.

According to the ALARA principle, all medical imaging should be performed using the lowest possible exposure of the patients needed to produce images of satisfactory diagnostic quality. Hence, an optimization of the examination should be performed, in which the optimum relationship between radiation exposure and image quality is determined. In order to perform such an optimization, observer performance studies may be conducted. As described in Section 1.4, the validity of the results from such studies will be higher if clinical images are used. However, in order to optimize the relationship between exposure and image quality, images acquired using various amounts of exposure are needed. The quest of acquiring clinical images using various amounts of exposure might be difficult to motivate, as additional and clinically unnecessary exposure of patients will be needed. Methods for simulating that an examination has been performed using lower exposure have previously been presented for conventional radiography [50-52] and CT [53-57]. As a tomosynthesis examination consist of the acquisition of a large number of projection images, it might be anticipated that the methods described for conventional radiography could be valid also in the case of tomosynthesis. However, the methods described for conventional chest radiography may be based on assumptions that might not be valid at the low exposure rates that are used in the acquisition of each of the tomosynthesis projection images. Hence, previously described methods for simulating reduction of exposure may need modifications to be valid for use in the case of tomosynthesis. This is the subject of Paper II.

Many of the studies on chest tomosynthesis have been focused on comparing the detectability of lung nodules between chest radiography and chest tomosynthesis, using chest CT as a reference. However, in order to thoroughly evaluate the performance of chest tomosynthesis in nodule detection, the possibility control the sizes, densities and locations of lung nodules would be desirable. The desired requirements of nodule characteristics may be difficult to fulfil using clinical images. Furthermore, it may be difficult to determine the exact size and density of real nodules. A number of methods of simulating lung nodules have been described previously [7, 58-60]. However, the approach used for nodule simulation is largely dependent on the imaging technique to be investigated. In conventional chest

radiography the shape of the simulated nodules is of less importance than the contrast, as overlaying anatomy will obscure the exact delineation of the simulated nodule. In the case of CT, where most overlapping anatomy is removed, it is important to consider the shapes of the simulated nodules, while the linear relationship between pixel value and density facilitates the simulation of nodule density. As chest tomosynthesis may be described as a combination of conventional radiography and CT, the most suitable method to use for the simulation of lung nodules in chest tomosynthesis is not obvious. This is the topic of interest in Papers III and IV.

2 Aims

The overall aim of the work described in this thesis was to develop methods for the evaluation and optimization of chest tomosynthesis. This work included the development of a simplified method to estimate effective doses from chest tomosynthesis examinations, and the development of methods for the creation of hybrid images that can be used for both the evaluation of chest tomosynthesis and the optimization of radiation exposure.

The aims of the separate studies were:

- to investigate the dosimetry of chest tomosynthesis and to determine conversion factors between the kerma-area product and effective dose for various system configurations and patient sizes (Paper I);

- to modify a previously described method of simulating dose reduction so that variations in DQE can be taken into account, thereby making the method more suitable for simulating dose reduction in tomosynthesis images (Paper II); and

- to develop a suitable method of simulating lung nodules in clinical chest tomosynthesis images (Papers III and IV), and to evaluate the method by comparing the detectability and visual appearance of the simulated nodules with those of real, clinically observed lung nodules (Paper IV).

As previously mentioned, all the studies are partly based on the GE tomosynthesis system. A detailed description of this system is therefore given in Chapter 3. Chapters 4 to 6 provide a thorough background to each of the studies performed. Each chapter includes a review of the important concepts and methodologies related to each study, a description of previous research in the area, as well as a summary of each paper.

"So perhaps the best thing to do is to stop writing Introductions and get on with the book."

-A.A. Milne

3 The GE tomosynthesis system

A prototype of the GE Definium 8000 system with VolumeRAD option was installed at the Sahlgrenska University Hospital, Gothenburg, Sweden, in December 2006, and was replaced by the commercial product in September 2007. Ever since the installation of the system, research aiming at evaluating chest tomosynthesis has been conducted at the hospital. Both the method of simulating dose reduction in tomosynthesis (Paper II) and the method of simulating nodules in chest tomosynthesis (Papers III and IV) were validated using this system.

The system was originally designed for planar digital radiographic imaging, but software for performing tomosynthesis image acquisition and reconstruction has been implemented, i.e., the VolumeRAD option. The system is designed with a stationary caesium iodide, flat-panel detector, with 2022×2022 pixels and a pixel size of 0.2×0.2 mm^2.

A conventional chest radiography examination includes both a posterioanterior (PA) image and a lateral (LAT) image of the chest. Using the pre-defined settings of the GE system at Sahlgrenska University Hospital, the acquisition of both the PA and LAT images are acquired using a source-to-image distance (SID) of 180 cm and automatic exposure control (AEC). The tube voltage (kV) used for the acquisition of the PA projection image is 125 kV, and a total filtration of 3 mm Al + 0.1 mm Cu is used. The LAT image is acquired using a tube voltage of 140 kV and a total filtration of 3 mm Al + 0.2 mm Cu. The chest tomosynthesis examination is performed using the same patient setup as for a conventional chest PA projection image, but in the case of a tomosynthesis examination the X-ray tube performs a continuous vertical motion, acquiring 60 projection images in the angular interval of ±15° during a time period of approximately ten seconds. During the vertical motion of the X-ray tube the tube is rotated around its own axis so that the central axis of the X-ray beam always passes through the pivot point, which is located 9.9 cm in front of the detector surface (Figure 3.1). Also the collimation of the X-ray field is adjusted during the image acquisition to compensate for the increased field size at the detector surface for the oblique incident angles of the X-ray beam.

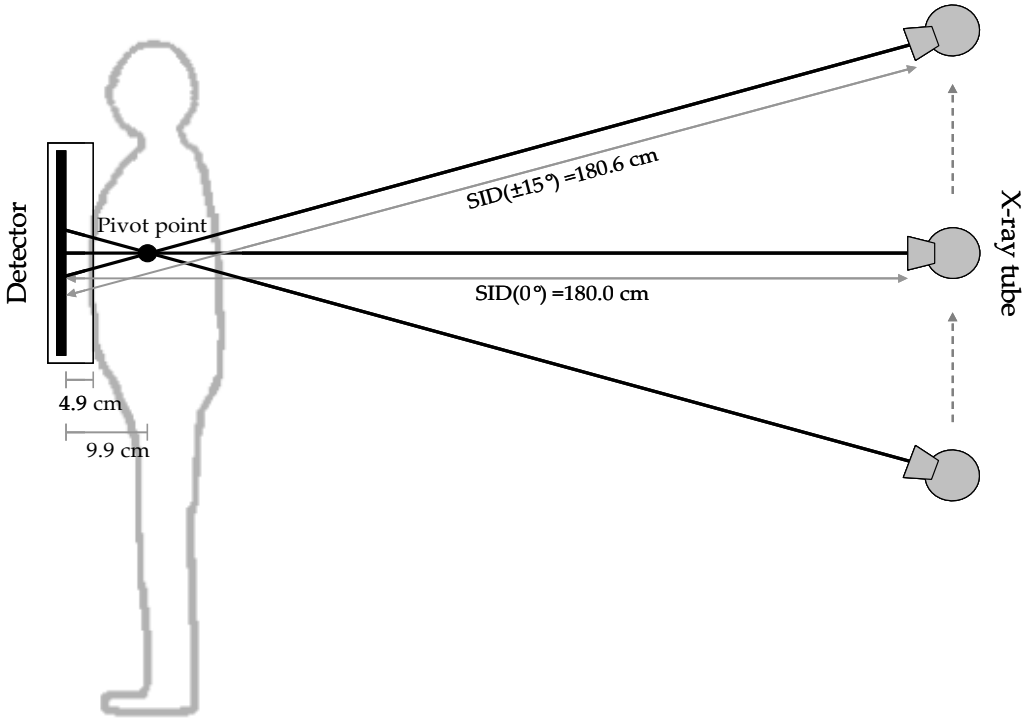

Figure 3.1. Illustration of the geometry used for the acquisition of tomosynthesis projection images using the GE Definium 8000 system with VolumeRAD option.

The tomosynthesis image acquisition is performed using a tube voltage of 120 kV and a total filtration of 3 mm Al + 0.1 mm Cu. The total exposure used for a tomosynthesis examination is determined by acquiring a scout image of the patient. The scout image is a PA projection image acquired at a tube voltage of 120 kV using AEC. The total exposure used for the acquisition of the tomosynthesis projection images is obtained by multiplying the tube load (mAs) used for the acquisition of the scout image by a factor (commonly 10). The total mAs obtained is then evenly distributed between the 60 projection images included in the tomosynthesis examination. The obtained mAs per projection image is rounded down to the closest Renard step (International standard ISO 3), with the constraint of a minimum tube load of 0.25 mAs per projection [32]. The projection images are used to reconstruct an arbitrary number of tomosynthesis section images using filtered backprojection. An example of a PA projection image and a reconstructed tomosynthesis section image of a patient is presented in Figure 3.2.

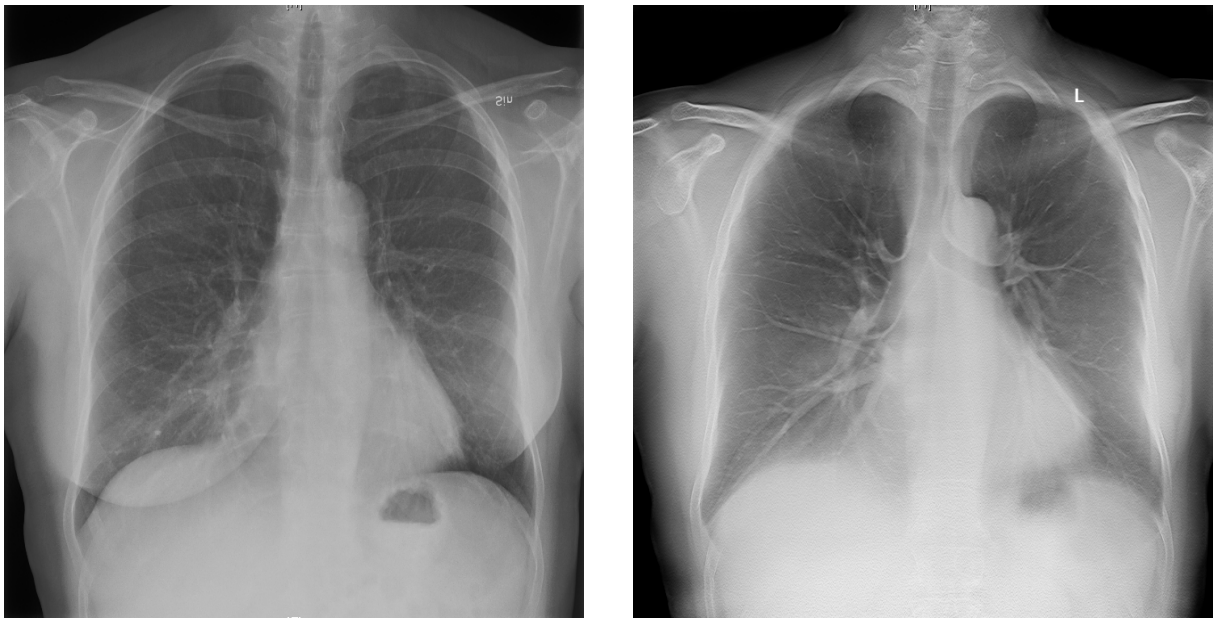

Figure 3.2. An example of a PA projection image (left) and a reconstructed tomosynthesis section image (right) required using the GE Definium 8000 system with VolumeRAD option.

It has been shown that the resulting effective dose to a patient from a chest radiography examination using the GE tomosynthesis system is approximately 0.05 mSv, while the tomosynthesis examination results in an effective dose to the patient of approximately 0.13 mSv [32, 33].

"I'm not lost for I know where I am. But however, where I am may be lost."

-A.A. Milne

4 Dosimetry

Radiation dose measurements are performed in radiology for two main purposes: to estimate the exposure of the patient, and to measure the performance of X-ray equipment [14]. The method used for dose measurements must be chosen based on both the purpose of the measurements and the X-ray modality. Two types of dose quantities are defined for use in radiological protection: operational quantities and protection quantities. The operational quantities are defined by the International Commission on Radiation Units and Measurements (ICRU) [61] and are based on the determination of the amount of energy that is released by uncharged particles (including photons) in a matter of interest. The protection quantities are defined by the International Commission on Radiological Protection (ICRP) [15] and are based on the mean absorbed dose in an organ or tissue, weighted by risk factors associated with the type of radiation and the radiation sensitivity of that organ or tissue. In 2007 the International Atomic Energy Agency (IAEA) established an international code of practice for dosimetry in diagnostic radiology [62]. This code of practice is based on the dose quantities previously prescribed by the ICRU and ICRP.

As knowledge about commonly used dosimetric quantities in diagnostic radiology is needed in order to investigate the dosimetry of chest tomosynthesis, a review of the commonly used operational and risk-related dose quantities is given in the following Sections 4.1-4.2. The risk-related dose quantity effective dose was in the present work determined using the Monte Carlo based software PCXMC (PC program for X-ray Monte Carlo). A description of this software is given in Section 4.3.

4.1 Operational dose quantities

4.1.1 Kerma

The dosimetric quantity kerma (kinetic energy released per unit mass) refers to the sum of the initial kinetic energy (dE_{tr}) of all the charged particles that are created by uncharged particles (photons or neutrons) in a mass (dm) of a material [62]. The kerma (K) can thus be defined as:

$$K = \frac{dE_{tr}}{dm} \tag{4.1}$$

and has the unit J/kg, or gray (Gy). The quantity E_{tr} does not include the relatively small amount of energy that is needed to overcome the binding energies of the charged particles released [63].

4.1.2 Energy imparted

The energy imparted (ε) is the sum of all the energy deposited in a volume:

$$\varepsilon = \sum_i \varepsilon_i . \tag{4.2}$$

The mean energy imparted to a volume of matter is defined as the radiant energy entering the volume (R_{in}) minus the radiant energy leaving the volume (R_{out}), plus the sum of all changes in rest energies ($\sum Q$) of the nuclei and elementary particles that occur in the volume [62]. The mean energy imparted can thus be defined as:

$$\bar{\varepsilon} = R_{in} - R_{out} + \sum Q \tag{4.3}$$

and has the unit J. It should be noted that the term $\sum Q$ is equal to zero for the photon energies used in diagnostic radiology.

4.1.3 Absorbed dose

The mean energy imparted ($d\bar{\varepsilon}$) is used to calculate the absorbed dose (D), which is often used to quantify the energy deposition in matter of mass (dm) [62], thus

$$D = \frac{d\bar{\varepsilon}}{dm} \tag{4.4}$$

with the unit J/kg, or gray (Gy).

4.1.4 Incident air kerma

The incident air kerma (K_i) is the kerma measured in air, at the point where the central axis of the X-ray beam enters the patient or phantom [62]. The incident air kerma only includes primary radiation, and hence, the backscattered radiation is excluded. The incident air kerma can either be measured at the exact point of interest, or be approximated using knowledge of the focal-spot-to-surface (skin) distance (FSD) and the air kerma (K_a) at any other distance (d) from the focal spot, by using the inverse square law [63]. Thus, the incident air kerma can be expressed as:

$$K_i = K_a(d)\left(\frac{d}{d_{FSD}}\right)^2 \tag{4.5}$$

with the unit J/kg, or gray (Gy).

4.1.5 Entrance surface air kerma

The entrance surface air kerma (K_e) is determined at the point where the central axis of the X-ray beam enters the patient. The difference between the incident air kerma and the entrance surface air kerma is that the latter includes contributions from backscattered radiation [62]. Hence, the entrance surface air kerma is related to the incident air kerma through:

$$K_e = K_i B \tag{4.6}$$

where B is the backscatter factor, which depends on the X-ray spectrum, the field size and the specific features of the patient or phantom (i.e. thickness and composition) [63]. The entrance-surface air kerma also has the unit J/kg, or gray (Gy).

4.1.6 Air kerma-area product

The air kerma-area product (KAP or P_{KA}) is the air kerma (K_a) integrated over an area (A) in a plane perpendicular to the central axis of the X-ray beam [62]. Hence, P_{KA} can be written:

$$P_{KA} = \int_A K_a(A)dA \tag{4.7}$$

and has the unit (J/kg)cm^2, or Gycm^2. If air attenuation and scattering can be neglected, P_{KA} is invariant with distance from the focal spot, as long as the distance to the patient (or phantom) is large enough for backscattered radiation from the patient/phantom not to be included in the measurement.

4.2 Risk-related dose quantities

Before the introduction of the risk-related dose quantities the exposure of the patient was commonly expressed as the entrance surface dose measured on the patient's skin at the point where the central axis of the X-ray beam enters the patient. Alternatively, the incident air kerma at the point where the central axis of the X-ray beam enters the patient was estimated by measuring the incident air kerma in an arbitrary point along the x-ray beam axis and then converting this measure using the inverse-square law [63]. These measurements may be sufficient for the purpose of quality control of the equipment (e.g. exposure stability), but are, however, not optimal for estimation of risk factors connected to the exposure, as a change in radiation quality, patient size or the part of the body being irradiated will have considerable impact on the assessed risk. Risk-related dose quantities were first presented by ICRP in 1977 (Publication 26) [64], while the modern terminology equivalent dose and effective dose were introduced in the 1990 recommendations of the ICRP (Publication 60) [65].

Both quantities are based on information about the mean absorbed dose in an organ or tissue, but also account for the relative biological effectiveness (RBE) of ionizing radiation, and the sensitivity of different organs/tissues to radiation.

4.2.1 Equivalent dose

Different types of radiation (e.g. photons, electrons and heavy ions) result in various degrees of cell damage, i.e. different types of radiation have different RBE values. Consequently, *radiation weighting factors* were introduced [64]. Applying the radiation weighting factors to the mean absorbed dose in an organ or tissue, results in a weighted absorbed dose, also called the equivalent dose. The equivalent dose (H_T) is defined as [62]:

$$H_T = \sum_R w_R D_T \tag{4.8}$$

where w_R is the radiation weighting factor for the type of radiation R and D_T is the mean absorbed dose in the organ or tissue (T). Equivalent dose has the unit J/kg, or sievert (Sv).

4.2.2 Effective dose

As the sensitivity of different organs and tissues to radiation differs, *tissue weighting factors* were introduced [64]. By applying tissue weighting factors to the equivalent dose in each organ or tissue and then make a summation of the equivalent doses in all organs and tissues, a quantity called the effective dose is obtained. The effective dose (E) is defined as [62]:

$$E = \sum_T w_T H_T, \tag{4.9}$$

where w_T is the tissue weighting factor for tissue/organ T. Effective dose also has the unit J/kg, or sievert (Sv).

The ICRP has estimated the lifetime risk of radiation-induced side effects (both deterministic effects and stochastic effects) by observations made on individuals who have been exposed to high doses of radiation. These risk estimates have been derived by averaging over sex and age at exposure [15]. Deterministic effects (inevitable effects) are assumed to occur when the dose exceeds a threshold value. Consequently, the risk estimates for deterministic effects are based on observations

of individuals who have been exposed to high doses of radiation, either by accident or in medical situations (e.g. radiotherapy). The risk of stochastic effects (randomly occurring effects, such as cancer and hereditary disorders) is based on the linear non-threshold (LNT) dose-response relationship. This means that it is assumed that the probability of stochastic effects increases linearly with dose. The validity of the LNT model has, however, been the subject of heated debate over the past decades. Many of the arguments for and against this model are discussed in a review by Johansson [66].

In general, the parameters used to estimate the risk of stochastic effects by the ICRP are based on the follow-up of individuals participating in the Japanese Life Span Study on atomic bomb survivors [67]. Since the first publication of the risk-related dose quantities by ICRP in 1977 [64], further follow-ups have been performed. This has resulted in revisions of the tissue weighting factors. The revisions are presented in ICRP Publication 60 [65] from 1990 and in ICRP Publication 103 [15] from 2007. The existing conversion factors (see Section 4.4) used to estimate the resulting effective dose from commonly performed radiological procedures are based on the tissue weighting factors presented in ICRP 60. The determination of conversion factors to use for the estimation of resulting effective dose from a chest tomosynthesis examination, presented in Paper I, were however based on the tissue weighting factors presented in ICRP Publication 103. The differences in tissue weighting factors between these two publications will therefore here be discussed in more detail.

Table 4.1. The tissue weighing factors in the ICRP Publications 60 (from 1990) and 103 (from 2007). Note: *r* indicates remainder organ/tissue, "–" indicates organs/tissues not included in the calculation of effective dose.

Organ	Publication 60	Publication 103
Red bone marrow	0.12	0.12
Breasts	0.05	0.12
Colon	0.12	0.12
Lungs	0.12	0.12
Stomach	0.12	0.12
Ovaries	0.20	0.08
Testicles	0.20	0.08
Liver	0.05	0.04
Oesophagus	0.05	0.04
Thyroid	0.05	0.04
Urinary bladder	0.05	0.04
Bone surface	0.01	0.01
Skin	0.01	0.01
Salivary glands	–	0.01
Brain	*r*	0.01
Adrenals	*r*	*r*
Extrathoracic region	–	*r*
Gall bladder	–	*r*
Heart	–	*r*
Kidneys	*r*	*r*
Lymphatic nodes	–	*r*
Muscle	*r*	*r*
Oral mucosa	–	*r*
Pancreas	*r*	*r*
Prostate	–	*r*
Small intestine	*r*	*r*
Upper large intestine	*r*	–
Spleen	*r*	*r*
Thymus	*r*	*r*
Uterus	*r*	*r*

The changes in tissue weighting factors between ICRP Publication 60 and ICRP Publication 103 are shown in Table 4.1. Apart from the fact that a larger number of organs/tissues have obtained specific weighting factors in the latest publication, the most significant changes in tissue weighting factors are found for the breasts and gonads (ovaries and testicles). The weighting factor for the breasts has been increased from 0.05 (Publication 60) to 0.12 (Publication 103). One of the reasons for this increase is due to the fact that the risk estimates in ICRP Publication 60 were

based on mortality data, while the risk estimations in the most recent report are based on incidence data. By also including curable cancer cases in the risk estimate, a more complete description of the radiation-induced risks is obtained and the risk estimates are not affected by improvements in the treatment of the disease. Furthermore, in ICRP Publication 60 all genetic diseases occurring due to radiation exposure were regarded as lethal, while ICRP Publication 103 accounts for both the severity and lethality of different genetic diseases. Consequently, the weighting factor for the gonads has been reduced from 0.20 to 0.08 in ICRP Publication 103. An additional difference between the tissue weighting factors given in ICRP Publication 60 and ICRP Publication 103 is the treatment of the remainder organs. In ICRP Publication 60 the remainder organs (indicated by *r* in Table 4.1) were together assigned a weighting factor of 0.05. However, if one of the organs included in the remainder organs was exposed to a higher equivalent dose than any of the other organs listed in Table 4.1, the weighting factor of that specific remainder organ was set to 0.025, while the rest of the remainder organs were assigned a weighting factor of 0.025. In ICRP publication 103 a weighting factor of 0.12 is evenly distributed between the remainder organs so that each of these organs has a weighting factor of 0.12/13 (for a specified patient (male or female) the prostate or the uterus is included in the calculations of effective dose, why the weighting factor of 0.12 is divided by 13 even though 14 remainder organs are listed in Table 4.1). Note: the upper large intestine, which was included as one of the remainder organs in ICRP Publication 60, has in ICRP Publication 103 been combined with the lower large intestine to define the colon.

4.2.3 Determination of the risk-related dose quantities

Calculations of absorbed dose distributions in the human body require information about the anatomical characteristics of the body. Using human reference values allows the effective doses from different radiation exposures to be compared. In 2002 the ICRP established reference values of heights, weights and organ masses for humans of six different ages: newborn, 1 year, 5 years, 10 years, 15 years and adult [68]. The reference values established for the 15-year-old and adult are gender specific. In 2007 the ICRP also presented a method of using reference computational voxel phantoms in dose calculations [15]. These voxel phantoms are designed according to the reference values established for the male and female adult [69], hence the male phantom (Rex) represents a human of height 176 cm and weight 73 kg, while the female phantom (Regina) represents a human of height 163 cm and weight 60 kg.

4.3 The PCXMC software

In 1997, STUK (the Radiation and Nuclear Safety Authority of Finland) released the software PCXMC [70]. The program is designed for calculating both organ doses and effective doses to patients undergoing various projection radiography examinations, including fluoroscopy. Since the release of the first version, the software has been improved and in the latest version, PCXMC 2.0 (released in 2008) [71], the mathematical phantom has been modified to take into account the new ICRP tissue weighting factors in Publication 103 [15].

4.3.1 Mathematical phantoms

The phantoms used in PCXMC are based on the mathematical phantom first described by Cristy and Eckerman in 1987 [72]. The phantom was originally intended to be used for dosimetric calculations in the case of internal, photon-emitting radiation sources. However, over the years the phantom has been modified to produce mathematical models that are suitable for dosimetry calculations for external photon irradiation [73]. Further modifications were made by Tapiovaara et al. when implementing the phantom in PCXMC 2.0 [71]:

- the head has been modelled to a more realistic shape (not a cylinder),
- salivary glands have been added,
- the lateral width of the facial skeleton has been reduced to make room for the parotid glands,
- the vertical location of the facial skeleton has been modified (moved down),
- the position of the thyroid has been modified,
- extrathoracic airways have been added,
- mouth mucosa has been added,
- the prostate gland has been added,
- the arms of the phantom can be removed (in order to resemble simulations of lateral projections), and
- the size of the patient can be adjusted (height and weight).

Six preset phantom sizes are available in PCXMC, representing patients of various ages: newborn (50.9 cm, 3.4 kg), 1 year old (74.4 cm, 9.2 kg), 5 years old (109.1 cm, 19.0 kg), 10 years old (139.8 cm, 32.4 kg), 15 years old (168.1 cm, 56.3 kg) and adult (178.6 cm, 73.2 kg) [71]. The size of the phantom, including organ sizes, can be manually varied by modifying a preset phantom size using scaling factors. The scaling factors for variations in phantom height (h) and weight (w) are given by:

$$s_z = \frac{h}{h_0} \tag{4.10}$$

and

$$s_{xy} = \sqrt{\frac{h_0 \cdot w}{h \cdot w_0}} \tag{4.11}$$

where s_z is the scaling factor in the direction of the z-axis (phantom height), s_{xy} is the scaling factor in the direction of the x- and y-axes (phantom width and thickness, respectively), and h_0 and w_0 are the height and weight of the unscaled phantom [71]. It should be noted, however, that although the possibility of changing the phantom size enables simulations of patients of various sizes, the variability in patient size due to variation in fat tissue can not be simulated.

4.3.2 Monte Carlo simulations

The Monte Carlo simulations in PCXMC are based on user-supplied input parameters describing the geometry of the examination to be simulated. Hence, parameters values such as patient size, the size and orientation of the radiation field, incident angle of the X-ray beam, FSD and the number of photon histories to be simulated are determined.

The Monte Carlo simulations in PCXMC include calculations of the photon transport through matter, based on probability distributions of different scattering processes. Monochromatic photons of different energies (10, 20, 30, …, 150 keV) are simulated in ten different batches of each energy level. According to Tapiovaara et al. [71], this energy resolution is sufficient, as the energy absorbed in an organ per photon is a smooth function of photon energy. The absorption at each energy value and the statistical error are obtained from the average value and standard deviation of the ten batches. The photons are assumed to be emitted from an isotropic point source, into the angular region limited by the focal distance and dimensions of the X-ray field. If a maximum photon energy of 150 keV is chosen by the user, all energy levels below that energy level are included in the simulation. The energy deposition in each organ is calculated at each photon interaction point when passing through the phantom [71].

Due to the low maximum energy of 150 keV, only photoelectric absorption, coherent (Rayleigh) scattering and incoherent (Compton) scattering are of importance in the calculations. As the range of secondary electrons is very short at these photon energies, the energy of the secondary electrons can be assumed to be absorbed at the same location as the photon interaction [71]. The only exception from this assumption is when calculating the dose to the bone marrow. This is due to the fact that the

active bone marrow is located in small cavities in the trabecular bone. Therefore, even secondary electrons with a very short range can influence the results when calculating dose to the active bone marrow. In the mathematical phantoms used in PCXMC, the bones are modelled as having a homogeneous composition of minerals and organic material. In reality the size of the bone marrow cavities varies, depending on patient size and the anatomical location of the bone. When calculating bone marrow dose in PXCMC, the total amount of energy deposited in the phantom skeleton is distributed between two skeletal components: active bone marrow and bone minerals [71]. The same distribution between the two skeletal components is used for all patient sizes and all parts of the skeleton.

4.3.3 Dose calculations

After defining the geometry of the examination and performing the Monte Carlo simulations of the photon histories for this geometry, the resulting doses can be calculated for any X-ray output and X-ray spectrum. The X-ray output can be expressed as the K_i at the point were the central axis of the X-ray beam enters the patient (given in mGy), the exposure (given in mR), the KAP (given in $mGycm^2$) or the exposure-area product (given in Rcm^2) [71]. The X-ray spectrum is defined by the X-ray tube voltage, the tube anode angle and the total filtration. PCXMC then calculates the mean values of absorbed doses, averaged over the organ volume for the organs listed in Table 4.1. PCXMC can also be used to calculate the effective dose resulting from an examination using the absorbed doses and the tissue weighting factors given in ICRP Publication 60 and ICRP Publication 103. It should, however, be noted that PCXMC does not calculate the effective dose exactly as stated in ICRP Publication 103. As mentioned above, PCXMC uses mathematical, size-adjustable hermaphrodite phantoms for the dose calculations, instead of using the reference male (Rex) and female (Regina) voxel phantoms that are prescribed by the ICRP.

4.4 Conversion factors

As the determination of effective dose requires knowledge of the radiation dose to a large number of different organs in the body, it is time-consuming, and it is thus unlikely to be performed routinely in radiology departments. In 1994 the UK National Radiological Protection Board (NRPB) introduced the concept of using conversion factors to estimate the effective dose from conventional radiographic examinations [48]. The idea behind the use of conversion factors was that the resulting effective dose from common radiological examinations could be easily estimated by multiplying a known dose measure from an examination with a specified conversion factor for that examination. The dose measures considered in this NRPB report were the surface entrance dose and the KAP, and Monte Carlo simulations were performed to estimate the effective doses for different projection images. A mathematical hermaphrodite phantom [74] representing an average adult

patient was used in the simulations, and 40 different radiation qualities were considered. Tube voltages ranging from 50 to 120 kV in steps of 10 kV were simulated, and the total filtration was varied between 2 and 5 mm Al (2, 2.5, 3, 4 and 5 mm Al). The effective doses were calculated using the tissue weighting factors presented in ICRP Publication 60 [65]. For complete examinations (including more than one projection image) the KAP value summed over all projection images was determined to provide a better measure of patient dose than the entrance surface dose, thus only conversion factors between KAP and effective dose (E_{KAP}) were calculated for complete examinations [48]. For a lung examination, including a PA projection image and a LAT projection image, E_{KAP} was determined to be 0.1 mSv/Gycm^2 for an examination performed using radiation qualities of 70 kV (PA projection) and 85 kV (LAT projection) and total filtration of 3 mm Al. However, as chest examinations are normally performed with tube voltages of 120 kV or higher in the Nordic countries, the E_{KAP} given in the NRPB report has been adjusted to 0.18 mSv/Gycm^2 by the radiation protection and nuclear safety authorities in Denmark, Finland, Iceland, Norway and Sweden [75].

4.5 Previous work on the dosimetry of chest tomosynthesis

To date, two papers focusing on the dosimetry of the GE chest tomosynthesis system have been published. These dosimetric evaluations are both based on Monte Carlo simulations of the GE tomosynthesis system using the PXCMC software described above.

Sabol [32] based dose calculations on exposure data obtained from patients who had undergone chest radiographic examinations at different hospitals in the Unites States. Only patients estimated to be of average size by the radiological technicians who performed the examinations, were included in the study. The average tube load obtained for the PA projection was 1.9 mAs (based on 286 patients), which corresponds to an incident air kerma of 0.10 Gy. The corresponding values for the LAT projection were 5.9 mAs and 0.40 Gy (based on 104 patients). As no detailed information about the patient sizes were known, a patient with a height of 176 cm and a weight of 86.3 kg was used in the simulations (average size of an American male). The geometric parameters used in the simulation of the tomosynthesis examination were obtained by performing a tomosynthesis scan of a medium-sized anthropomorphic chest phantom. Assuming the same exposure data for the tomosynthesis scout image as for the PA projection image, the resulting effective doses, calculated using the tissue weighting factors presented in ICRP Publication 103, arising from the examinations were 0.0165 mSv (PA), 0.0386 mSv (LAT) and 0.124 mSv (tomosynthesis without scout image).

Båth et al. [33] instead based their dose calculations on tomosynthesis examinations of patients with known sizes. The mean values of both patient size and exposure parameters for 40 patients who had undergone both chest radiography and chest tomosynthesis examinations were used as input parameters to PCXMC. The mean height and weight of these patients were 170.9 cm and 70.2 kg, respectively, resulting in effective doses (tissue weighting factors in ICRP Publication 103) of 0.014 mSv (PA projection), 0.039 mSv (LAT projection) and 0.122 mSv (tomosynthesis without scout image).

4.6 Summary of Paper I

4.6.1 Background

Although not yet fully evaluated, many studies have shown that chest tomosynthesis has the potential to improve the diagnostic outcome from a chest examination compared to conventional chest radiography [23-28]. Furthermore, it has been suggested that chest tomosynthesis may provide an alternative to thoracic CT examinations in specific situations, without a substantial loss in diagnostic information [31]. Therefore, it can be expected that the number of chest tomosynthesis examinations performed at hospitals around the world will increase, emphasizing the need for a thorough dosimetric evaluation of the examination. It can also be expected that other image acquisition parameters will be used in future tomosynthesis systems, including both geometric parameters and exposure parameters. The aims of the study presented in Paper I were to investigate the dosimetry of chest tomosynthesis systems and to determine E_{KAP} for various system configurations and patient sizes.

4.6.2 Description of the method

The Monte Carlo-based software PCXMC 2.0 was used to simulate different tomosynthesis system configurations and patient sizes and calculating the resulting effective doses. In the simulations the angular interval for image acquisition was varied from ±5° to ±30°, in steps of ±5°, using an angular resolution of 1°. The projection images were assumed to be uniformly distributed over each angular interval, which in turn was assumed to be symmetrical around the zero-degree projection (the corresponding PA projection). The central axis of the X-ray beam was, for all projection images, directed towards the centre of the detector. In the zero-degree projection, the field size was adjusted to cover the lungs (as in a conventional PA projection), and for each angular projection image the field was collimated to obtain the same field size at the detector surface. The Monte Carlo simulations were performed using different patient sizes and tube voltages and for all simulations a total filtration of 3 mm Al and 0.1 mm Cu was assumed. Different distributions of the exposure between the projection images were investigated (constant K_i, constant

KAP, constant tube load and constant effective dose for each projection image). Values of E_{KAP} were obtained for the zero-degree projection alone (corresponding to the PA projection in conventional chest radiography) and for the entire tomosynthesis examination for each tomosynthesis system configuration and patient size.

4.6.3 Results

The collimation of the x-ray beam for three different incident angles of the X-ray beam (-30°, 0° and +30°) using a phantom of height 170 cm and weight 70 kg are shown in Figure 4.1. The ratio between effective dose and KAP for different tomosynthesis projection angles, using this phantom size and calculated using a tube voltage of 120 kV, is presented in Figure 4.2. It is evident that the ratio is highly dependent on the tomosynthesis projection angle, and that the ratio is in general higher when the radiation enters the patient from below (positive angles in Figure 4.2).

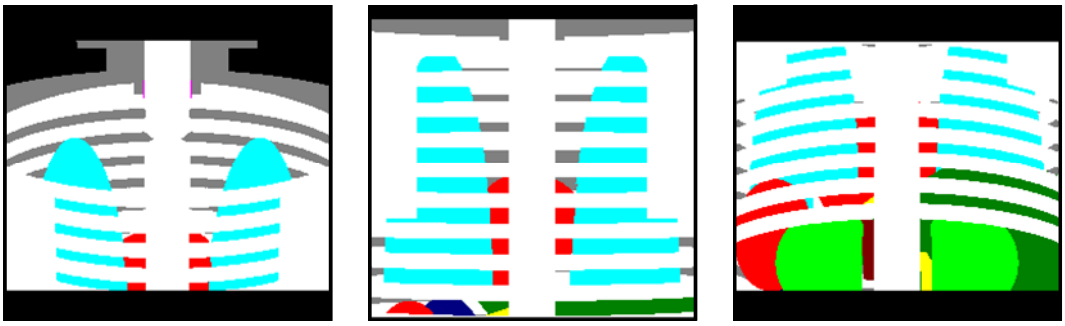

Figure 4.1. Screen shots from the PCXMC software, showing the collimation of the x-ray field in the calculation of effective dose, for three different incident angles of the X-ray beam (-30° left, 0° middle and +30° right).

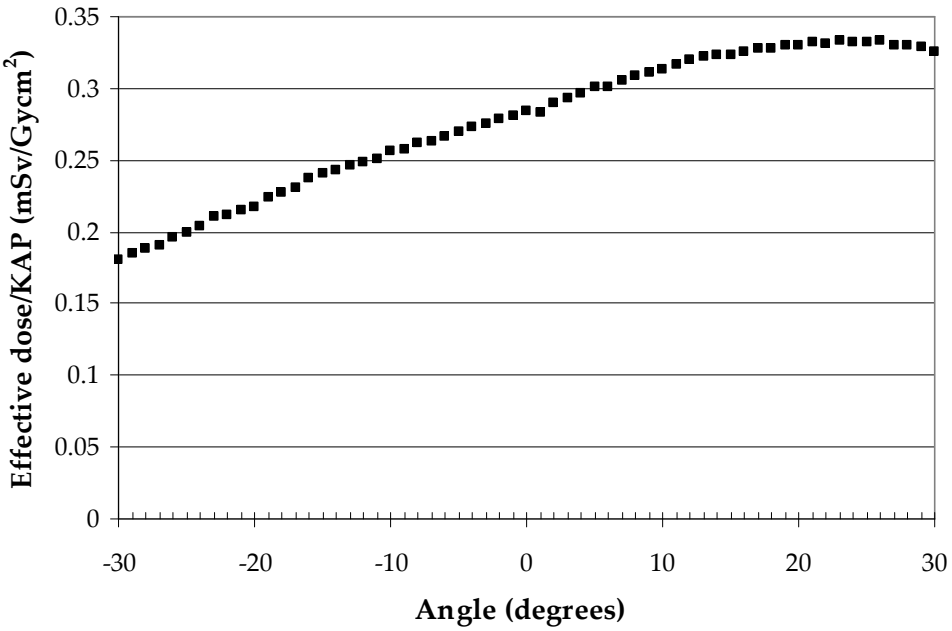

Figure 4.2. The ratio between effective dose and KAP for projection angles between -30° and +30°, calculated using a tube voltage of 120 kV and a patient of height 170 cm and weight 70 kg. Positive angles correspond to radiation entering the patient from below. (Adapted from Paper I.)

The E_{KAP} for the zero-degree projection is presented for different patient sizes, calculated using a tube voltage of 120 kV, in Table 4.2, while Table 4.3 gives the variation in E_{KAP} with tube voltage, calculated using a patient of 170 cm and 70 kg. It was found that the E_{KAP} depended substantially on patient size (decreasing for larger patients) and tube voltage (increasing for higher tube voltages). However, the dependency on the angular interval was much smaller, as can be seen from Tables 4.4 and 4.5.

The effective dose from a tomosynthesis examination can thus be estimated by multiplying the total KAP of the examination with the appropriate E_{KAP} for the tomosynthesis examination, $E_{KAP,tomo}$. The $E_{KAP,tomo}$ is obtained by combining the E_{KAP} values for the zero degree projection image, presented in Tables 4.2 and 4.3, with the percentage difference (PD) in E_{KAP} between the tomosynthesis examination and the zero degree projection image, presented in Tables 4.4 and 4.5, according to:

$$E_{KAP,tomo} = E_{KAP} \cdot (1 + PD) \tag{4.12}$$

Table 4.2. E_{KAP} for the zero-degree projection for different patient sizes, calculated using a tube voltage of 120 kV. The estimated statistical error in E_{KAP} from the Monte Carlo simulation was 0.1 % (standard deviation). (Adapted from Paper I.)

Patient size	E_{KAP} (mSv/Gycm^2)
170 cm, 50 kg (BMI = 17.3, PA thickness = 17.0)	0.372
170 cm, 60 kg (BMI = 20.8, PA thickness = 18.5)	0.326
170 cm, 70 kg (BMI = 24.2, PA thickness = 20.0)	0.285
170 cm, 80 kg (BMI = 27.7, PA thickness = 21.4)	0.255
170 cm, 90 kg (BMI = 31.1, PA thickness = 22.7)	0.231
170 cm, 100 kg (BMI = 34.6, PA thickness = 24.0)	0.207

Table 4.3. E_{KAP} for the zero-degree projection for a patient sized 170 cm and 70 kg, calculated using different tube voltages. The estimated statistical error in E_{KAP} from the Monte Carlo simulation was 0.1 % (standard deviation). (Adapted from Paper I.)

Tube voltage	E_{KAP} (mSv/Gycm^2)
100 kV	0.257
110 kV	0.277
120 kV	0.285
130 kV	0.295
140 kV	0.304
150 kV	0.311

Upon comparing the E_{KAP} for the zero-degree projections with those obtained for the entire tomosynthesis examinations it was found that the difference was smaller than 10 %, irrespective of system configuration and patient size (see Tables 4.4 and 4.5). It was therefore concluded that the total effective dose resulting from a tomosynthesis examination could be estimated with acceptable accuracy only by using the E_{KAP} for the zero-degree projection.

Table 4.4. The PD between the E_{KAP} for an entire tomosynthesis examination, and that for the zero-degree projection, calculated for different system configurations and patient sizes. The estimated error in percentage difference was 0.1%. (Adapted from Paper I.)

Patient size	Constant air kerma						Constant KAP						Constant tube load						Constant effective dose					
Angular interval	±30	±25	±20	±15	±10	±5	±30	±25	±20	±15	±10	±5	±30	±25	±20	±15	±10	±5	±30	±25	±20	±15	±10	±5
170 cm, 50 kg (BMI = 17.3)	-0.9	-0.2	0.2	0.4	0.4	0.2	-1.0	-0.2	0.2	0.4	0.4	0.2	-0.7	-0.1	0.3	0.4	0.4	0.2	-3.6	-2.0	-0.9	-0.2	0.1	0.1
170 cm, 60 kg (BMI = 20.8)	-1.6	-0.7	0.0	0.3	0.4	0.3	-1.7	-0.7	0.0	0.3	0.4	0.3	-1.4	-0.6	0.0	0.3	0.4	0.3	-4.7	-2.8	-1.4	-0.5	0.1	0.2
170 cm, 70 kg (BMI = 24.2)	-2.8	-1.6	-0.7	-0.2	-0.1	-0.1	-2.9	-1.6	-0.8	-0.2	-0.1	-0.1	-2.4	-1.4	-0.7	-0.2	-0.1	-0.1	-6.1	-3.9	-2.2	-1.1	-0.5	-0.3
170 cm, 80 kg (BMI = 27.7)	-3.3	-2.0	-1.0	-0.4	0.0	0.0	-3.5	-2.0	-1.0	-0.4	0.0	0.0	-3.0	-1.8	-1.0	-0.4	0.0	0.0	-7.0	-4.5	-2.6	-1.3	-0.4	-0.1
170 cm, 90 kg (BMI = 31.1)	-4.0	-2.5	-1.3	-0.5	0.0	0.2	-4.2	-2.6	-1.3	-0.5	0.0	0.2	-3.6	-2.3	-1.2	-0.5	0.0	0.2	-8.0	-5.3	-3.1	-1.6	-0.5	0.0
170 cm, 100 kg (BMI = 34.6)	-4.6	-3.0	-1.7	-0.7	-0.1	0.2	-4.8	-3.1	-1.7	-0.7	-0.1	0.2	-4.2	-2.8	-1.6	-0.7	-0.1	0.2	-8.9	-6.0	-3.7	-1.9	-0.7	0.0

Table 4.5. The PD between the E_{KAP} for an entire tomosynthesis examination, and that for the zero-degree projection, calculated using a patient sized 170 cm and 70 kg, for different system configurations and tube voltages. The estimated error in percentage difference was 0.1%. (Adapted from Paper I.)

Tube voltage	Constant air kerma						Constant KAP						Constant tube load						Constant effective dose					
Angular interval	±30	±25	±20	±15	±10	±5	±30	±25	±20	±15	±10	±5	±30	±25	±20	±15	±10	±5	±30	±25	±20	±15	±10	±5
100 kV	-3.1	-1.9	-1.0	-0.4	-0.2	-0.2	-3.3	-2.0	-1.0	-0.4	-0.2	-0.2	-2.8	-1.8	-1.0	-0.4	-0.2	-0.2	-6.7	-4.3	-2.6	-1.3	-0.6	-0.4
110 kV	-2.3	-1.7	-0.8	-0.2	0.1	0.1	-2.4	-1.8	-0.8	-0.2	0.1	0.1	-2.0	-1.4	-0.6	-0.1	0.2	0.1	-5.3	-3.6	-1.9	-0.9	-0.2	0.0
120 kV	-2.8	-1.6	-0.7	-0.2	-0.1	-0.1	-2.9	-1.6	-0.8	-0.2	-0.1	-0.1	-2.4	-1.4	-0.7	-0.2	-0.1	-0.1	-6.1	-3.9	-2.2	-1.1	-0.5	-0.3
130 kV	-2.5	-1.4	-0.6	-0.1	0.0	-0.1	-2.7	-1.5	-0.7	-0.1	0.0	-0.1	-2.3	-1.3	-0.6	-0.1	0.0	-0.1	-5.9	-3.7	-2.1	-1.0	-0.4	-0.2
140 kV	-2.4	-1.3	-0.6	-0.1	0.0	-0.1	-2.5	-1.4	-0.6	-0.1	0.0	-0.1	-2.1	-1.2	-0.5	-0.1	0.0	-0.1	-5.7	-3.6	-2.0	-0.9	-0.4	-0.2
150 kV	-2.3	-1.2	-0.5	0.0	0.0	0.0	-2.4	-1.3	-0.5	0.0	0.0	0.0	-2.0	-1.1	-0.5	0.0	0.0	0.0	-5.5	-3.4	-1.5	-0.9	-0.4	-0.2

"I do remember, and then when I try to remember,
I forget."

-A.A. Milne

5 Simulated dose reduction

The ALARA principle states that all X-ray examinations should be optimized so that images with sufficient clinical quality are obtained using the lowest possible radiation exposure of the patients [15]. One way to determine the optimum patient exposure for an examination is to perform observer performance studies using clinical images acquired using various amounts of radiation exposure. This procedure will, however, require unnecessary additional exposure of patients. Instead of using clinical images it may therefore be beneficial to simulate that an examination has been performed using a lower exposure. Methods of simulating dose reduction have been described previously for conventional radiography [50-52], tomosynthesis [76] and CT [53-57]. The methods described for simulated dose reduction in conventional radiography and tomosynthesis are summarized in section 5.3. As can be seen in these summaries the described methods use different approaches to create simulated low-dose images. In the simplest approach, noise is measured as standard deviation and white noise is added to the original image to obtain a specific standard deviation in the low-dose images. In most radiography systems, however, the pixel values are correlated, and if this is not taken into account in the dose reduction process the noise properties of the simulated low-dose image will differ from those in images actually acquired at the lower dose. The noise in the CT projection data has no correlation (correlations between the pixels are only obtained in the reconstruction process), why methods that are based on the process of adding Gaussian distributed quantum noise to the projection data of CT examinations [53, 54] will produce simulated images with noise properties comparable to those of images actually acquired at a lower dose [77]. If simulated dose reduction in the case of CT is made by adding noise to the reconstructed CT images, the correlation between the pixels must be taken into account in order to obtain valid results [55-57].

Simulating dose reduction in tomosynthesis can be based on the same methods as used for conventional radiography. However, as each projection image included in the tomosynthesis examination is acquired using a very low exposure levels the situation is more complex. Due to the low levels of radiation entering the detector, the assumption of a constant DQE over all dose levels may no longer be valid [78, 79]. Hence, potential variations in DQE must be taken into account when simulating lower doses. Furthermore, as the projection images are acquired from various oblique angles, it can not be assumed that the noise properties are constant for different projection images or radially symmetric. It is, therefore, of great importance that the characteristics of the medical system being simulated are well known in order to obtain valid results in the simulation process. As described in Section 1.3, one way to characterize an imaging system and compare it to other imaging systems

without accounting for a specific imaging task is to describe the signal transfer through the system using LST. An introduction to LST is therefore given below.

5.1 Introduction to linear systems theory

When using LST to determine the signal and noise properties of a system, the system must fulfil some requirements in order to obtain valid results. First of all, the system must be linear, which means that the output signal from the system is proportional to the input signal. In general, no system is completely linear, and the use of LSA is thus always an approximation. However, most systems that have a pronounced non-linear response to a signal can be linearized by calibration. Second, the description is simplified if the system is 'shift-invariant', meaning that the signal response must be identical at all image locations. A review of the use of LST to describe the signal transfer through a medical system is given by Cunningham [80].

The signal entering an X-ray imaging system consists of a distribution of X-ray quanta. Each quantum can be represented by an impulse function, also known as a Dirac delta function. The Dirac delta function, $\delta(x-x_0)$, has a value of ∞ at location x_0 and 0 at all other locations. Hence, the integral of the Dirac delta function between $-\infty$ and $+\infty$ is 1 [81]. The response of the system to a delta function can be described by an impulse response function (IRF) [80]. In medical imaging the IRF is also called the point spread function (PSF).

Assuming an input signal f(x,y), the output signal S{f(x,y)} from a linear and stationary system with an IRF described by $IRF(x_0,y_0)$ can be approximated by the superposition of an IRF for each delta function [80]:

$$S\{f(x,y)\} = \int_{-\infty}^{+\infty}\int_{-\infty}^{+\infty} f(x',y')IRF(x-x',y-y')dx'dy'. \tag{5.1}$$

The integral in Eq. 5.1 is called the convolution integral, and can also be written [80]:

$$S\{f(x,y)\} = f(x,y) \otimes IRF(x,y) \tag{5.2}$$

or

$$S\{f(x,y)\} = f(x,y) \otimes PSF(x,y). \tag{5.3}$$

The output signal from a linear, shift-invariant system can thus be simplified to the convolution of the input signal and the PSF of the system.

5.1.1 The Fourier transform

One way to extract the spatial frequencies of the output signal from an imaging system is to use Fourier transforms (FTs). These are commonly used in medical imaging to describe the properties of an imaging system. The two-dimensional FT of the signal f(x,y) is defined as [39]:

$$F(u,v) = \int_{-\infty}^{+\infty}\int_{-\infty}^{+\infty} f(x,y)e^{-2\pi\pi i(u+vy)}dxdy\,. \tag{5.4}$$

The inverse FT is thus:

$$f(x,y) = \int_{-\infty}^{+\infty}\int_{-\infty}^{+\infty} F(u,v)e^{+2\pi\pi i(u+vy)}dudv\,. \tag{5.5}$$

One of the benefits of using FTs is the convolution theorem, which states that convolution in the spatial domain is equal to multiplication in the spatial frequency domain [81]. Hence, using the FT, Eq. 5.4 can be written as [39]:

$$G(u,v) = F(u,v)\cdot T(u,v) \tag{5.6}$$

where G(u,v) is the FT of S{f(x,y)}, and T(u,v) is the FT of the PSF, also called the characteristic function of the system.

5.1.2 The sampling theorem and aliasing

When sampling a signal, information about the frequencies present in the signal is obtained. For all frequencies to be sampled correctly, the maximum sampling interval must be equal to or smaller than the reciprocal of twice the highest frequency present in the signal [81]. The sampling frequency corresponding to the maximum sampling interval for correct signal sampling is called the Nyquist frequency. If a signal is undersampled, i.e. if the sampling interval is too large, frequencies above the Nyquist frequency will appear as lower frequencies after sampling. This phenomenon is referred to as aliasing [39]. Undersampling is common in digital imaging devices and is almost always present to some degree [82].

5.2 Metrics of system performance

Quantitative evaluation of an imaging system often includes measurements that describe the signal transfer through the system. The modulation transfer function (MTF) describes the signal spread in the system, the noise power spectrum (NPS) describes the frequency components of the system noise, and the DQE describes the

efficiency of signal transfer through the system. More thorough descriptions of these measures are given below.

5.2.1 Modulation transfer function

For a given sinusoidal signal, S, the modulation of the signal, M, is defined as the ratio between the signal amplitude and the average signal [80]:

$$M = \frac{|S_{max}| - |S_{min}|}{|S_{max}| + |S_{min}|}. \tag{5.7}$$

Assuming a linear system the MTF is defined as the ratio between the modulation of the input and output signals and is usually expressed as a function of spatial frequency [80]:

$$MTF(u, v) = \frac{M(u, v)_{out}}{M(u, v)_{in}}. \tag{5.8}$$

For a linear system, the MTF is simply the amplitude of the two-dimensional FT (as a function of spatial frequency) of the PSF of the system [82]. Hence, MTF can be written as:

$$MTF(u, v) = \left|FT\{PSF(x, y)\}\right|. \tag{5.9}$$

As described above, aliasing may occur if the frequencies of a signal are not properly sampled by the system. In this case the system's response to a delta function can not be used to describe the modulation of signal frequencies when passing through the system [83]. Instead the presampling MTF, which describes the system's response to a signal without including the final sampling stage [82], can be used. In the routine used to simulate dose reduction described in Paper II, the MTF was assumed to be independent of detector dose. Hence, the presampling MTF need not be determined in order to use the method. A more thorough description of the presampling MTF is instead given in Section 6.3, as it was used for the lung nodule simulation.

5.2.2 Noise power spectrum

The theory described in Section 5.1 is based on the assumption that the system is linear and deterministic. A system is called deterministic if, when presented with two identical input signals, it produces two identical output signals [80]. However, random noise may occur in some systems, causing small fluctuations in the output signal [80]. Such a system is called a stochastic system. The NPS, also called the Wiener spectrum, describes the frequency distribution of the random fluctuations

(also called image noise). The NPS can be described as the variance in image intensity over the spatial frequencies in an image, or as the variance of a given spatial frequency in repeated measurements of that specific frequency [82]. In order to use the Fourier approach to describe the image noise, the imaging system should be shift-invariant and ergodic. A system is ergodic if the temporal averages are equal to the spatial averages [80]. The NPS of a shift-invariant, ergodic random process, with fluctuations given by $\Delta D(x,y)$, is defined as [39]:

$$NPS(u,v) = \lim_{X,Y\to\infty} \left\langle \frac{1}{2X}\frac{1}{2Y}\left| \int_{-X}^{+X}\int_{-Y}^{+Y} \Delta D(x,y) e^{-2\pi i(ux+vy)} dxdy \right|^2 \right\rangle \tag{5.10}$$

where $\langle\ \rangle$ denotes the ensemble average.

For a digital system, the NPS can be written [82]:

$$NPS(u,v) = N_x N_y \Delta_x \Delta_y \left\langle \left| FT\{\Delta D(x,y)\} \right|^2 \right\rangle \tag{5.11}$$

where N_x and N_y are the numbers of pixels in the x- and y-directions, respectively, and Δ_x and Δ_y are the corresponding pixel sizes.

When determining the NPS, an acquired flat-field image is commonly divided into several regions of interest (ROIs). The NPS in each ROI is determined using Eq. 5.11 and the final NPS is obtained by averaging the NPS in the ROIs. If the NPS is to be determined in an image containing non-uniformities, the normalized NPS (NNPS) can be used. The NNPS is given by [82]:

$$NNPS(u,v) = \frac{NPS(u,v)}{(\text{large area signal})^2} \tag{5.12}$$

where 'large area signal' is the mean pixel value in the ROI.

5.2.3 Detective quantum efficiency

For an ideal detector, the signal-to-noise ratio (SNR) would simply be proportional to the square root of the number of photons, N, in a specific ROI [82]:

$$SNR_{ideal} = \sqrt{N}\ . \tag{5.13}$$

In medical imaging, however, the detectors are seldom ideal as they contain other sources of noise in addition to the Poisson-distributed noise due to the variation in

the photon flux [82]. The SNR for a non-ideal detector is thus always smaller than for an ideal detector.

The DQE is a measure of the detector efficiency, and is defined as [39]:

$$\mathrm{DQE} = \frac{\mathrm{SNR}_{\mathrm{out}}^2}{\mathrm{SNR}_{\mathrm{in}}^2} \tag{5.14}$$

where $\mathrm{SNR}_{\mathrm{out}}$ is the SNR of the output signal and $\mathrm{SNR}_{\mathrm{in}}$ the SNR of the input signal. Hence, for an ideal detector, DQE is equal to 1. DQE can also be interpreted as:

$$\mathrm{DQE} = \frac{\mathrm{NEQ}}{\mathrm{N}} = \frac{\mathrm{NEQ}}{\mathrm{SNR}_{\mathrm{in}}^2} \tag{5.15}$$

where NEQ (noise-equivalent number of quanta) is the number of quanta required in an ideal detector to produce an output with the same SNR as a non-ideal (real) detector [82].

For a linear, shift-invariant and ergodic system, the frequency-dependent NEQ is given by [82]:

$$\mathrm{NEQ}(u,v) = \frac{\mathrm{MTF}^2(u,v)}{\mathrm{NNPS}(u,v)} = \frac{(\text{large area signal})^2\,\mathrm{MTF}^2(u,v)}{\mathrm{NPS}(u,v)}. \tag{5.16}$$

Hence, the DQE can be written as:

$$\mathrm{DQE}(u,v) = \frac{(\text{large area signal})^2\,\mathrm{MTF}^2(u,v)}{\mathrm{NPS}(u,v)\mathrm{SNR}_{\mathrm{in}}^2}. \tag{5.17}$$

In many medical systems the DQE of the digital detector is reduced at lower detector doses. This is due to additive noise components, e.g. instrumental noise, which often affect the DQE of the digital detector in the low-dose region [78, 79]. Therefore, the assumption of constant DQE for all detector doses may not be valid for low detector doses.

5.3 Previous work on simulated dose reduction in digital radiographic imaging

A number of methods of simulating dose reduction in digital radiographic images have been described previously [50-52, 76]. The methods have varying complexity and a short description of these methods is given here. All these methods are however based on the idea of simulating a reduction in detector dose, why the expression 'dose level' refers to detector dose when describing the methods for

simulating dose reduction. As the dose reduction is simulated as a change in the number of photons contributing to an image, a simulated reduction in detector dose is equivalent to a simulated reduction of all other relevant dose measures. If the X-ray system is linear, the change in detector dose can be expressed as the change in pixel value.

Veldkamp et al. [52] used a relatively simple method of simulating dose reduction in digital chest radiographic images. Image noise was measured as the standard deviation and dose reduction was simulated by scaling the pixel values of the raw data original image and then adding a random number to each pixel value. The random number was derived from a Gaussian distribution with zero mean and a standard deviation depending on the pixel value concerned. The method was evaluated by comparing the standard deviation and NPS in images that were simulated to have been acquired at a lower dose level to the standard deviation and NPS in images that were actually acquired at a lower dose level. Not surprisingly, although the results revealed that the standard deviations of the simulated images matched those of the real low-dose images, the NPS of the images were different.

Saunders and Samei [50] presented a method of modifying the image quality parameters of digital radiographic images. The noise modification routine was based on the creation of a noise image that was added to an essentially noise-free full-dose image in order to simulate the image that would have been acquired at a lower dose. The noise image was created by multiplying an uncorrelated Gaussian noise array by a noise frequency filter. The noise frequency filter was created by taking the square root of the NPS of the system. Assuming that the noise correlations were both radially symmetric and independent of detector dose, different noise magnitudes could be obtained by linearly scaling the pixel values of the full-dose image before addition of the created noise image. When adding the noise image to the scaled full-dose image, the variation in noise over the image was taken into account by adjusting the magnitude of the noise according to the local mean pixel value in each area of the image. The noise modification routine was evaluated by comparing the obtained NPS in dose reduced flat-field images to theoretically determined NPS, and the results from this evaluation indicated that the noise modification routine could be used to simulate the noise properties of an imaging system.

Båth et al. [51] described a method similar to that of Saunders and Samei [50], based on the creation of a noise image which, when added to an original image, resulted in an image with the same noise properties as an image actually acquired at a lower dose level. The method differed from that described by Saunders and Samei in that the method by Båth et al. accounted for the quantum noise present in the original image, while Saunders and Samei assumed an essentially noise-free full-dose image. Båth et al. created a noise image by filtering white noise with the frequency components given by the difference in NPS between the lower dose level and the

original dose level (not assuming radial symmetry). Information about the NPS at the two dose levels was determined from flat-field images acquired at the corresponding dose levels. Noise variations over a non-homogeneous image were accounted for by adjusting the individual pixel values in the noise image according to the pixel values in the original image. The created noise image was then added to the scaled original image to obtain an image that was simulated to be acquired at the lower dose level. The method was validated both by comparing the NPS of a simulated dose-reduced flat-field image to the NPS of a flat-field image actually acquired at the lower dose, and by visually comparing the noise characteristics of a simulated dose-reduced image of an anthropomorphic chest phantom with the noise characteristics of an image of the phantom actually acquired at the lower dose. Both comparisons showed good agreement between the simulated images and the images actually acquired at the lower dose level.

A method dedicated to simulating dose reduction in chest tomosynthesis images was presented in 2007 by Li and Dobbins [76]. This method was also based on the principle of creating noise images which, when added to the original images, resulted in images simulated to be acquired using a lower exposure. The noise images were created by filtering white noise with the NPS of the system. The NPS of the system was obtained from flat-field projection images from a tomosynthesis scan. As it was found that the NPS did not vary substantially between the different projection images, the NPS of the system was obtained by averaging the NPS from all angular projections. Additionally, the NPS was assumed to be radially symmetric and to have a shape that was constant over different detector doses. In order to adjust the spatial variance in the noise image according to the non-homogeneous background in a clinical image, the relationship between image variance and mean pixel intensity was determined, and the pixel values in the noise image were then adjusted accordingly. The created noise image was added to the full-dose image to simulate an image that had been acquired at a lower dose level. Subjective evaluation indicated that the noise in the simulated low-dose tomosynthesis images was similar to the noise in a tomosynthesis image actually acquired using a lower dose, although the method was not thoroughly validated.

5.4 Summary of Paper II

5.4.1 Background

The method of simulating dose reduction in digital radiographic systems described by Båth et al. was briefly presented above [51]. A limitation of this method is however that it is based on the assumption that the DQE of the system is constant over: 1) the dose variation between the original dose level and the dose level of the flat-field image that is closest to the original dose level, 2) the dose variation between the simulated dose level and the dose level of the flat-field image that is closest to the

simulated dose level, and 3) the dose variations that may occur over a clinical image. The validity of these assumptions can be questioned in the case of chest tomosynthesis due to the low exposures used for the acquisition of the projection images, as it is known that additive noise components often affect the DQE of the detector in the low-dose region. The aim of the study presented in Paper II was, therefore, to modify the method previously described by Båth et al. so that variations in DQE between different detector doses and possible variations in NPS between different angular projection images could be taken into account, thereby making the method more suitable for simulating dose reduction in tomosynthesis images.

5.4.2 Theory

The aim of the method presented in Paper II was to create a noise image that, when added to the scaled original image, resulted in an image with the same noise properties as an image actually acquired at a lower dose level. Hence, the first step in the dose reduction method was to scale the pixel values in the original image, $Im_{(x,y)_{orig}}$ according to:

$$Im(x.y)_{orig,scaled} = Im(x,y)_{orig}\frac{D_{sim}}{D_{orig}} \tag{5.18}$$

where D_{orig} and D_{sim} are the original and simulated dose levels, respectively.

In order to obtain the correct noise properties in the simulated image, an appropriate noise image must be added to the scaled original image. An original noise image was created by assigning normally distributed, floating point, pseudorandom numbers with a mean of zero and a standard deviation of one, to the pixels. The number of pixels and pixel size of the noise image were chosen to match those of the original image. The noise image added to the scaled original image was filtered with a frequency filter to obtain an NPS equal to the difference in NPS of the simulated and original dose levels. As the relative standard deviation is unaffected by scaling, the variance of the pixel values (σ^2) in the scaled image is given by:

$$\sigma^2{}_{Im(x,y)_{orig,scaled}} = \sigma^2{}_{Im(x,y)_{orig}}\left(\frac{D_{sim}}{D_{orig}}\right)^2 \tag{5.19}$$

where $\sigma^2{}_{Im(x,y)_{orig,scaled}}$ and $\sigma^2{}_{Im(x,y)_{orig}}$ are the variances of the pixel values in the scaled original image and the original image, respectively.

Since σ^2 is equal to the integral of the NPS, the NPS is also scaled correspondingly, and the NPS of the scaled original image is given by:

$$NPS(u,v)_{Im_{orig,scaled}} = NPS(u,v)_{D_{orig}} \left(\frac{D_{sim}}{D_{orig}} \right)^2 . \quad (5.20)$$

The NPS of the system at different detector doses can be determined from flat-field images acquired at various dose levels. In the most basic situation, one can imagine simulated dose reduction of a homogeneous image and that the flat-field images used to determine the NPS at different detector doses are acquired exactly at dose levels D_{orig} and D_{sim}. The NPS of the noise image that is added to the original image is then given by:

$$NPS(u,v)_{Im_{noise}} = NPS(u,v)_{D_{sim}} - NPS(u,v)_{D_{orig}} \left(\frac{D_{sim}}{D_{orig}} \right)^2 . \quad (5.21)$$

Note that as the NPS is determined in the frequency domain the noise image created must be Fourier transformed before applying the filter with frequency components given by the square root of Eq. 5.21.

If the image in which the dose is to be reduced is not homogeneous, the noise image that is to be added to the original image must also be adjusted according to the dose variation in the original image. The pixel variance of the original noise image is given by:

$$\sigma^2_{Im_{noise}} = \sigma^2_{D_{sim}} - \sigma^2_{D_{orig}} \left(\frac{D_{sim}}{D_{orig}} \right)^2 \quad (5.22)$$

while to take the local dose variations into account, the pixel variance at each location of the noise image, $\sigma^2_{Im(x,y)_{noise}}$, should be given by:

$$\sigma^2_{Im(x,y)_{noise}} = \sigma^2_{D_{Im(x,y)_{sim}}} - \sigma^2_{D_{im(x,y)_{orig}}} \left(\frac{D_{sim}}{D_{orig}} \right)^2 . \quad (5.23)$$

The pixel values in the original noise image should thus be corrected by:

$$\mathrm{Im}(x,y)_{\mathrm{noise,corrected}} = \mathrm{Im}(x,y)_{\mathrm{noise,uncorrected}} \sqrt{\frac{\sigma^2_{D_{\mathrm{Im}(x,y)_{\mathrm{sim}}}} - \sigma^2_{D_{\mathrm{Im}(x,y)_{\mathrm{orig}}}} \left(\frac{D_{\mathrm{sim}}}{D_{\mathrm{orig}}}\right)^2}{\sigma^2_{D_{\mathrm{sim}}} - \sigma^2_{D_{\mathrm{orig}}} \left(\frac{D_{\mathrm{sim}}}{D_{\mathrm{orig}}}\right)^2}}. \qquad (5.24)$$

An additional complication in the simulated dose reduction is that the acquired flat-field images used to determine the NPS at various dose levels are not acquired at the exact dose levels D_{orig} and D_{sim}. Rather, the flat-field images may be acquired at dose levels D_1 (a dose level close to D_{sim}) and D_2 (a dose level close to D_{orig}). In this case, the NPS will be determined at dose levels slightly different from those of interest. If the DQE is not constant over the dose levels D_1 and D_{sim}, and D_2 and D_{orig}, respectively, correction of the NPS in the noise image will be necessary to obtain the correct result. Assuming that the MTF is constant over different dose levels, the relationship between the NPS at two different dose levels, D_a and D_b, between which the DQE varies, is given by:

$$\mathrm{NPS}(u,v)_{D_a} = \mathrm{NPS}(u,v)_{D_b} \frac{D_a}{D_b} \frac{\mathrm{DQE}(u,v)_{D_b}}{\mathrm{DQE}(u,v)_{D_a}} \qquad (5.25)$$

where $\mathrm{DQE}(u,v)_{D_a}$ and $\mathrm{DQE}(u,v)_{D_b}$ are the DQE at the dose levels D_a and D_b, respectively. Hence, in this case, the NPS of the created noise image is given by:

$$\begin{aligned} \mathrm{NPS}(u,v)_{\mathrm{Im}_{\mathrm{noise}}} = & \frac{D_{\mathrm{sim}}}{D_1} \frac{\mathrm{DQE}(u,v)_{D_1}}{\mathrm{DQE}(u,v)_{D_{\mathrm{sim}}}} \mathrm{NPS}(u,v)_{D_1} \\ & - \frac{D^2_{\mathrm{sim}}}{D_{\mathrm{orig}} D_2} \frac{\mathrm{DQE}(u,v)_{D_2}}{\mathrm{DQE}(u,v)_{D_{\mathrm{orig}}}} \mathrm{NPS}(u,v)_{D_2} \end{aligned} \qquad (5.26)$$

By making the assumption that the DQE surface has a constant shape over different dose levels, the expression for DQE given in Eq. 5.17 can be inserted into Eq. 5.26 giving (as σ^2 is equal to the integral of the NPS):

$$\mathrm{NPS}(u,v)_{\mathrm{Im}_{\mathrm{noise}}} = \left(\frac{\sigma_{D_{\mathrm{sim}}}}{\sigma_{D_1}}\right)^2 \mathrm{NPS}(u,v)_{D_1} - \left(\frac{D_{\mathrm{sim}}}{D_{\mathrm{orig}}}\right)^2 \left(\frac{\sigma_{D_{\mathrm{orig}}}}{\sigma_{D_2}}\right)^2 \mathrm{NPS}(u,v)_{D_2}. \qquad (5.27)$$

5.4.3 Validation

In the study described in Paper II, it was assumed that the DQE surface has a constant shape over the relevant dose levels. By making this assumption, DQE variations can be accounted for simply by determining the pixel variance as a function of detector dose. As mentioned above, the relationship between pixel variance and detector dose is obtained from flat-field images acquired at various dose levels. The ratio between the mean pixel value and the variance as a function of detector dose for the GE tomosynthesis system, determined from ROIs in ten consecutive tomosynthesis projection angles at each dose level, is shown in Figure 5.1. As can be seen, the ratio between the ROI mean and variance is constant at higher detector doses (pixel values), but decreases at lower detector doses. This can be interpreted as a decrease in DQE at these lower detector doses.

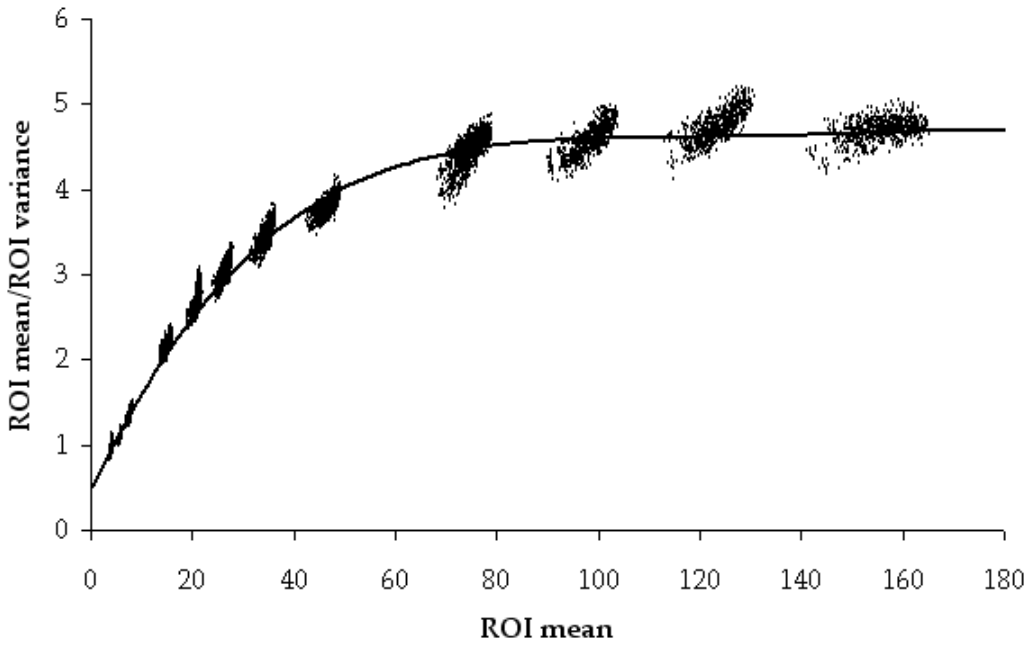

Figure 5.1. A plot of the ratio of pixel mean to pixel variance vs. pixel mean for ROIs obtained from flat-field images acquired at different dose levels. A quartic polynomial has been fitted to the data. Each group of data points represent ROIs from the same ten consecutive tomosynthesis projection angles acquired at the same dose level. (Adapted from Paper II.)

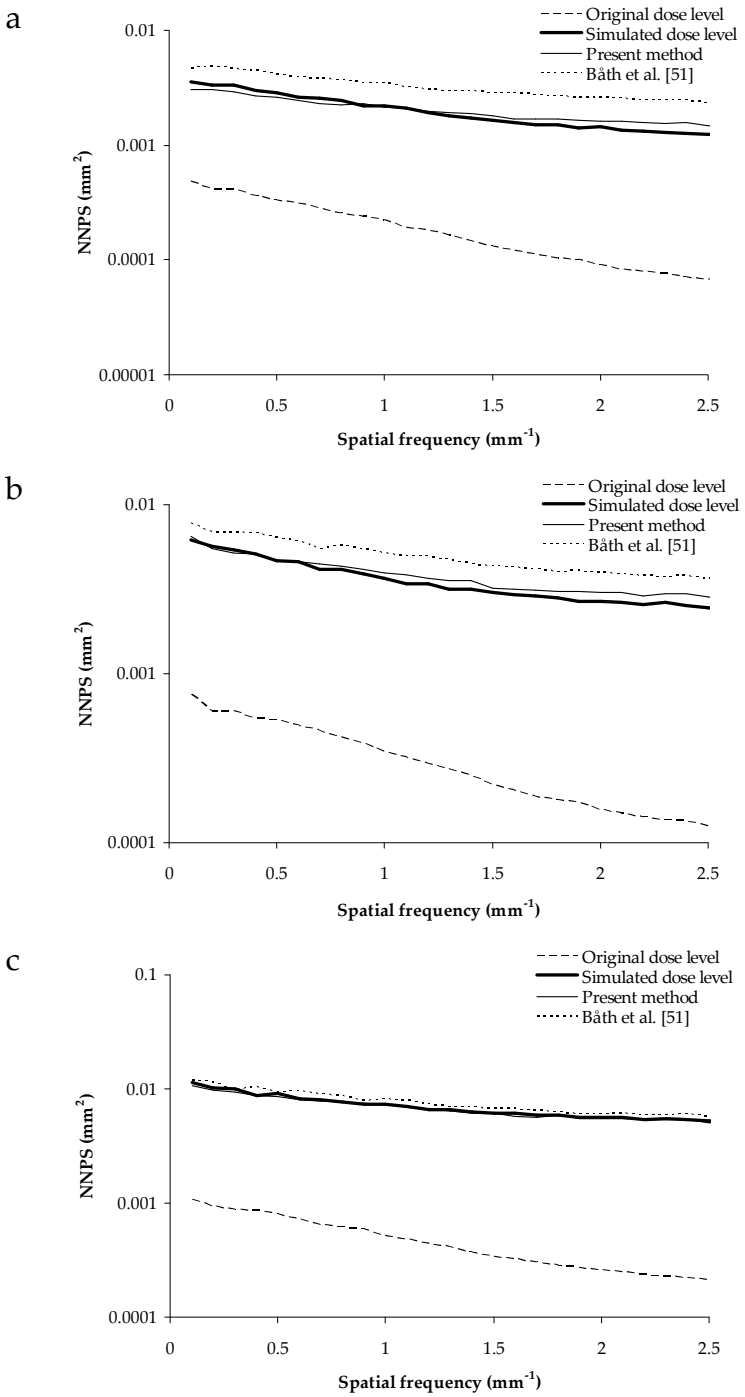

Figure 5.2. Examples of radially averaged NNPS in the high detector dose (0 mm Al) (a), medium detector dose (8 mm Al) (b) and low detector dose (18 mm Al) (c) regions of the aluminium phantom tomosynthesis projection images. The dashed line represents the NNPS of an image acquired using the original dose level (100 %) and the heavy line represents an image actually acquired using the simulated dose level (17 % of the original exposure). The light line represents the NNPS for the simulated image at a dose level corresponding to 17 % of the original dose level, using the method described in Paper II. The NNPS of the simulated image at 17 % of the original dose level using the method described by Båth et al. [51] is shown for comparison (dotted line). (Redrawn from Paper II.)

The method of simulating dose reduction was validated using different phantoms. For example, validation included comparisons of the NPS in simulated dose-reduced images of an aluminium phantom consisting of two regions containing aluminium of different thicknesses (8 and 18 mm Al), and an anthropomorphic chest phantom (Alderson lung/Chest Phantom RS-320; Radiology Support Devices, Long Beach, CA, USA), with the NPS in images of the phantoms actually acquired at a lower dose level. The NNPS of the three different detector dose regions (0, 8 and 18 mm Al) in the aluminium phantom projection images are shown in Figure 5.2. The aluminium phantom images were reduced to a dose level corresponding to 17 % of the original dose level. As can be seen in Figure 5.2, the method of simulating dose reduction described in Paper II resulted in an image with approximately the same noise properties as an image actually acquired at the lower dose level. The NNPS obtained using the method described by Båth et al. [51] (no correction for variations in DQE) is shown for comparison.

Figure 5.3 shows regions from reconstructed tomosynthesis projection images of the anthropomorphic chest phantom after simulated dose reduction to 20 % of the original dose level, together with the corresponding region from the original image and an image actually acquired at the simulated dose level. As the reconstructed tomosynthesis section images can not be expected to be linear, the NPS of the cut-outs shown in Figure 5.3 was normalized by dividing the NPS of a given image by the square of the difference in the mean pixel value at two different locations in the images. In this way, a scaled NPS was obtained that could be used to compare the NPS of images with different pixel value distributions. The scaled NPS of the images in Figure 5.3 are shown in Figure 5.4.

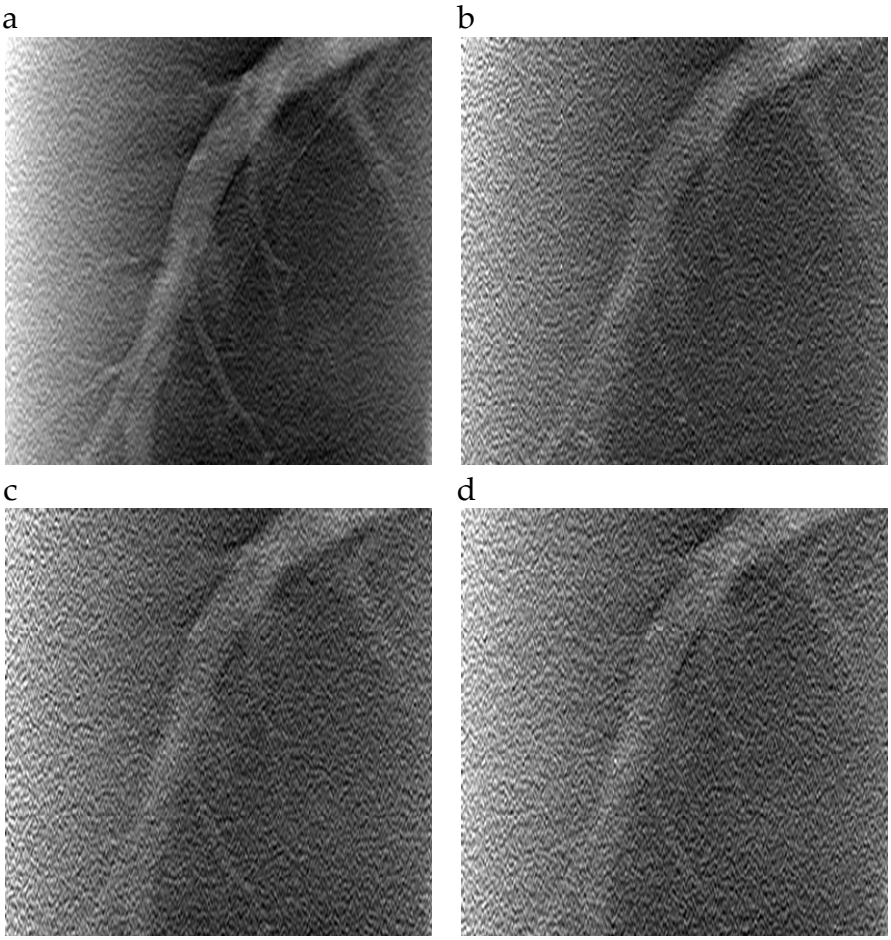

Figure 5.3. Regions from reconstructed section images from tomosynthesis examinations of an anthropomorphic chest phantom performed at dose levels of: (a) 100 % and (b) 20 %. The corresponding cut-outs of the 100 % dose examination after simulated dose reduction to 20 % of the original dose level using the method described in Paper II (c) and the method described by Båth et al. [51] (d) are also shown. (Adapted from Paper II.)

It might be difficult to appreciate the differences in noise properties between the images in Figure 5.3. However, as can be seen in Figure 5.4 the dose reduction method described in Paper II results in a simulated image with an NPS more closely matching the NPS of the image actually collected at the 20 % dose level, while the NPS of the image obtained using the method described by Båth et al. [51] for the simulated dose reduction was shown to have a slightly erroneous magnitude.

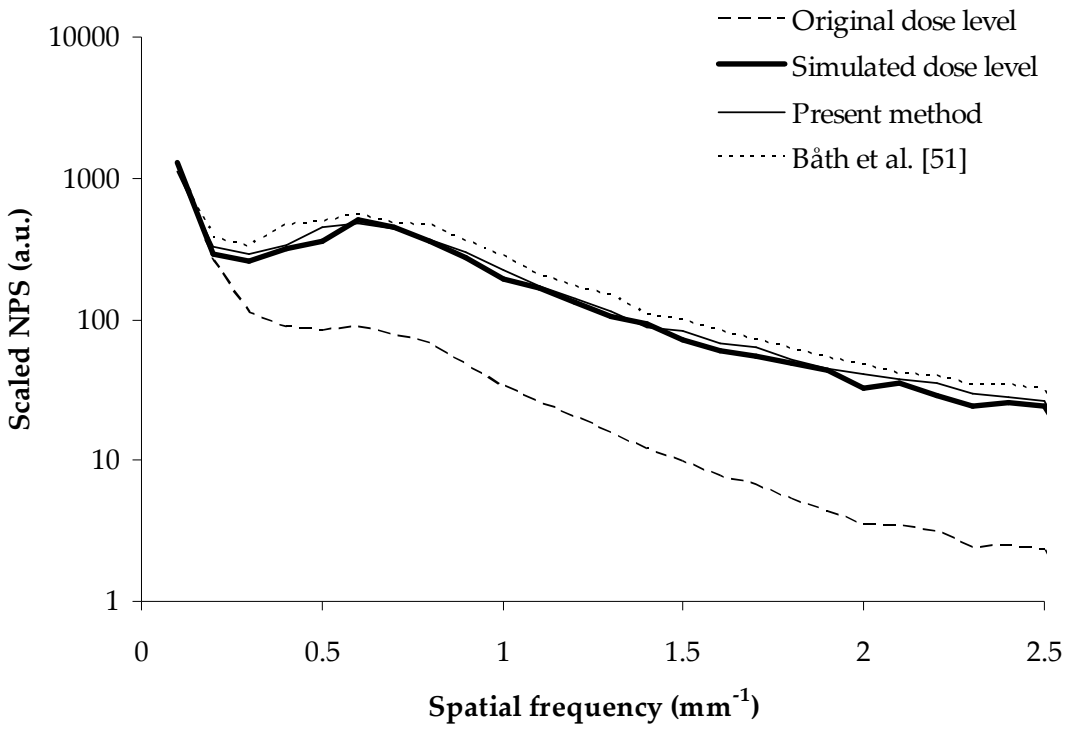

Figure 5.4. The radially averaged scaled NPS of the regions of the tomosynthesis section images presented in Figure 5.3. The dashed line represents the scaled NPS of the section image obtained at the original dose level (100 %), the heavy line represents the scaled NPS of the section image acquired at 20 % of the original dose level, the light line represents the scaled NPS of the 100 % image dose reduced to the 20 % dose level using the method described in Paper II, and the dotted line represents the scaled NPS of the 100 % image dose reduced to the 20 % dose level using the method described by Båth et al. [51]. (Adapted from Paper II.)

One of the original dose tomosynthesis projection images included in the reconstruction of the section image, of which a region is shown in Figure 5.3a, has a mean pixel value of 52, which lies in the dose region where the ratio between pixel mean and pixel variance starts to decrease (Figure 5.1). This illustrates the necessity of taking the change in DQE into account when simulating dose reduction in tomosynthesis projection images.

5.4.4 Step-by-step description of the simulated dose reduction method

The method of simulating dose reduction in tomosynthesis described in Paper II may, at first, seem rather complicated. Therefore, a thorough, step-by-step description of the simulation process is given here. A schematic flow cart of the dose simulation process is given in Figure 5.5.

1. The first step involves the acquisition of flat-field images at different dose levels. The flat-field images should preferably be acquired using the same

radiation quality as the clinical images that are to be simulated. Therefore, to simulate dose reduction of chest tomosynthesis images, a homogeneous phantom, with an attenuation corresponding to the average patient, should be used to acquire the flat field images. Note: the anti-scatter grid should be removed during the acquisition of the flat-field images in order to avoid artefacts due to the grid lines in the determination of the NPS. Instead, an air gap technique can be used to reduce the effect of scattered radiation.

2. The relationship between pixel value and standard deviation should be determined for each dose level and angular projection. The ratio of the pixel mean to pixel variance can then be plotted against the pixel mean of the ROI, and a function can be fitted to the data. In the case of tomosynthesis, where a relatively large number of projection images are included in each examination (60 for the GE VolumeRAD system), this procedure will result in a large amount of data. Data handling can be simplified by pooling the data from, e.g., ten consecutive angles before plotting the values, thus, each angular interval will be represented by its own function. The functions can be considered valid for the mean projection angle in each angular interval, and linear interpolation between the functions can be used to obtain the correct values for other projection angles.

3. The NPS of each flat-field image should now be determined, not assuming radial symmetry. The central part of each flat-field image should be divided into non-overlapping ROIs and for each ROI the NPS should be determined using Eq. 5.11. The NPS of each flat-field image can then be determined by averaging the NPS of the ROIs.

   The simulated dose level (D_{sim}) should now be determined as a percentage of the original dose level (D_{orig}). The pixel values in the original image can then be scaled correspondingly. The two flat-field images that closest match the mean pixel values of the original image and the simulated image should now be identified. As it cannot be assumed that the slope of the NPS is constant for different angular projection images, the flat-field images should also be matched according to angular projection.

4. A noise image should now be created in the spatial domain. This involves assigning values to the pixels from normally distributed, floating point, pseudorandom numbers with a mean of zero and a standard deviation of one. After Fourier transforming the noise image, a filter with frequency components given by the square root of the NPS of the noise image should be applied. The NPS of the noise image is determined using the NPS of flat-field images with mean pixel values close to D_{orig} (D_1) and D_{sim} (D_2), and the

standard deviations (σ) at D_{orig}, D_{sim}, D_1 and D_2, according to Eq. 5.27. In this way, the possible difference in DQE that might be found between D_{orig} and D_1, and D_{sim} and D_2, respectively, (so-called global DQE variations), can be accounted for.

5. As the detector dose may vary considerably over a clinical image, the DQE can also vary over the image (so-called local DQE variations). After correcting the noise image for global DQE variations, the noise image should be inversely Fourier transformed and the real part corrected for local detector dose variations according to Eq. 5.24.

6. The created (and corrected) noise image can finally be added to the scaled, original clinical image in order to simulate an image that has been acquired at the simulated dose level.

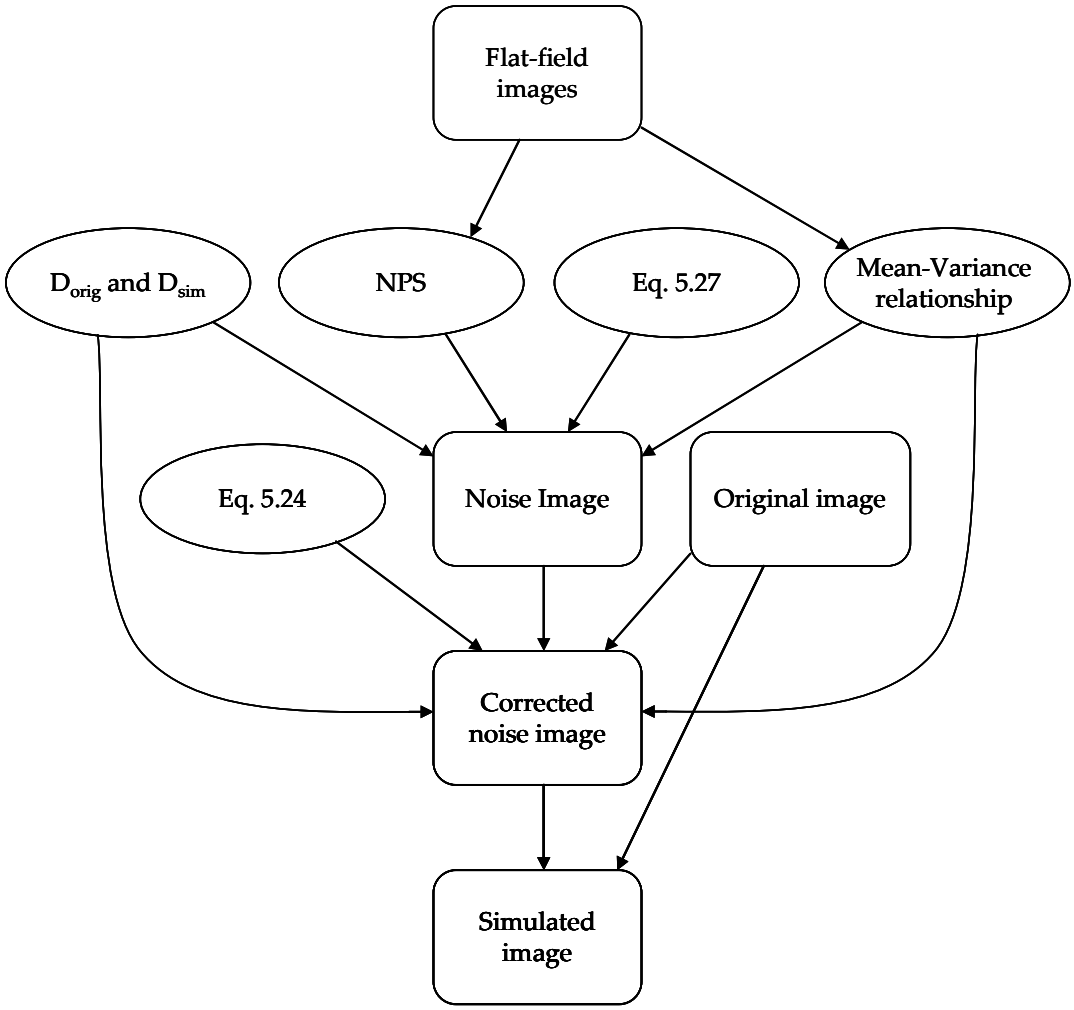

Figur 5.5. Schematic flow chart of the simulated dose reduction process.

"Before beginning a Hunt, it is wise to ask someone what you are looking for before you begin looking for it."

-A.A. Milne

6 Nodule simulation

Simulating pathology in radiological images is a challenging task. Depending on the imaging technique, different criteria must be fulfilled for the simulated pathology to resemble real pathology. In conventional projection radiography the overlapping anatomy will obscure much of the pathology, reducing the possibility of visualizing the exact delineation of pathological structures such as lung nodules. Therefore, it is often deemed unnecessary to achieve perfect simulation of the margins and shape of the lung nodules in conventional chest radiography. Thus, many of the methods of simulating nodules in conventional chest radiography images are based on the creation of nodule phantoms [58] or the use of mathematically described nodule profiles [7, 45].

In CT examinations the situation is the reverse, as most of the obscuring anatomy is removed from the images. The pathological structures are thus clearly delineated in most cases, and it is therefore important to mimic the margins and shape of the structure in the simulation process. In the methods simulating lung nodules in CT images different approaches are applied to create nodules with a realistic shape. For example, Sun et al. [60] simulated nodules by using several ellipsoids with different axial lengths, combined so that all shared the same centre. Li et al. [59] instead created three-dimensional nodules by modelling the nodules as two-dimensional contrast-profile equations on sequential CT slices.

Chest tomosynthesis can be seen as a combination of conventional radiography and CT. Much of the overlaying anatomy is removed from the reconstructed tomosynthesis images, but not completely removed due to the limited depth resolution of tomosynthesis [22]. The result is that, in most cases, the pathological structures are clearly visible. However, some overlapping anatomy is still present in the images, which needs to be accounted for if the simulated nodules are to be inserted directly into the reconstructed tomosynthesis section images. Another complication in the case of tomosynthesis is the fact that there is no standardised calibration procedure for the pixel values in the reconstructed tomosynthesis section images. It is thus difficult to determine the pixel values for a simulated nodule of a certain density in the reconstructed section image. In the case of CT, where the pixel values are calibrated in Hounsfield units (CT number), it is easier to insert a simulated nodule of a specified density directly into the reconstructed CT image. (A summary of some of the previous work on simulating lung nodules is given in Section 6.5.)

In order to avoid problems associated with remaining overlapping anatomy and uncalibrated reconstructed images, it was found in this work (Paper III) that a suitable approach for simulating lung nodules in chest tomosynthesis images is to

insert the simulated nodule into the raw-data projection images of the tomosynthesis examination, before reconstruction of the tomosynthesis section images. As described further in Section 6.7, the simulated nodules are inserted into the tomosynthesis projection images by reducing the pixel values in the region of the nodule according to the reduction in detector signal that would have occurred if the nodule had actually been present in the patient at the time of the acquisition of the tomosynthesis projection images. Apart from the attenuation of the radiation passing through the nodule, the detector signal is affected by scattered radiation and the MTF of the detector. These factors must, therefore, be taken into account in the nodule simulation process. In Sections 6.2 and 6.3, thorough descriptions of the determination of scattered radiation and MTF are therefore given. A common way to evaluate a method of creating simulated pathology is to perform an ROC study to evaluate the similarities or differences between simulated and real pathology. A review of ROC is therefore given in Section 6.4.

6.1 Nodule characteristics

Pulmonary nodules are a common finding in thoracic radiology. A nodule is defined as a rounded opacity completely surrounded by lung parenchyma that is smaller than 3 cm in diameter [84-87]. In many cases, nodules are caused by inflammatory lung disease and are thus benign [84-88], but in some cases the nodule is malignant. A malignant nodule may either be an early stage of lung cancer (84 % of all malignant lung nodules [89]) or a metastasis from a malignant tumour in a different part of the body [84, 88]. Most lung nodules are detected incidentally on conventional chest radiography examinations or CT examinations performed for other purposes [89]. Wahidi et al. [90] summarized the data from eight large lung cancer screening trials and found that the prevalence of at least one lung nodule in a patient varied between 8 and 51 %. Although the prevalence of lung nodules varied between the studies, it can be concluded that thoracic radiologists often encounter one or more nonspecific lung nodule in a patient. The morphological features of the nodule can in such cases be helpful when trying to differentiate benign nodules from malignant ones. Evaluation of nodule characteristics using radiographic follow-up examinations is a common procedure, for both incidentally and intentionally detected nodules [84-88].

The size of a nodule is an important factor in determining the risk of malignancy; the risk increasing with nodule size [84, 85, 87, 88]. By analysing nodule findings in CT screening for lung cancer, Henschke et al. [91] found that less than 1 % of nodules ≤ 5 mm in diameter were malignant. The corresponding fraction for nodules ≤ 10 mm in diameter was 7 %. Wormanns et al. [86] concluded that a nodule diameter of 10 mm represents an important threshold between a probably malignant lesion and a probably benign lung nodule. Nodule size alone should, however, not be used to determine the risk of malignancy. In addition, the density, margins and internal

characteristics of the nodule can provide useful information for the task of differentiating between malignant and benignant nodules.

Pulmonary nodules can be divided into three main categories according to density: nonsolid, partly solid and solid [91]. Solid nodules are most common, but they are less likely to be malignant than nonsolid and partly solid nodules. In the study by Henschke et al. [91] it was found that only 7 % of the solid nodules were malignant. Of the nonsolid nodules, approximately 18 % were malignant, while 60 % of the partly solid nodules were malignant. The nodule margins can be defined as smooth, lobulated, irregular or spiculated [84]. Nodules with smooth, well-defined margins have the lowest risk of being malignant [88]. However, approximately 20 % of all malignant nodules also show smooth, well-defined margins [84, 88]. A lobulated margin can be the result of uneven growth, often associated with malignancy [84, 87, 88]. Also, nodules with irregular or spiculated margins have a high risk of being malignant [84, 86, 88]. The situation is further complicated by the fact that most of the features associated with malignant nodules can also be found among benign nodules [84, 86-88], increasing the risk of incorrect diagnosis.

Apart from nodules found in patients with a known history of bone malignancy, calcification is a feature often associated with benign nodules. Studies have, however, shown that calcification is also present in approximately 10 % of lung cancer cases [92]. Therefore, it is important to analyse the appearance of calcification. Central, diffuse, solid, laminated or "popcorn-like" patterns of calcification are associated with a high probability of benignancy [84-88]. A common internal feature of nodules is the presence of cavities. The wall thickness of the cavity can be used as an indicator of malignancy. If the walls of the cavity are thinner than 4 mm there is a high probability of benignity, while wall thickness greater than 16 mm is a strong indicator of malignancy [84, 85, 87, 88].

The Fleischner Society [93] has provided guidelines for the management of small pulmonary nodules. According to these guidelines, nodules ≤ 4 mm in diameter can be disregarded, as the risk of future malignancy is less than 1 % for these nodules. Exceptions are nodules found in patients with known history of malignancy or known risk factors for malignancy. For these patient categories, follow-up after 12 months is recommended to verify that no change in nodule volume has occurred. For nodules larger than 4 mm but smaller than 6 mm the recommendation is follow-up after 12 months for low-risk patients and after 6 months for patients with a high risk of malignancy. If the nodule size then remains unchanged the Fleischner Society recommends no further follow-up. If the nodule is > 6-8 mm in diameter it is recommended that the first follow-up is performed after 6 months for low-risk patient and 3 months for high-risk patients, but, also for these nodules, no further follow-up is recommended unless the size of the nodule has increased. For nodules larger than 8 mm in diameter the Fleischner Society recommends follow-up on three

occasions (after 3, 9 and 12 months) and additional investigations using, for example, contrast-enhanced CT, positron emission tomography or needle biopsy.

6.2 Scattered radiation in chest radiography imaging

Scattered radiation is present, to some extent, in all medical X-ray images. It is well-known that scattered radiation results in the degradation of image contrast and this must, therefore, be taken into account in nodule simulation. Several studies on scattered radiation in chest radiography examinations have shown that the amount of scattered radiation varies between different regions of the chest [94-97]. The amount of scattered radiation can be quantified using either the scatter fraction (SF) or the scatter-to-primary ratio (SPR). While the SPR is defined as the ratio between scattered and primary photons, SF is defined as the ratio between the scattered photons and the total number of photons.

The amount of scattered radiation reaching the imaging detector in radiography examinations can be reduced by using an air gap between the object and the detector or an anti-scatter grid. The anti-scatter grid consists of an array of very thin, parallel strips of lead foil, separated by a low-attenuating material, commonly aluminium [98]. This results in attenuation of the scattered radiation by the lead foils, while the non-scattered photons pass through the grid in the aluminium spaces between the lead foils. The effectiveness of the grid is determined by the depth of the lead foils in the direction of the X-ray beam and the thickness of the lead foils in the plane perpendicular to the central axis of the X-ray beam, as well as by the separation between the lead foils. The specifications of a grid often include values of grid ratio and grid strip density, where the grid ratio is defined as the ratio between the lead foil depth and separation. A grid with a lead foil depth of 3 mm and a separation of 0.25 mm will consequently have a grid ratio of 12 (or 12:1). The grid strip density is given as the number of lead foils per centimetre of the grid.

Many studies have compared the efficiency of scatter reduction using an air gap and an anti-scatter grid. Niklason et al. [94] constructed a phantom designed to provide scatter fractions similar to those found in measurements of real patients undergoing a chest radiographic examination. The phantom was then used to measure the difference in SF when using an anti-scatter grid or an air gap using a tube voltage of 120 kV. They found that scattered radiation could account for more than 90 % (SF > 0.9) of the radiation exiting the patient at the location of the central mediastinum. The corresponding scatter fractions in the lung and retrocardiac regions were 0.55 and 0.81, respectively. Using an anti-scatter grid with a ratio of 12:1 during the examination reduced the SFs substantially (lung 0.26, retrocardiac area 0.46 and mediastinum 0.57). The effect of using a 30 cm air gap between the phantom and the imaging detector was not as great, although the SFs were also significantly reduced in this case (lung 0.35, retrocardiac area 0.64 and mediastinum 0.87).

Jordan et al. [96] measured the SF in 20 PA chest radiographs, acquired using a grid with the same ratio as in Niklason et al. (12:1) [94], and a tube voltage of 125 kV. In this study a posterior beam stop technique was used for scattering measurements, and somewhat higher SFs than those reported by Niklason et al. were found, namely: lung 0.27 (range, 0.19-0.36), retrocardiac area 0.66 (range, 0.58-0.80) and mediastinum 0.68 (range, 0.49-0.82). However, as can be seen by the range of the values reported by Jordan et al. the values of SF varied considerably with patient size, which may partly explain the difference in SFs between the two studies.

Ullman et al. [97] performed Monte Carlo simulations of a digital chest imaging system using a chest voxel phantom. The simulations were performed using a tube voltage of 145 kV and also in this work a grid ratio of 12:1 was assumed. The variation in SPR between different parts of the phantom image was calculated on a pixel-to-pixel basis, and the results revealed that the SPRs were higher in regions of higher density (mediastinum and heart region) than in the lung region. However, it was also shown that the SPR in the lung region increased close to the interface between lung tissue and anatomical tissues of higher densities. Measuring SF in the central location of each anatomical region may thus lead to underestimation of the amount of scattered radiation in each region. A further explanation to the differences in SFs between Niklasson et al. [94] and Jordan et al. [96] may therefore be the fact that the SF values reported by Jordan et al. were means of SF values measured at many different locations in each anatomic region, while the values reported by Niklason et al. were measured in the centre of each anatomic region.

The effect on image contrast (C) due to scattered radiation can be expressed [82]:

$$C = C_p(1 - SF) \tag{6.1}$$

where C_p is the image contrast without the influence of scattered radiation. Hence, a SF of 0.27 in the lung region (as reported by Jordan et al. [96]) will result in a reduction in image contrast of 27 %. Therefore, not accounting for the scattered radiation in the nodule simulation process would lead to higher contrasts for simulated nodules than for real nodules with corresponding physical properties. In this work (Paper III) a constant SPR of 0.5 (equivalent to a SF of 0.33) was used in the nodule simulation process. Using this higher value of SF would result in 8 % lower nodule contrast than when using a SF of 0.27.

In a tomosynthesis examination, it can be expected that the SPR in a specific anatomical location may vary between the different angular projections. Recently, Ullman et al. [99] presented Monte Carlo simulations of a tomosynthesis examination performed using the GE Definium 8000 system with the VolumeRAD option. The simulations were performed using a voxel phantom created by a CT scan of an

anthropomorphic chest phantom (PBU-X-21, Kyoto Kagaku Co. Ltd, Kyoto, Japan), and threshold segmentation with a step density function. Monte Carlo simulations were used to create tomosynthesis projection images of the phantom, including primary photons, scattered photons and correlated noise. The signal contributions from scattered photons were calculated in a grid of 40×40 points. The calculations of signal contribution from scattered photons were then used to estimate the SPR at each grid point. As the tomosynthesis projection images have a resolution of 2022×2022 pixels, the SPRs at the grid points were interpolated from 40×40 points to 2022×2022 points using bilinear interpolation. The SPRs obtained from the Monte Carlo simulations were analysed by Svalkvist et al. [100] and it was found that the SPR at a specific location in the patient could vary by up to a factor of ten between the different angular projection images. However, despite this large variation in SPR, the resulting nodule contrast in the reconstructed tomosynthesis section images was not seriously affected by neglecting the angular SPR variations in the nodule simulation process. It was found, for example, that using the SPR for the zero-degree projection image throughout the entire simulation process generated an error in the resulting nodule contrast smaller than 10 %. Nevertheless, in the evaluation of the improved method for nodule simulation described in Paper IV the variations in SPR, both between different locations in the image and between different angular projection images, were accounted for in the simulation process.

6.3 MTF measurements

As described in Section 5.2.1, difficulties may arise when determining the MTF of a digital radiographic system. As the MTF describes the signal response of a system at a given frequency, information is required on all the frequencies included in the input signal (delta function) for correct estimation of the MTF. Due to the fact that aliasing (see Section 5.1.2) is present in most digital imaging systems, the system's response to a single delta function can not be used to adequately determine the MTF of the system. A thorough description of the effects of undersampling when determining the MTF of a digital imaging system is given by Dobbins [83]. One solution to the problem of determining the MTF of an undersampled system is to instead determine the pre-sampling MTF of the system. The pre-sampling MTF describes the system's response to a signal up to, but not including, the stage of sampling [82].

As mentioned in Section 5.2.1, the MTF can be described as the amplitude of the two-dimensional FT (as a function of spatial frequency) of the PSF of the system. The one-dimensional MTF can be described as [39]:

$$\mathrm{MTF} = \left|\mathrm{FT}\{\mathrm{LSF}(x)\}\right| \tag{6.2}$$

where LSF (the line spread function) is defined as the response of a system to a delta function, integrated over one variable and normalized to unit area [80]. The LSF can also be described as the response of the system to a 'line' delta function [80]. This definition is useful for the measurement of the MTF of a system, which is commonly performed using either the slit method or the edge method.

In the slit method, the LSF of the system is given by the convolution of the PSF with the slit. In order to avoid the influence of aliasing when determining the MTF of a digital system using the slit method, Fujita et al. [101] proposed a method in which the slit is positioned slightly tilted relative to the sampling coordinates (pixels). Due to the slight tilting of the slit, the pixel values along different pixel rows crossing the slit will correspond to slightly different samplings of the LSF. A finely sampled LSF of the system can thus be generated by combining sampling data from a number of different pixel rows crossing the slit. The MTF of the system, in the direction perpendicular to the slit, is then given by the FT of the finely sampled LSF. As the effective sampling distance is made smaller using this technique, the effect of aliasing will be eliminated and the pre-sampling MTF is obtained.

In the edge method, a sharp edge made of tungsten or lead is imaged. In the same way as for the slit method, the edge should be positioned slightly tilted relative to the sampling coordinates of the detector in order to avoid the effects of aliasing. The method of using a tilted edge device to measure the pre-sampling MTF for a digital radiographic system was first described by Samei et al. [102]. The pixel values in different pixel rows across the edge are sampled to generate an over-sampled edge spread function. The derivative of the edge spread function is the LSF perpendicular to the edge, which in turn is used to obtain the pre-sampling MTF of the system, in the same way as described for the slit method.

Opinions differ as to whether the slit method or the edge method is preferable for the determination of the pre-sampling MTF of a digital system. Dobbins et al. [82], for example, are of the opinion that the edge is more difficult to align with respect to the axis of the central beam than the slit, while Samei et al. [102], for example, are of the opinion that a slit is more difficult to fabricate and is more difficult to align to the radiation beam. However, Dobbins et al. and Samei et al. agree that the slit method results in less correct determination of the low frequencies than the edge method. In 2003 the International Electrotechnical Commission (IEC) defined an international standard for determination of the DQE of digital X-ray imaging devices [103]. According to this standard the pre-sampling MTF should be measured using the edge method. Ranger et al. later investigated the difference in DQE obtained using the slit method as described by Dobbins et al. [104], the edge method described by Samei and Flynn [105] and the edge method described by the IEC [103] in the determination of the MTF. The results revealed that the slit method resulted in 11 %

higher DQE than the method proposed by the IEC, while the edge method described by Samei and Flynn resulted in a 4.4 % higher DQE.

In the present work (Paper III), the one-dimensional MTF measurements of the GE Definium 8000 system with VolumeRAD option, necessary to take the detector resolution into account in the nodule simulations, were performed using the tilted slit method described by Fujita et al. [101] and a slit created by Båth et al. [78]. The slit consisted of two aluminium foils with a thickness of 10 μm placed between two carefully polished tungsten plates (thickness 2 mm, width 9 mm and length 30 mm) that were attached to a steel holder. A very narrow air gap was obtained when the two tungsten plates were screwed tightly together. The air gap (slit) was found to be 11±1 μm wide. The construction was mounted on a bottom plate, which allowed for rotation of the slit in two dimensions in order to simplify the alignment of the slit with the X-ray beam, and to obtain any desired angle between the slit and the sampling coordinates of the detector. Measurements of the pre-sampling MTF were performed both horizontally and vertically for the 0° projection and for two different oblique incident angles of the X-ray beam (9°, 17°). The measurements revealed that the horizontal MTF seemed to be unaffected by the incident angle of the X-ray beam, whereas the vertical MTF varied slightly between the different angles (see Figure 6.1).

The vertical MTF was assumed to be symmetric around the 0° projection (same for both positive and negative incident angels). Using this assumption, the vertical MTF for each tomosynthesis angle was estimated by performing cubic-spline interpolation using the determined vertical MTFs for the 0° projection and for the two different oblique incident angles of the X-ray beam (9°, 17°). The two-dimensional MTF for each angle MTF(u,v,α) was then estimated according to:

$$\mathrm{MTF}(u, v, \alpha) = \mathrm{MTF}(u,0) \cdot \mathrm{MTF}(0, v, \alpha) \tag{6.3}$$

where MTF(u,0) is the horizontal MTF and MTF(0,v,α) is the vertical MTF at angle α.

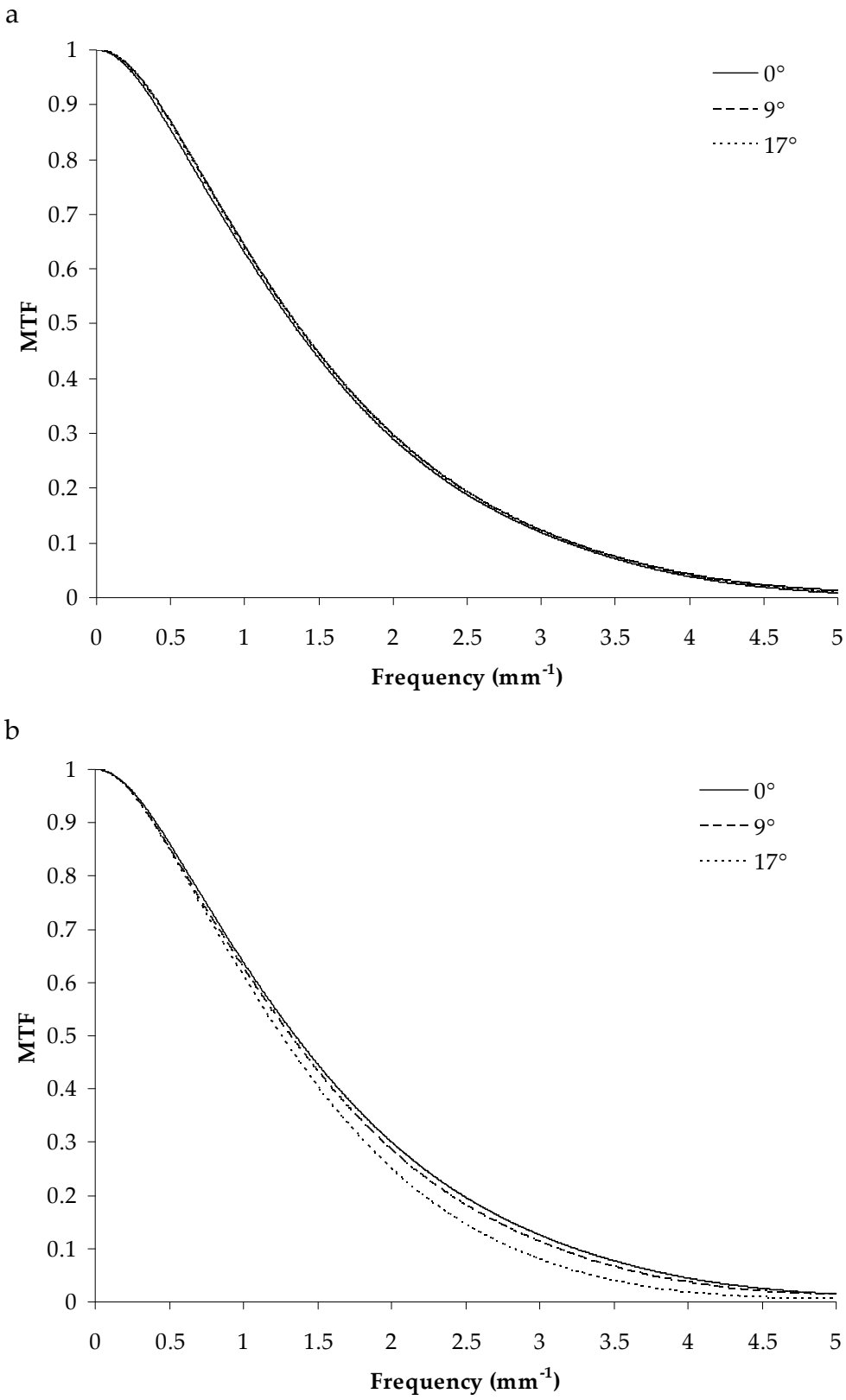

Figure 6.1. The horizontal (a) and vertical (b) MTF for the 0° projection and for two different oblique incident angles of the X-ray beam (9°, 17°) for the GE Definium 8000 system with VolumeRAD option.

6.4 Receiver operating characteristics

In the clinical situation, radiologists are constantly faced with the task of determining whether or not images of a patient show any signs of pathological changes. The possibility for the radiologist to make a valid decision can be increased by optimizing the viewing conditions, for example by ensuring that the quality of the image is adequate for the intended purpose. In return, image quality can be measured by analysing the performance of radiologists in specified decision tasks.

The sensitivity, also known as the true positive fraction (TPF), is a measure of the probability that a patient that actually has a disease is also judged to have that disease by the observer. The specificity, also known as the true negative fraction (TNF), is thus a measure of the probability that a healthy patient is judged to be healthy by the observer [106]. When conducting observer performance studies, the observers are often instructed to grade their confidence in each decision according to a rating scale, where a higher rating means that the observer is more confident that their decision is correct. Each rating is thus comparable to a threshold for the decision, which will vary between different observers. The choices of the decision thresholds are used in ROC analysis to establish the relationship between the TPF and the false positive fraction (FPF = 1 - specificity) [106]. Plotting the TPF against the FPF for each decision threshold gives an ROC curve. In Figure 6.2 an example of an ROC curve obtained using a six-level rating scale (five decision thresholds) is shown. A curve that is situated close to the diagonal (indicated by the dashed line in Figure 6.2) corresponds to a situation where the observer has been unable to differentiate between healthy and unhealthy patients. That is, for each threshold, the probability that the observer has made a correct decision is 50 %, which corresponds to the result one can expect if the decisions of the observer were based on pure guesswork. A curve situated close to the top left corner, such as that in Figure 6.2, corresponds to a situation where the observer more easily has been able to distinguish between healthy and unhealthy patients. The area under the ROC curve (A_z) is often used as a quantitative measure of observer performance; the value ranging between 0.5 (chance detection) and 1.0 (perfect detection) [106].

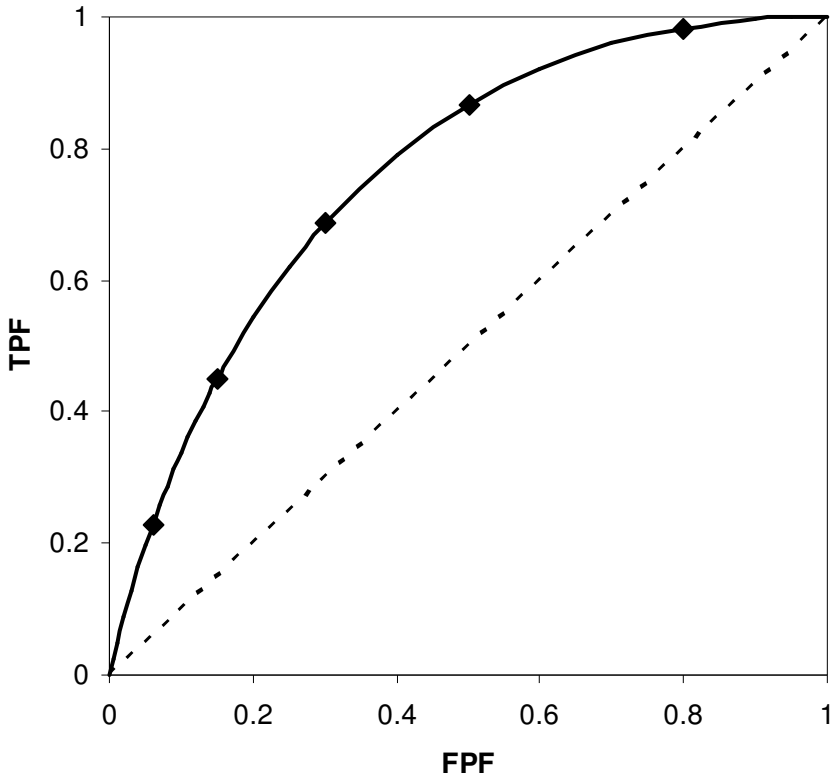

Figure 6.2. An example of a typical ROC curve. Each point on the curve corresponds to a decision threshold (six-level rating scale). The dashed line represents the situation where the observers are unable to distinguish between healthy and unhealthy patients.

The ROC analysis is often regarded as the gold standard when evaluating image quality by observer performance studies [41]. However, the method has some weaknesses when used to analyse images in which the disease is manifested by localised lesions within an organ [106]. This is e.g. the case when investigating the presence of nodules in the lung parenchyma. In these studies, each patient might have more than one abnormality, and in a situation where the observer misses a true abnormality in the images and instead, erroneously, suspects another location in the image to contain an abnormality, the two mistakes made by the observer will not be apparent. First the observer misses a true abnormality, which can be translated to making a false negative decision. Secondly, the observer erroneously suspects a location that in fact does not contain any abnormality, which can be translated to making a false positive decision. However, if using ROC analysis to evaluate the results from the study these two mistakes will cancel each other out as the decision on the case level will be correct (the patient does have an abnormality), although the decision was based on incorrect assumptions. In order to avoid such a situation the free-response ROC (FROC) paradigm [107] can be used.

According to the FROC paradigm, the observers are instructed to mark suspicious abnormalities in the images and for each marking grade their confidence in the marking being a true abnormality. Hence, instead of grading their overall confidence in the patient being healthy (or not), the observers identify suspicious abnormalities and grade their confidence in their own markings. For each abnormality noted in the image, it is established whether it is a true abnormality (true positive) or an erroneous mark (false positive). A FROC curve is then obtained by plotting the lesion localisation fraction (LLF) against the non-lesion localisation fraction (NLF) [106]. The LLF corresponds to the ratio between the number of true positive marks and the total number of lesions (abnormalities) present in each patient, while the NLF corresponds to the ratio between the false positive marks and the total number of patients included in the study [106]. As all false positive marks are included in the FROC curve, the area under a FROC curve can not be used as a quantitative measure of observer performance, as a higher number of false positive marks will yield a larger value. In order to compare the A_z values of two modalities and retain the benefits of performing the analysis on a lesion level instead of a patient level, alternative FROC (AFROC) curves can be plotted. The AFROC curve is obtained by plotting the LLF against the FPF [106]. In the case of the FROC paradigm, where multiple marks are possible in each case, the FPF is the ratio between the false positive mark with the highest confidence in a normal image and the total number of normal cases included in the study. Hence, the AFROC curve will, as in the case of the ROC curve, have a maximum A_z value of 1.0 [106]. Note, while the area under the ROC curve has a theoretical minimum value of 0.5, the area under the AFROC curve has a theoretical minimum value of 0 (if only false positive markings are made in the images).

6.5 Previous work on the simulation of lung nodules

As mentioned earlier, methods for simulation of lung nodules has previously been described for both conventional chest radiography and CT [7, 58-60]. When simulating nodules in conventional chest radiography images, the shape of the simulated nodules is of less importance, since overlapping anatomy will make delineation of the simulated nodules difficult. This is not the case when simulating nodules in chest CT examinations. Due to the major reduction of overlapping anatomy in CT images, both delineation and the internal characteristics of the nodule can be clearly visualized, increasing the need for more complex simulated structures in order to for them to resemble real lung nodules.

Samei et al. [58] created nodule phantoms by extracting the contrast characteristics of real nodules found in chest radiographic images. The optical density profiles across real nodules were obtained and converted into exposure contrast. The average diameter of each nodule was also estimated. The relationship between peak contrast and nodule diameter of the real nodules was used to establish the corresponding

characteristics of the simulated nodules. Nodule phantoms with the desired thickness profiles were then machined from Teflon®. These nodule phantoms could then be placed on the surface of a patient or anthropomorphic phantom during the acquisition of radiographic images, thereby introducing the nodule structures into clinical images. The contrast of the simulated nodules was evaluated by placing the nodule phantoms on a Lucite slab and acquiring a radiograph, in which the relationship between peak contrast and diameter of the nodule phantoms was investigated. The visual appearance of the nodule phantoms in the anatomical background was also investigated. This was accomplished by comparing the visual appearance of a nodule phantom inserted in images of an anthropomorphic chest phantom with the visual appearance of the corresponding real nodule that was used to establish the relationship between peak contrast and nodule diameter. The results showed that the peak contrast and diameter of the simulated nodules were in close agreement with the expected values. It was also found that the appearance of the nodule phantoms in an anatomic background was very similar to the visual appearance of real nodules.

Båth et al. [7] used a mathematically simulated so-called 'designer nodule' to create artificial nodules in digital chest radiographic images. The concept of a designer nodule was described by Burgess et al. [108] and is based on a mathematical description of a lung tumour profile, where the amplitude of the simulated nodule is defined as a function of nodule radius. Båth et al. inserted the simulated nodules into linear chest radiographic images by varying the pixel values in the radiographic images according to the contrast of the simulated nodules, and used these images to investigate to what extent the location of nodules influences the possibility for nodule detection. The simulated nodules were also used to investigate to what extent system noise and anatomical noise disturbs the detection of lung nodules. The method for simulating nodules was not evaluated by Båth et al. However, Burgess et al. had previously shown that the relationship between amplitude and nodule radius fitted lung tumour profiles previously reported by Samei et al. [109] very well.

Sun et al. [60] presented a method of simulating three-dimensional lung nodules in CT using several ellipsoids with various axial lengths, all sharing the same centre. The simulated nodules were inserted into clinically acquired CT images using simulation software originally intended for simulating colonic polyps [110]. The nodules were inserted on a voxel-by-voxel basis, comparing each voxel value inside the simulated nodule with the voxel value at the location where the nodule was to be inserted. If the voxel value in the original CT image was similar to the voxel value of the simulated nodule, it was assumed that the nodule voxel lay within surrounding tissue, and the voxel value in the original image was replaced by the voxel value of the simulated nodule. However, if the voxel value in the original image differed from the voxel value of the simulated nodule it was assumed that the voxel was completely or partly located in air. In this case, the nodule voxel value was added to the voxel value in the original image. However, changing the voxel values of the

original image resulted in a reduction of the noise in these voxels. This was compensated for by adding spatially correlated noise to the nodule voxels. The amount of noise added was weighted by the change in each voxel value. No evaluation of the method was reported.

Li et al. [59] presented a method of simulating lung nodules in paediatric multi-detector CT (MDCT). The method was based on the creation of three-dimensional nodules by modelling the nodules as two-dimensional masks on sequential MDCT images. Thus, for each simulated nodule, the peak contrast and radius of the nodule could be varied between different CT slices and could thus be adjusted according to the location of the centre of the nodule relative to the centre of the CT slices. Irregularly shaped simulated nodules were obtained by varying the radius from one polar angle to another. The steepness of the nodule contrast profile was adjusted to obtain a smooth surface around the irregular border of the nodule. The method was validated by conducting an observer performance experiment using 93 image sets. Each image set contained zero or one nodule (either real or simulated) and four experienced paediatric radiologists were given the task of identifying the image sets in which a nodule was present, and then grading their level of confidence that the nodule was real. The detectability of the nodules was evaluated by comparing the percentage detected nodules and the percentage false positive detections of real and simulated nodules. The visual appearance of the nodules was evaluated using ROC analysis combined with a two-sample t-test. The results revealed that a larger number of the real nodules were detected than of the simulated nodules. It was, however, difficult for the observers to visually differentiate simulated nodules from real ones.

6.6 Summary of Paper III

6.6.1 Background

Anatomical images containing simulated pathology have proven to be a valuable tool in studies aiming at evaluating and optimizing radiographic examinations. Using simulated pathology in a detection study provides a unique opportunity to control the variables that are to be studied, e.g. nodule size or density. As described above, a number of methods of creating simulated nodules in both conventional chest radiography and CT have been described. However, none of these methods is appropriate for simulating lung nodules in chest tomosynthesis. The aim of the study presented in Paper III was therefore to develop a method suitable for simulating lung nodules in clinical chest tomosynthesis images.

6.6.2 Description of the method

The method is based on the creation of three-dimensional artificial nodules, which are inserted into each projection image before reconstruction of the tomosynthesis section images. Based on the visual appearance of real nodules and the nodule characteristics described in Section 6.1, three-dimensional nodules, with a resolution (voxel size) of 0.1×0.1×0.1 mm^3, were created beginning with a sphere with the same volume as that desired for the simulated nodule. A random number of smaller spheres were then added to the original sphere in two steps: first to create the shape of the simulated nodule and then to create the required surface structure. Random irregularities in nodule shape and surface structure were obtained by randomly shifting the centre of each additional sphere relative to the centre of the original sphere. After each addition of spheres the resulting nodule was smoothed using a mean filter (2×2×2 mm^2 for the shape and 0.9×0.9×0.9 mm^2 for the surface structure) (see Figure 6.3). After smoothing, the nodule was delineated by implementing a threshold at 50 % of the maximum voxel value. As the addition of spheres to the original sphere results in a nodule with larger volume than desired, the size of the nodule was scaled down to the same volume as the original sphere after each smoothing.

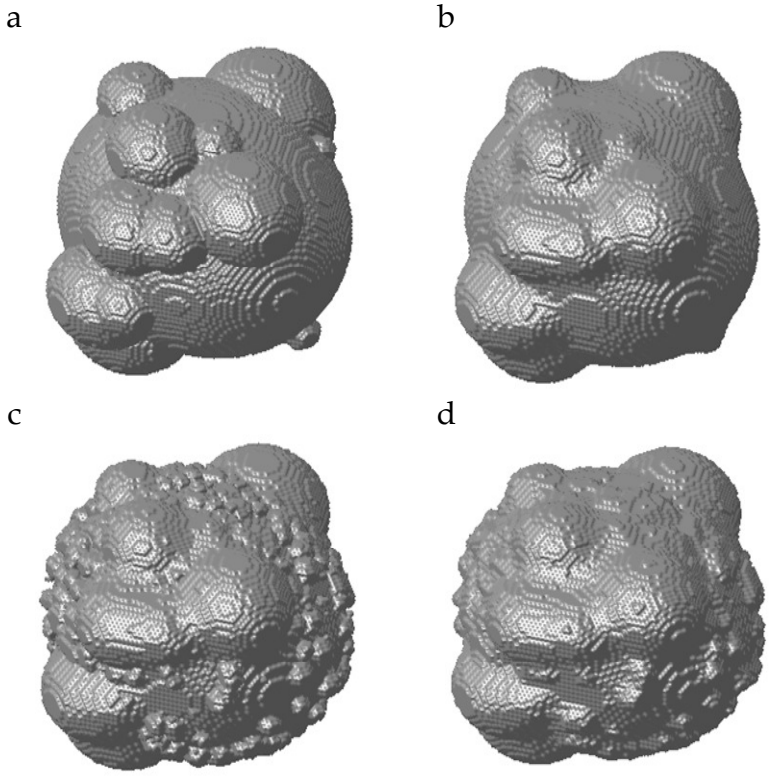

Figure 6.3. Example of the step-by-step creation of an artificial three-dimensional nodule with a radius of 5 mm by adding smaller spheres to the original sphere. (a) shows the nodule before smoothing and (b) after smoothing with a mean filter of size 2×2×2 mm^2. The surface structure is created by adding a large number of even smaller spheres to the created nodule. (c) shows the result before smoothing and (d) after smoothing with a mean filter of size 0.9×0.9×0.9 mm^2.

For a given desired position of the nodule in the patient, information about the geometry of the tomosynthesis projection image acquisition, available in the DICOM (Digital Imaging and Communication in Medicine) header of the projection images, could be used to calculate the corresponding position of the nodule in each projection image. The nodule was inserted into each projection image by simulating the radiation that was emitted from the focal spot, passed through the nodule and reached the detector. By assuming that the nodules had homogeneous density, the path of radiation through the nodule could be neglected and only the distance between the entrance point of the radiation into the nodule and the exit point out of the nodule needed be used to calculate the attenuation of the radiation inside the nodule. However, as the location at which the nodule was to be inserted in reality contained lung tissue, the attenuation coefficient of lung tissue was subtracted in order to reproduce the situation of a real nodule in the lung. Attenuation coefficients of 0.20 cm^{-1} and 0.05 cm^{-1} were used for the nodule and lung tissue, respectively [82]. Hence the resulting attenuation coefficient used in the calculations was 0.15 cm^{-1}.

In order to account for blurring due to the facts that the focal spot is not an actual point source and is moving during the exposures (approx. 0.2 mm/exposure), each focal spot was divided into 5×5 point-like focal spots, called subfocuses. Furthermore, in order to correctly account for aliasing, each pixel in the detector was divided into 5×5 subpixels. Thus, to insert the nodule into each projection image, the radiation was traced from each of the subfocuses to each of the subpixels (see Figure 6.4). The pre-sampling MTF (determined as described in Section 6.3) was then applied to the finely sampled signal. After applying the pre-sampling MTF, sampling in the detector was simulated using the value of the central subpixel in each pixel as the sampled pixel value.

The loss of nodule contrast due to scattered radiation was accounted for by adjusting the signal according to a SPR of 0.5. The overall reduction in detector signal that would have occurred if the nodule had actually been in the patient at the time of the acquisition of the tomosynthesis section images was thus obtained.

Due to the relatively long image acquisition time (approximately ten seconds), some patient motion will be present in the images. This was accounted for by randomly shifting the position of the nodule between insertions into each projection image. The amount of shift relative to the original location was determined according to a normal distribution with a given standard deviation (SD_{motion}), and the direction of the shift was randomized to give uniform distribution over all directions. In general, more patient motion (larger SD_{motion}) was added closer to the heart due to the beating of the heart.

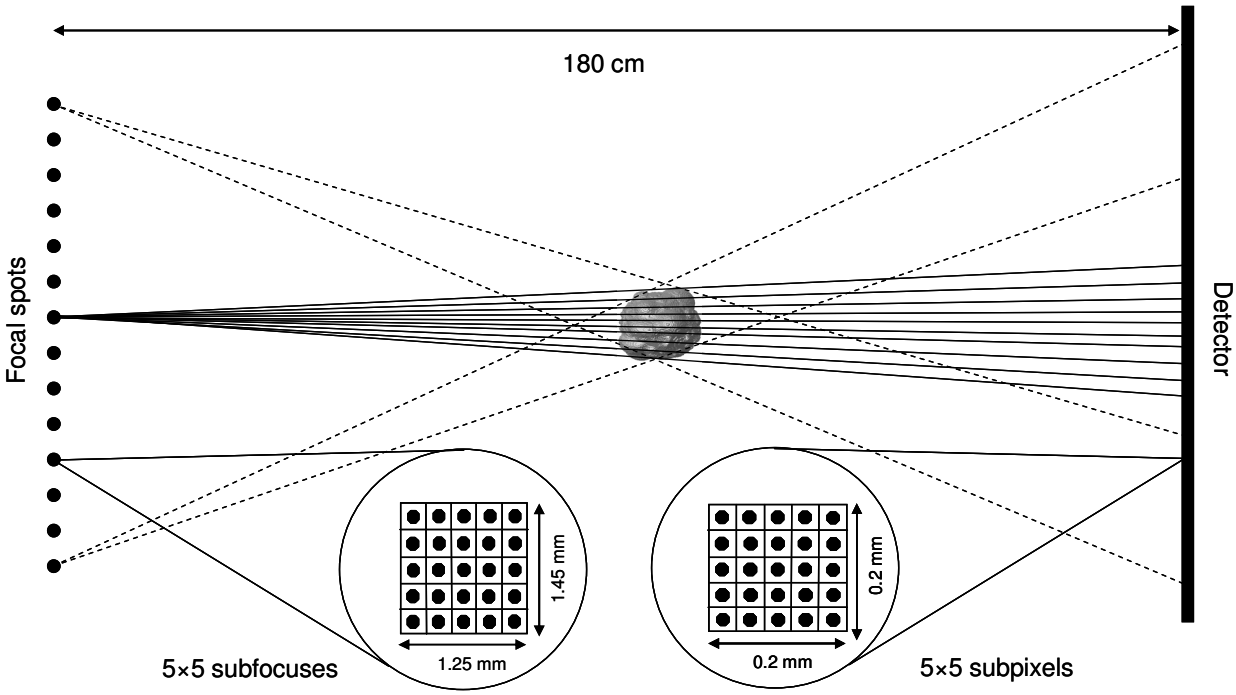

Figure 6.4. Illustration of the tracing of radiation from each of the subfocuses to each of the subpixels for each angular tomosynthesis projection image. (Adapted from Paper III.)

6.6.3 Results

Figure 6.5 shows simulated nodules of different sizes (left-hand column) and real, clinically found nodules (right-hand column). The limited depth resolution of the tomosynthesis section images reduced the necessity to take small anatomical details, e.g. small vessels, into account when positioning the simulated nodule in the parenchyma of the patient, as the signal spread in the depth direction leads to an incorporation of adjacent tissue into a nodule. For example, as can be seen in Figure 6.5, small vessels are visible in both real and simulated nodules. However, it was also found that the simulated nodules in general had a slightly lower contrast than the real nodules. It was concluded that this could be due to the fact that the SPR of 0.5 was slightly too high, especially in the central region of the lung, and it was assumed that adjustment of the SPR would increase the validity of method.

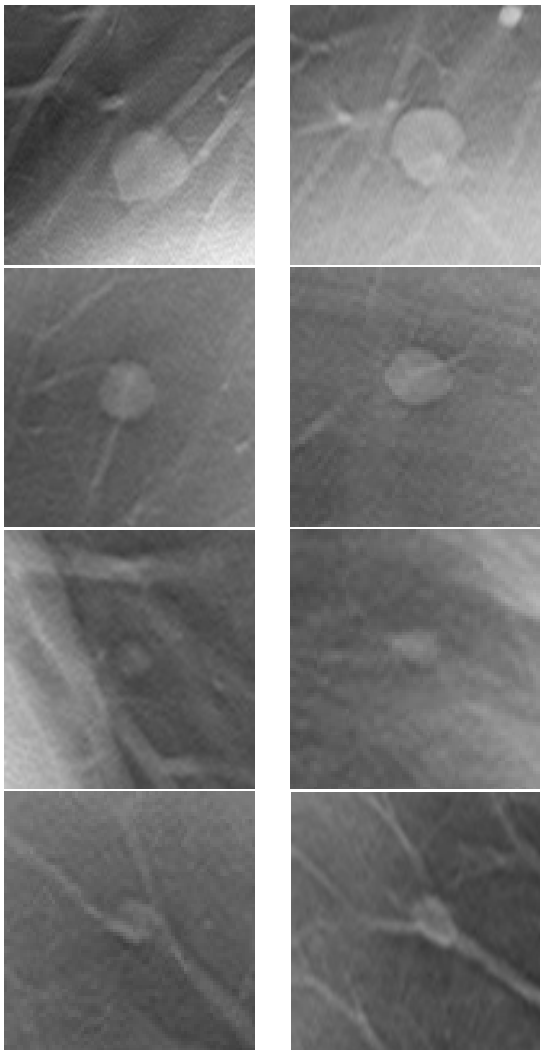

Figure 6.5. Regions of reconstructed tomosynthesis section images with simulated nodules of different sizes inserted into the tomosynthesis projection images of a patient with normal findings (left column), and real nodules with sizes corresponding to those of the simulated nodules found in clinical patients (right column). (Adapted from Paper III.)

The results of projecting the simulated three-dimensional nodule onto the detector are presented in Figure 6.6. As can be seen from the figure, the blurring caused by the signal spread in the detector overshadowed the blurring caused by the finite and moving focal spot. In addition, the results indicate that the MTF can be applied to the signal without using subpixels in the radiation calculation, as no effect of aliasing can be seen in Figure 6.6(d). This provides an opportunity to simplify the simulations and substantially decrease the simulation time.

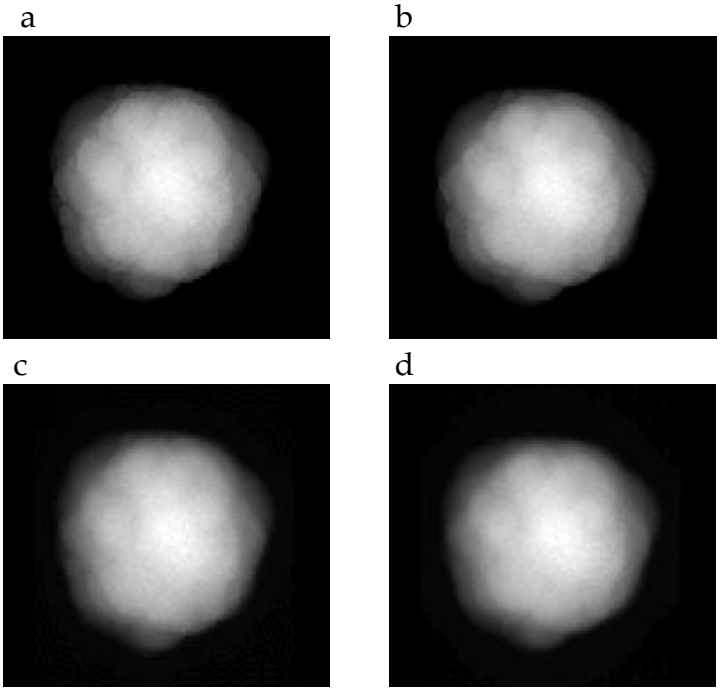

Figure 6.6. The results of projecting a simulated nodule onto the detector: a) using subfocuses and subpixels, b) without subfocuses or subpixels, c) using subfocuses and subpixels after applying the MTF, and d) without using subfocuses or subpixels after applying the MTF. (Adapted from Paper III.)

6.7 Short summary of Paper IV

6.7.1 Background

As it was found that the simulated nodules produced using the method described in Paper III seemed to have a slightly erroneous contrast compared to real, clinically found nodules, a revision of the method was determined necessary in order to give more clinically valid results. Furthermore, a thorough evaluation of the method was needed. The aims of the study presented in Paper IV were therefore to improve the method of simulating lung nodules and to evaluate the improved method by comparing the sensitivity and visual appearance of the simulated nodules with those of real, clinically found lung nodules.

6.7.2 Improvements of the method

The contrast of the simulated nodules depends on the attenuation coefficients and the amount of scattered radiation. Hence, both these factors were further analysed.

Attenuation coefficients

Constant attenuation coefficients of 0.20 cm^{-1} and 0.05 cm^{-1} had been used for the nodule and lung tissue, respectively, in the previous study (Paper III). The attenuation coefficient for lung tissue given in the literature was that of "average" lung tissue [82]. Assuming linearity between CT number and density, and an attenuation coefficient of 0.1928 cm^{-1} for water, which corresponds to a CT number of zero (mean photon energy 70 keV) [111], an attenuation coefficient of 0.05 cm^{-1} was calculated to correspond to a CT number of -750 HU. A CT number of approximately -750 HU was also obtained when measuring the average CT number in the lung region of a patient including many of the larger blood vessels and bronchi. However, as no nodules are located in the location of a bronchus or a vessel, an attenuation coefficient of 0.05 cm^{-1} was assumed to be slightly too high. The attenuation coefficient for lung tissue was therefore instead determined by performing manual measurements of the CT number in the lung regions of real patients. The ROIs used for these measurements were placed in the lung, avoiding areas where bronchi and larger blood vessels were present. The mean CT number obtained from these measurements was -850 HU, which corresponds to an attenuation coefficient of 0.03 cm^{-1}. Therefore, an attenuation coefficient of 0.03 cm^{-1} was used instead of 0.05 cm^{-1} for the subtraction of lung tissue in the calculations of the resulting attenuation coefficient for the simulated nodules. For the validation of the nodule simulation method, the attenuation coefficients of the simulated nodules was varied according to the mean CT number in real, clinically found nodules, as further described in Section 6.7.3.

Scattered radiation

As mentioned in Section 6.2, scattered radiation results in a degradation of image contrast, and several studies have shown that the amount of scattered radiation varies between different regions of a chest image; being higher in regions close to anatomy of higher density [94-97, 112]. This variation should thus be taken into account in the simulation process in order to obtain more realistic contrast for the simulated nodules. Monte Carlo simulations of a tomosynthesis examination performed using the GE Definium 8000 system with VolumeRAD option [99] was used to obtain knowledge on the variation in scattered radiation, both between different areas of the lung and between different tomosynthesis projection images. The Monte Carlo simulations were performed using a voxel phantom, created using CT images of the anthropomorphic chest phantom (PBU-X-21). The size of this phantom corresponds to the size of a 160 cm tall, lean Asian male. This phantom is thus much smaller than the average patient defined by the ICRP (male 176 cm and 73 kg, female 163 cm and 60 kg) [68]. Therefore, using the SPR obtained from the Monte Carlo simulations by Ullman et al. would probably lead to an underestimation of the SF values in larger, Western patients. However, by scaling the SF values reported by Ullman et al. according to the values reported by Jordan et al. [96] for different

patient sizes (see Section 6.2), more realistic SF values for patients of different sizes can be obtained and the variation in SF between different regions of the lung and between different tomosynthesis projection images can be accounted for.

6.7.3 Evaluation of the method

The resulting method was evaluated using clinical images from patients with both normal (n=26) and abnormal findings (n=38) in regard to pulmonary nodules. The total number of lung nodules found was 129. The sizes of the real nodules were determined by manual measurements in three orthogonal planes (transverse plane, sagittal plane and coronal plane) of the CT images of the patients. The volume of each real nodule was then estimated as the volume of an ellipsoid, with axes lengths equal to the manual measurements of the nodule diameter in each orthogonal plane. The diameters presented in Figure 6.7 are the diameters of spheres with the same volume as the corresponding ellipsoids.

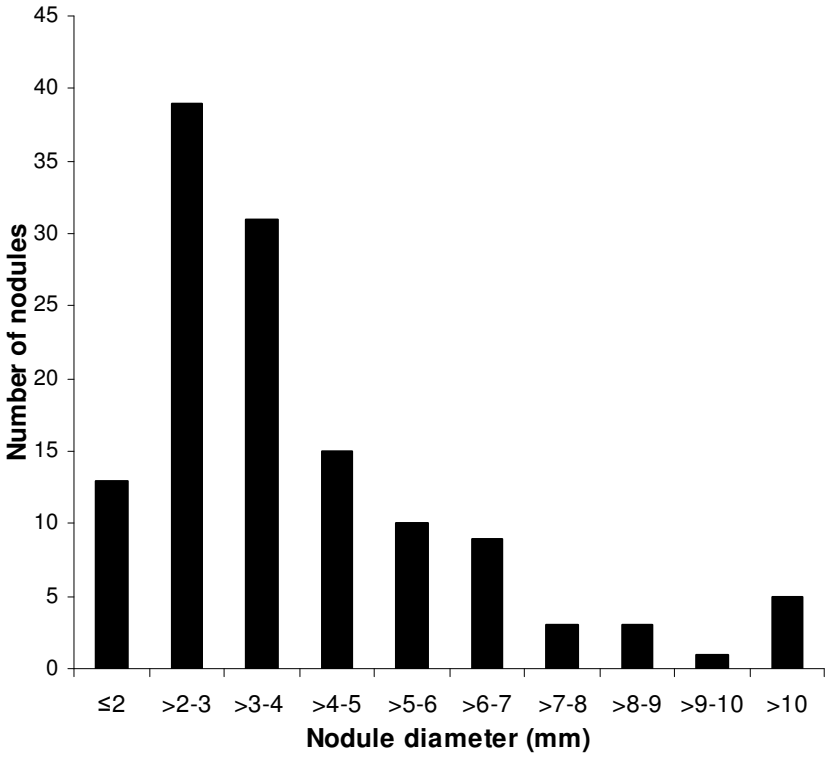

Figure 6.7. The size distribution of real nodules found in the patient images. The nodule diameters shown are the diameters of spheres with the same volume as the corresponding ellipsoids. (From Paper IV.)

The density of each real nodule was estimated by determining the CT number in a ROI placed over the area of the nodule in each of the adjacent thin CT slices where the nodule could be identified. The CT number of each nodule was determined as the mean of the CT numbers from all slices. The corresponding attenuation coefficients

of the nodules were then determined using the linearity between CT number and density, in the same way as described for the lung tissue above. Figure 6.8 shows the distribution of the CT number and corresponding attenuation coefficient of the real nodules.

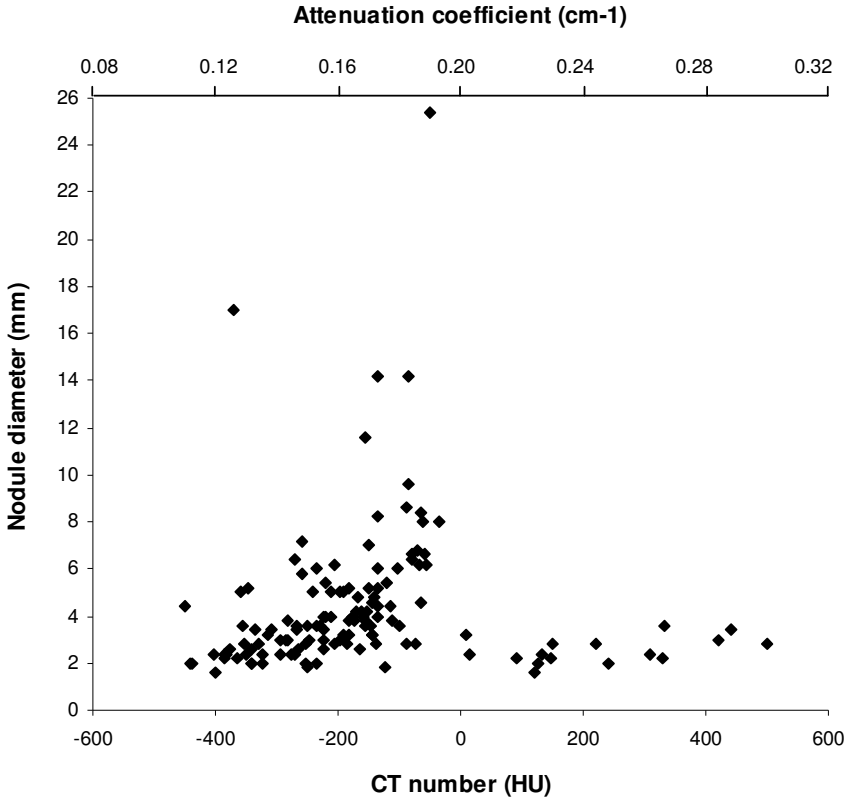

Figure 6.8. The distribution of CT number and corresponding attenuation coefficient for the real nodules found in the patient images. Each data point represents one nodule. (From Paper IV.)

Simulated nodules, matching the real, clinically found nodules in size, density and location, were created and randomly inserted into the patient images after dividing the patient material into three equally sized groups: patients with only real nodules (n=19), patients with only simulated nodules (n=19) and patients with both real and simulated nodules (n=19). The rest of the patients (n=7) were used as normal (nodule-free) cases in the study. After determining the location of the simulated nodule in the patient, the corresponding location in the Monte-Carlo-simulated tomosynthesis projection images of the voxel phantom was identified. This allowed the most appropriate SPR for use in the insertion of the nodule into each projection image to be obtained. The insertion process was performed in the same way as described in Paper III, without the use of subfocuses or subpixels in the tracing of the radiation. Examples of three real nodules (left) together with the corresponding simulated nodules (right) are shown in Figure 6.9.

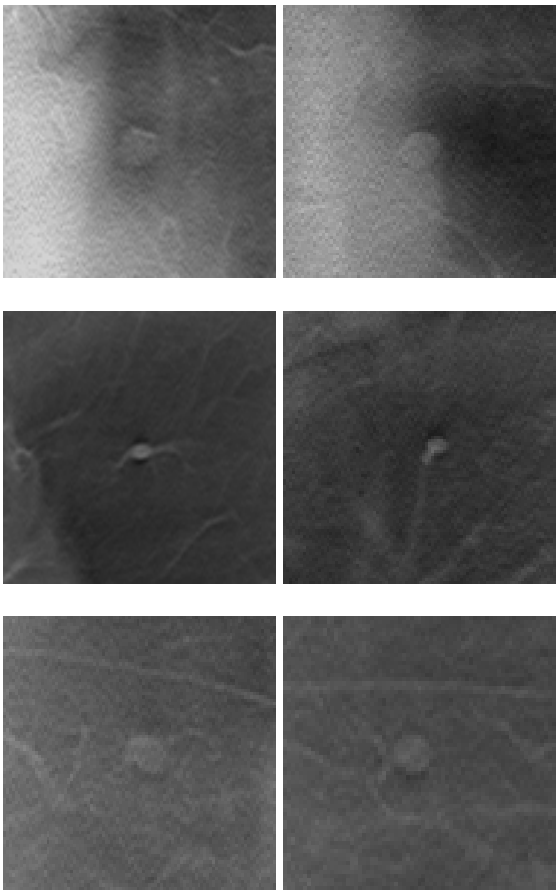

Figure 6.9. Examples of real nodules (left column) and the corresponding simulated nodules (right column), matched according to size, density and location, but inserted into images from different patients (thus not matched for patient motion or scattered radiation). (From Paper IV.)

An observer performance study was conducted in which three thoracic radiologists and one radiology resident participated as observers. The images were evaluated using the in-house developed software ViewDEX [113, 114], which is designed especially for observer performance and visual grading studies using clinical images. Using this software, the images could be shown to the observer in a unique random order for each observer. The study consisted of two parts. The first part was a detection study, with the main purpose of comparing the detection of real and simulated nodules. Thus, the observers were given the task of detecting and marking nodules in the images, according to the FROC paradigm [107]. For each mark the observers were asked to rate: 1) their confidence in the marking being a nodule (four-level rating scale, 1 = lowest confidence, 4 = highest confidence), and 2) their confidence in the nodule being real and not simulated (five-level rating scale, 1 = "definitely simulated" and 5 = "definitely real"). In the second part of the study, the location of all nodules were revealed to the observers, and the observers were asked to rate their confidence of each nodule being real (five-level rating scale).

As the purpose of first part of the study was to compare the detection of real and simulated nodules, an AFROC curve for each group of nodules would have been desirable. However, as it is not known whether a false positive mark is related to the group of real nodules or simulated nodules, correct AFROC curves could not be plotted. Instead, a modified version of ROC analysis was used to analyse the data. In the present work the TPF was represented by the detection of real nodules, while the FPF was represented by the detection of simulated nodules. The TPF was then plotted against the FPF for each of the three decision thresholds resulting from the four-level rating scale and the ROC software ROCKIT (C. Metz, University of Chicago) was used to fit a curve to the data. Using this modified ROC approach, a value of A_z equal to 0.5 corresponds to identical detectability of real and simulated nodules. A value of A_z greater than 0.5 indicates higher sensitivity for real nodules, whereas a value lower than 0.5 indicates a higher sensitivity for simulated nodules.

The visual appearance of the nodules was evaluated both qualitatively (comparison of histogram plots of the rating distributions for real and simulated nodules) and quantitatively using the modified ROC analysis described above (TPF corresponded to the ratings of real nodules and FPF corresponded to the ratings of simulated nodules).

6.7.4 Results

The first part of the observer performance study revealed that the percentage detected real and simulated nodules was 24.2 % and 29.3 %, respectively, including all ratings for nodule confidence (ratings 1-4). The ROC curve comparing the sensitivity of real and simulated nodules is shown in Figure 6.10 for each observer. The A_z value was close to 0.5 for all observers, indicating similar sensitivity for real and simulated nodules.

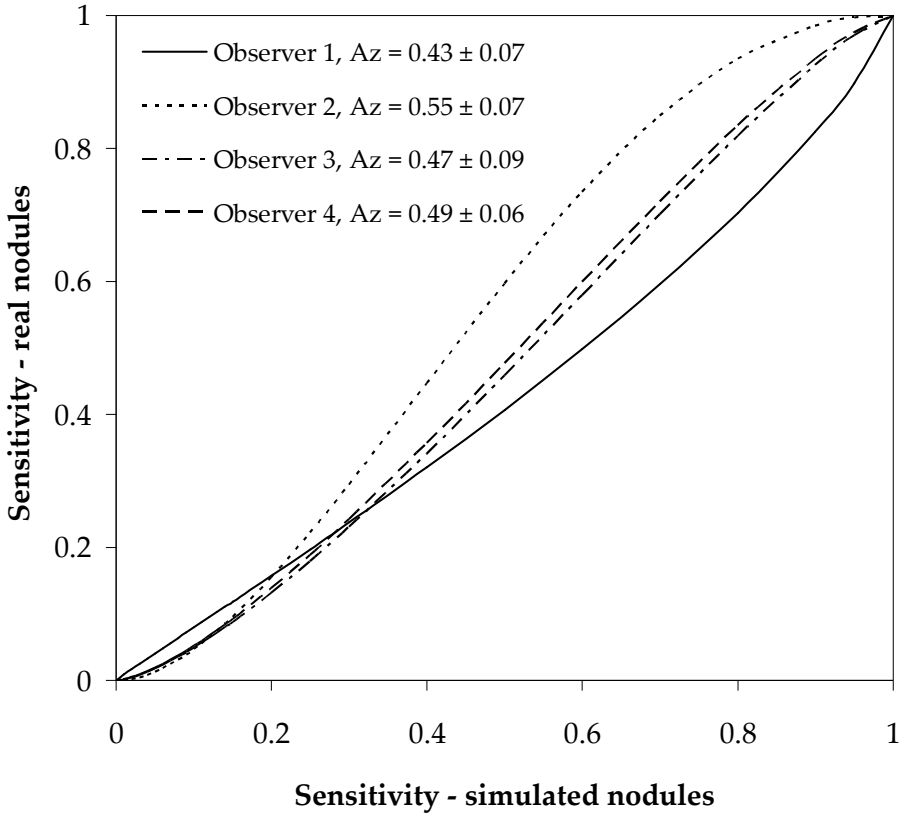

Figure 6.10. Results from the ROC analysis of the sensitivity of real and simulated nodules. The A_z and its standard deviation are given for each observer. An A_z of 0.5 corresponds to identical sensitivity for real and simulated nodules. (From Paper IV.)

The qualitative analysis of the rating distributions indicated similar visual appearance of real and simulated nodules, as there was considerable overlap between the two distributions, see Figure 6.11. However, as can be seen from Table 6.1, the modified ROC analysis indicated a difference between the rating distributions, as the A_z values for the observers ranged between 0.70 and 0.74, meaning that the real nodules in general obtained a slightly higher rating than the simulated nodules.

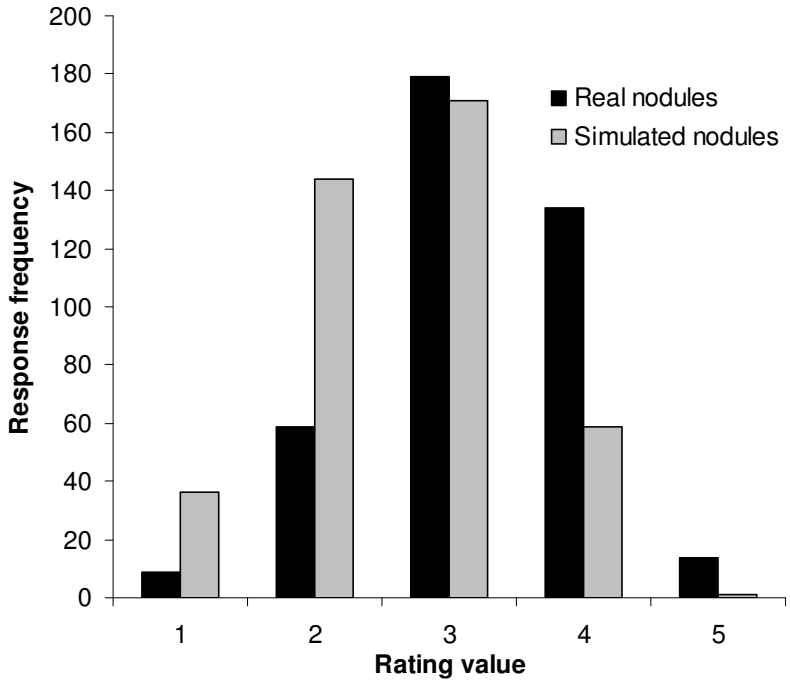

Figure 6.11. The rating distributions for real and simulated nodules, pooled for all observers. Rating 1 corresponds to "definitely simulated" while rating 5 corresponds to "definitely real". (From Paper IV.)

Table 6.1. The A_z value (and corresponding standard error) resulting from the ROC analysis of the visual appearances of real and simulated nodules, shown for each observer. The A_z values ranged between 0.70 and 0.74. (Adapted from Paper IV.)

	A_z
Observer 1	0.73 ± 0.05
Observer 2	0.74 ± 0.04
Observer 3	0.70 ± 0.04
Observer 4	0.72 ± 0.04

Think it over, think it under."

-A.A. Milne

7 Discussion and future work

In the present thesis, methods for evaluation and optimization of chest tomosynthesis have been presented. The work included the development of a method for simplified estimations of effective dose from chest tomosynthesis examinations and the development of methods for creation of hybrid images, which can be used to evaluate chest tomosynthesis with regard to nodule detection and to optimize the exposure from a chest tomosynthesis examination. In Sections 7.1-7.3 some aspects of the method developments will be discussed, while an overall discussion of the work will be given in Section 7.4. Possible future work regarding the evaluation and optimization of chest tomosynthesis will finally be discussed in Section 7.5.

7.1 Dosimetry

In this work a simplified method for estimation of the effective dose from a chest tomosynthesis examination was developed. By using the PCXMC 2.0 software [71], the resulting effective dose from chest tomosynthesis examinations, performed using different tomosynthesis system configurations, were determined for various patient sizes. Conversion factors between KAP and effective dose were then calculated for each system configuration and patient size. Using these conversion factors the effective dose resulting from tomosynthesis examinations can be estimated only by multiplying the total KAP of the examinations with the presented conversion factors.

The organ doses were in PCXMC 2.0 [71] calculated using computational hermaphrodite phantoms representing patients of different sizes. As mentioned earlier the phantoms are slightly modified versions of the phantoms presented by Christy and Eckerman [72] in 1987. The phantoms are thus computational phantoms in which both the body and organ contours are described by mathematical expressions. It can be argued that the main source of error in Monte Carlo simulations of absorbed dose distributions in the human body from external radiation is the phantom used to represent the patient. Mathematical phantoms can be expected to be less accurate than, for example, voxel phantoms, which are usually constructed based on CT examinations of real human beings. Tapiovaara et al. [71] compared the resulting effective doses obtained from dose calculations using PCXMC 2.0 software to the effective doses obtained from Monte Carlo calculations using the reference male and female phantoms Rex and Regina performed by Schlattl et al. [115]. In the comparison, the dose calculations in PCXMC were performed using phantom heights and weights corresponding to those of Rex and Regina. The results showed that the differences between the effective doses calculated using PCXMC and those by Schlattl et al. were about 20 %. Due to this potential error in the

estimated effective dose using the PCXMC software, the purpose of presenting the small differences in E_{KAP} values between various system configurations and patient sizes may seem rather ambiguous. However, as the comparisons between the E_{KAP} values presented in Paper I are relative, these small differences might still be of interest.

The results presented in Paper I show that the estimation of the effective dose from a tomosynthesis examination can be simplified by assuming that all the radiation is delivered to the patient in the zero-degree projection (corresponding to a conventional PA projection in chest radiography). For all tomosynthesis system configurations and patient sizes considered in Paper I, the error introduced by not taking the dose contributions from each individual projection image into account in the effective dose estimation was less than 10 %. This error increases as the angular interval used for the acquisition of the projection images increases. For the angular intervals used in the commercially available tomosynthesis systems (GE Definium 8000 system with VolumeRAD option ±15°; Shimadzu SonialVision Safire system ±20°), the error is less than 5 %. As the results presented in Paper I are based on relative comparisons of effective doses, they should not be seriously affected by the fact that the phantom used in the calculations differs from the reference phantoms established by the ICRP.

The E_{KAP} values for the zero-degree projection presented in Paper I differs slightly from the E_{KAP} values for the PA projection presented by the NRPB [48]. The E_{KAP} for various common radiographic examinations established by the NRPB are based on Monte Carlo calculations of organ doses using a geometric hermaphrodite phantom described by Cristy [74]. The phantom used by the NRPB is thus the older version of the phantom used in a slightly modified version in PCXMC 2.0. Tapiovaara et al. [71] have, however, shown that the organ doses obtained from calculations using PCXMC 2.0 agrees well with the organ doses obtained in the dose calculations presented by the NRPB. In the present work (Paper I) the E_{KAP} varied between 0.207 (170 cm and 100 kg) and 0.372 (170 cm, 50 kg) for the PA projection acquired at 120 kV using a total filtration of 3 mm Al + 0.1 mm Cu. According to simulations using the SRS-78 Spectrum Processor software [116], the half-value layer (HVL) of this radiation quality is similar to that obtained for a radiation quality of 120 kV and a total filtration of 6.5 mm Al. The total filtration used to calculate E_{KAP} for a PA projection acquired at 120 kV by the NRPB varied between 2 mm Al and 5 mm Al. The E_{KAP} presented by NRPB increases with increasing amount of total filtration. For example, the E_{KAP} calculated using a total filtration of 5 mm Al (0.231 mSv/Gycm^2) is approximately 13 % higher than the E_{KAP} calculated using a total filtration of 3 mm Al (0.200 mSv/Gycm^2). By extrapolating the results presented by the NRPB, the E_{KAP} for a total filtration of 6.5 mm Al can be estimated to be approximately 0.246

mSv/Gycm^2. The E_{KAP} for a patient with a height of 170 cm and a weight of 70 kg, using a tube voltage of 120 kV and a total filtration of 3 mm Al + 0.1 mm Cu reported in Paper I was 0.285 mSv/Gycm^2.

The difference between the E_{KAP} reported in Paper I and that reported by the NRPB [48] may partly be due to differences between the phantoms used for the calculations. The phantom used for the dose calculations in PCXMC 2.0 is a slightly modified version of the phantom used in the dose calculations presented by the NRPB. However, the main explanation of the difference is probably the fact that the E_{KAP} reported in NRPB are based on the tissue weighting factors given in ICRP Publication 60 [65], while the E_{KAP} presented in Paper I are based on the tissue weighting factors of ICRP Publication 103 [15]. For comparison, Båth et al. [33] performed calculations of the effective dose to 40 patients who had undergone both chest radiography and chest tomosynthesis examinations using the GE VolumeRAD system. The mean heights and weights of the patients were 170.9 cm and 70.2 kg, respectively. The E_{KAP} for the chest radiography examination (PA projection image + LAT projection image) was by Båth et al. determined to be 0.23 mSv/Gycm^2 using the tissue weighting factors in ICRP Publication 60 and 0.27 mSv/Gycm^2 using the tissue weighting factors in ICRP 103. It must, however, be noted that Båth et al. also assumed a total filtration of 3 mm Al + 0.1 mm Cu in their calculations, and thus the E_{KAP} would be expected to be slightly higher than the established value of 0.18 mSv/Gycm^2 [75] in use today.

Due to the large variation in E_{KAP} with patient size found in the present work, the purpose of effective dose estimations needs to be addressed. There has been some debate on the validity of using effective dose as a measure of dose in medical procedures. Borrás and Huda give their opinions on the subject in a recent point-counterpoint debate article [117]. Borrás argues that the use of effective dose for individuals undergoing medical exposure is inappropriate, as the weighting factors in ICRP are determined for a reference person of a certain size and age, and will therefore not provide a correct risk estimate for individuals. Huda, on the other hand, argues that effective dose is the most appropriate measure to use for quantifying the amount of radiation delivered to the patient. According to Huda, using the effective dose to quantify the radiation dose enables comparisons of the effective dose to a patient from a diagnostic X-ray examination with the effective doses from natural background radiation, and thus puts medical exposure into an appropriate perspective. The ICRP states that the effective dose is intended for use as a radiation protection quantity on the basis of established reference values [15]. It is therefore not recommended to use effective dose for detailed individual investigations of exposure and risks. However, in ICRP Publication 105 [118] it is stated that: *"Effective dose can be of practical value for comparing the relative doses related to stochastic effects from: different diagnostic examinations and interventional procedures, the*

use of similar technologies and procedures in different hospitals and countries, and the use of different technologies for the same medical examination, provided that the representative patients or patient populations for which the effective doses are derived are similar with regard to age and sex". Hence, effective dose may be valuable in the clinical situation for comparing exposure from different kinds of radiological examinations, or for comparing the patient exposure from a specific system to the established diagnostic reference levels for a particular type of examination. It can be argued that, for as long as the effective dose is not used to estimate the risk factors associated with exposure, but only to quantify the amount of radiation delivered to the patient, the use of effective dose might be valid.

As mentioned before, the high level of uncertainty connected to the determination of the effective dose and the high precision of the conversion factors presented in Paper I may be seem somewhat contradictory. However, the high precision was chosen in order to demonstrate the small difference between the E_{KAP} for the zero-degree projection and the E_{KAP} for the entire tomosynthesis examination and to be able to determine correct E_{KAP} values for each tomosynthesis system configuration. Due to the small percentage differences in E_{KAP} values between different system configurations, no effect would be visible if the E_{KAP} value for the zero-degree projection was presented with lower precision.

Finally, it should be noted that the E_{KAP} calculated for the larger patients should probably be lower in reality. The reason for this is the scaling of the phantom in PCXMC when simulating larger patients. As described in Section 4.3.1, when modifying the size of the phantom in PCXMC, all the organs and tissues are scaled according to the increase in patient size. In reality, larger patients are more likely to have a larger proportion of fat, while their organs are probably not very different in size from those in an average sized patient. For such body composition the fat might shield the more radiation sensitive organs and tissues, which would result in a reduction of the absorbed dose to these organs and tissues and, hence, a lower effective dose to the patient.

7.2 Simulated dose reduction

The method of simulating dose reduction described in Paper II is based on the creation of a noise image, which is added to the original image in order to simulate acquisition of the image at a lower dose level. In order to obtain a dose-reduced image with the same noise properties as an image actually acquired at a lower dose level, flat-field images acquired at different dose levels are used to obtain information about the NPS at different dose levels. In addition, the flat-field images are used to obtain the relationship between the standard deviation of pixel values and detector dose. This relationship is then used to correct the pixel values of the

created noise image according to the dose variations that exists over the clinical image that is to be dose reduced.

Optimally, the flat-field images used in the dose reduction process should be acquired as close to the original and simulated dose levels as possible. As described in Paper II, if the NPS at the exact dose level is not known, interpolation (or extrapolation if the dose levels are higher or lower than the dose level of any of the flat-field images) of the NPS between two other dose levels is used. Thereby only the magnitude of the NPS will be determined correctly, while the shape of the NPS at the desired dose level may be slightly erroneous. One way to minimize the potential error in the shape of the NPS is, therefore, to acquire flat-field images at many, closely spaced dose levels so that the difference between any two dose levels used for interpolation is small. In order to estimate the number of flat-field images required to obtain a reasonably valid simulation of dose reduction, it is necessary to have some idea of the magnitude of error that is introduced if the difference in dose levels between the flat-field images and the original and simulated dose levels, respectively, is increased. A hint is given by the validation of the dose simulation method described in Paper II, where an aluminium phantom with homogeneous regions of different amounts of aluminium (0, 8 and 18 mm) was used. The mean pixel value in the medium-dose region (8 mm Al) of the original image was determined to be 49.3, which corresponded to an entrance air kerma at the detector of 0.25 μGy. The mean pixel value in the same region of the image actually acquired at the simulated dose level was 8.4, corresponding to an entrance air kerma of 0.042 μGy (17 % of the original dose level). The two flat-field images used to determine the NPS at the two dose levels were acquired at dose levels of 0.20 μGy and 0.034 μGy. Hence, the flat-field images used to determine the NPS at the original and simulated dose levels were both acquired at slightly lower dose levels. As a result of this, the slopes of the NPS at both the original and simulated dose levels were slightly underestimated. However, as the NPS of the noise image was obtained from the difference in NPS between the original and simulated dose levels, the two underestimations cancelled each other to some extent, and the simulated image had only a small error in slope compared to the image actually acquired at the lower dose level, as can be seen in Figure 5.2 in Section 5.4.3. As the flat-field images used for the NPS determinations were acquired at slightly lower dose levels than the dose levels in the medium-dose regions (8 mm Al regions) of the original image and simulated image, the error in the slope of the NPS in the simulated image was larger in the high-dose region of the image and smaller in the low-dose region of the image. However, although the flat-field images were acquired at dose levels approximately 20 % below the medium-dose regions of the images, the resulting error in the slope of the NPS in the simulated image was relatively small.

When simulating a dose reduction in a non-homogeneous image, e.g. a clinical image, the pixel values of the created noise image must be adjusted according to the

variation in detector dose that exist in the clinical image that is to be dose reduced. As described above, this is accomplished using the relationship between the standard deviation of pixel values and the detector dose established using the flat-field images. Also for this adjustment, a more correct result is thus obtained if the flat-field images are acquired at many, closely spaced dose levels. However, as can be seen in Figure 5.1 in Section 5.4.3, the relationship between pixel mean and pixel variance is constant at higher dose levels for the GE Definium 8000 system with VolumeRAD option. Hence, in this dose region the need for closely spaced flat-field images is less than in the dose region where the relationship is affected by the detector dose, and thus a compromise can be made between benefit and work load by acquiring more flat-field images in the dose region where greater variation is seen.

As can be seen in Figure 5.2, the noise characteristics in the different dose regions of the simulated image of the aluminium phantom, produced using the method described by Båth et al. [51], has both an erroneous magnitude and slope. As the method of Båth et al. is based on the assumption of a constant DQE between: 1) the original dose level and the dose level of the flat-field image that is closest to the original dose level, 2) the simulated dose level and the dose level of the flat-field image that is closest to the simulated dose level, and 3) the dose variations that may occur over a clinical image, the magnitude of the noise in a simulated image may not be correct. As can be seen in Figure 5.2, the method of Båth et al. in this case overestimates the amount of noise in the simulated image. This is due to the fact that the flat-field images used in the simulated dose reduction are acquired at dose levels lower than both the original dose level and the simulated dose level. Thus, the method of Båth et al. overestimates the noise at both the original dose level (because the increase in DQE between the dose level of the high-dose flat-field image and the original dose level is not taken into account) and at the simulated dose level (because the increase in DQE between the dose level of the low-dose flat-field image and the simulated dose level is not taken into account). As the NPS of the noise image is given by the difference in NPS between the original dose level and the simulated dose level, one may expect that the two overestimations would cancel each other out, and not affect the magnitude of noise in the dose-reduced image. However, as seen in Figure 5.1, the overestimation is greater at lower dose levels (as DQE changes more rapidly with dose). Therefore, in this case the overall amount of noise that should be added to the original image in order to simulate a dose reduction will be overestimated using the method of Båth et al.

The difference in NNPS between the reconstructed tomosynthesis section images obtained using the dose simulation method described in Paper II and the method described by Båth et al. [51], is shown in Figure 5.4. As can be seen in Figure 5.3, this difference in NNPS is barely visible in the reconstructed tomosynthesis section images. It can thus be argued that the benefits of using a method that takes the variation in DQE into account are small. However, even if the difference is small in

an image, it may introduce a bias, for example, in a detection study. Furthermore, as both the method described in Paper II and the method described by Båth et al. are based on the acquisition of flat-field images, the difference in work load between the two methods is minor. The method accounting for variation in DQE only requires a small extra effort to establish the relationship between the variance of pixel values and detector dose. This extra effort is easy to motivate in the low-dose region in order to obtain a realistic result of the simulated dose reduction.

The method of simulating dose reduction in this work (Paper II) was validated by comparing the noise properties in images simulated to be acquired at a lower dose level with those in images actually acquired at the lower dose level. Both homogeneous images and clinical images were used for the validation, and the method was validated for different amounts of simulated dose reduction. The results revealed good agreement between the noise properties of the simulated images and the actually acquired low-dose images, which indicates that the method has a high degree of validity. In order to further validate the method an observer performance study could be performed in which the observer performance using simulated low-dose images is compared to the observer performance using images actually collected at a lower dose level. However, as the validation of the method, described in Paper II, did not reveal any significant differences in noise properties between simulated low-dose images and images actually acquired at the lower dose level, it can be expected that an observer performance study will probably not reveal any difference in performance between the two types of images.

Båth et al. [33] performed calculations of the effective dose to 40 patients who had undergone tomosynthesis examinations using the GE tomosynthesis system. The mean height and weight of the patients was 170.9 cm and 70.2 kg, respectively. When examining the exposure data used for the tomosynthesis examinations, it was found that the tube load used for the acquisition of scout images was <1.5 mAs for 31 of the 40 patients included in the study. Hence, the tube load that should be used for the acquisition of each tomosynthesis projection image should be less than 0.25 mAs [(1.5 mAs×10)/60]. However, as the lowest possible Renard step is 0.25 mAs for the GE tomosynthesis system it was this, rather than the actual dose ratio, that determined the resulting exposure of these patients. Therefore, an actual dose reduction in the tomosynthesis examination using this system is today only possible by either changing the number of projection images used, or using extra filtering during the acquisition of the tomosynthesis projection images. If future evaluations of chest tomosynthesis should reveal that it is possible to reduce the exposure in an examination without loosing diagnostic accuracy, manufacturers may perhaps be motivated to find a solution for the limitation in lowest exposure possible for the X-ray tube to deliver. Furthermore, it would perhaps also be motivated to find a solution to the problem of a reduction in DQE at lower dose levels if it is shown that such low doses are clinically possible to use.

7.3 Nodule simulation

In this work, a method of simulating lung nodules in chest tomosynthesis was developed and evaluated. The method is based on the creation of three-dimensional artificial nodules that are inserted into the tomosynthesis projection images before reconstruction of the section images. In order to mimic reality, the signal spread in the detector, the scattered radiation and the patient motion were accounted for in the simulation process. In this way, the pixel values at the location where the simulated image was inserted could be changed according to the reduction in pixel value that would have occurred if the nodule had actually been present in the patient at the time of the acquisition of the tomosynthesis projection images.

The developed method was evaluated by comparing the sensitivity and visual appearance of the simulated nodules to those of real nodules (Paper IV). Hence, nodules were simulated with the same size and density as real nodules found in patient images. The size of the real nodule was determined by manual measurements of nodule diameter in three orthogonal planes in CT images. The volume of each real nodule was thus estimated as the volume of an ellipsoid with radii equal to the manually measured nodule diameter in each of the orthogonal directions. However, even though not used, the diameters of the real nodules were also determined by automatic segmentation using the commercially available CAD software Lung Volume Computed Assisted Reading (LungVCAR; GE Healthcare, Milwaukee, WI, USA). The software delineates the nodule border and provides information about the nodule diameter in three orthogonal directions, and nodule volume. However, in the present work, the manual measurements were determined to give a more accurate result, as visual evaluation of the nodule delineation revealed that other tissues were often included in the segmented nodule volume. Hence, using the nodule sizes given by the LungVCAR software would, in many cases, lead to overestimation of nodule size. It was also found in the literature that CAD software has been shown to overestimate nodule volume, especially for nodules attached to vessels or pleura [119, 120]. In addition, during the segmentation process of the real nodules it was also found that many of the nodules could not be segmented using the LungVCAR software, why the use of this method for estimating the sizes of the real nodules was determined to be inappropriate.

In order to verify that the use of manual measurements in the determination of the diameter of the real nodules did not introduce any differences between the sizes of the real and simulated nodules in the reconstructed tomosynthesis section images, the largest diameter of all visible nodules was manually measured in the tomosynthesis section images. The results of these measurements did not indicate any bias in size between the real and simulated nodules, although small differences were found in the largest diameter between each pair of real and simulated nodules. However, as the mean of the difference between real and simulated nodules were close to zero, this difference is probably due to the fact that only the volumes of the

real and simulated nodules were matched. Hence, the largest diameter of the real and simulated nodules in the tomosynthesis section images differed slightly, as the shapes of the real nodules and corresponding simulated nodules differed.

The density of the real nodules found in the patient material was estimated by the CT number in ROIs placed over the area of each nodule in adjacent CT slices in which the nodule was visible (Paper IV). Assuming linearity between CT number and nodule density and an attenuation coefficient of 0.1928 mm^{-1} for water, corresponding to a CT number of zero (mean photon energy 70 keV) [111], the mean CT number of each nodule was converted into a corresponding attenuation coefficient. The measured CT number of a non-homogeneous nodule was consequently the mean value of the different CT numbers in the nodule. Due to the irregular shape and non-homogeneity of some of the real nodules, there is of course some uncertainty associated with the determination of nodule density. However, the results from the observer performance study showed no significant difference between the detectability of real and simulated nodules. This indicates that, on average, the density of the simulated nodules matches the densities of the real nodules.

As described in Paper III, it was noted that the contrast of the simulated nodules was slightly lower than the contrast of real nodules in the first implementation of the method. This could of course be due to the fact that the density of the simulated nodules (a constant nodule attenuation coefficient of 0.20 cm^{-1} [82] was used for all simulated nodules) was slightly lower than the density of the real nodules used for comparison. However, the amount of scattered radiation that is added in the nodule simulation process will also affect the contrast of the simulated nodules. A constant SPR of 0.5 (corresponding to a SF of 0.33) was assumed for the entire lung region (Paper III). This value was reported to be the mean SPR in the lung region by Ullman et al. [97], who performed Monte Carlo simulations of a digital chest radiographic system using a chest voxel phantom. However, both the results reported by Ullman et al. and in other studies [94, 96] indicate that the SF varies over the lung region and is higher in areas of higher density. It may thus be argued that these variations in SF should be taken into account in order to mimic the reality in the nodule simulation process, as was done in the improved method (Paper IV).

In the evaluation of the nodule simulation method (Paper IV), SPRs obtained from Monte Carlo simulations of the tomosynthesis system [99] were used. As described in Section 6.2, these Monte Carlo simulations were performed using a voxel phantom with a size corresponding to a 160 cm tall, lean Asian male. Jordan et al. [96] showed that the SF is highly dependent on patient size; the SF value in the lung region was shown to vary between 0.19 and 0.36 for patients with posterioanterior diameters (PA diameters) ranging from 26 cm to 34 cm. This variation in SF corresponds to a 20 % difference in nodule contrast. Evaluation of the SPRs obtained from the Monte

Carlo simulations of the tomosynthesis system [99] revealed a mean SPR of 0.18 (corresponding to a SF of 0.15) in the lung region of the phantom (Paper IV). Hence, the amount of scattering in the lung region of the phantom used in the Monte Carlo simulations corresponds to a smaller patient than the smallest patient included in the study by Jordan et al. (PA diameter 26 cm). Paper IV describes how the SPRs obtained from the Monte Carlo simulations were scaled according to the PA diameter of the patients included in the study. In the study described in Paper IV, the PA diameter of a patient was defined as the largest PA diameter over the lung region, in the lateral chest radiography images of the patients. By assuming that the relative variations in SFs, both between different areas of the lung and between different tomosynthesis projection images, are independent of patient size, the results presented by Jordan et al. for various patient sizes could be used to scale the SFs obtained from the Monte Carlo simulations according to the PA diameter of the patients included in the study. In Paper I it was shown that the relative difference in effective dose to the patient from a tomosynthesis examination when assuming that the entire exposure is delivered in the zero-degree projection, and when taking the exposure in all individual projection images into account in the dose calculation, was relatively constant for different patient sizes. This indicates that the assumption that the relative variations in SF between different tomosynthesis projection images are independent of patient size also is valid. However, the assumption that the relative variations in SFs between different areas of the lung are independent of patient size may not be completely correct due to differences in patient anatomy (e.g. the breasts of female patients). When measuring the PA diameter of the patients included in the study described in Paper IV, the breasts of the female patients were included in the measurement. Hence, patients with larger breasts had a larger PA diameter and were thereby also estimated to have higher SF. However, the variation in SF over different areas of the lung will probably also be larger for these patients.

In order to compare the sensitivity and visual appearance of the simulated nodules with those of real nodules, observer performance studies were conducted. The sensitivity of the real and simulated nodules was compared using a detection study in which the observers were instructed to detect and mark nodules in the images according to the FROC paradigm. For each mark the observers were instructed to rate both their confidence in the marking being a nodule (four-level rating scale) and their confidence in the marking being a real (not simulated) nodule (five-level rating scale). The FROC method has several benefits for the purpose of this study. First, the statistical power is much higher using FROC than ROC, and therefore a smaller number of patients were needed in the study. Second, as the purpose of the study was to compare real and simulated lesions, ROC (in which the analysis is conducted on a patient level rather than on a lesion level) would be less appropriate. Third, the use of an ROC study would technically have been more cumbersome as, preferably, only one nodule (real or simulated) should be present in each patient. However, as described in Section 6.4, FROC analysis could not be applied to the FROC data as it

was not known whether the false positive markings should be related to the group of real or simulated nodules. Instead, the rating for each threshold of the true positive markings for real and simulated nodules were plotted against each other and the ROC software ROCKIT (C. Metz, University of Chicago) was used to fit a curve to the data. Hence, if the sensitivity is the same for real and simulated nodules the curve should be a straight diagonal line, with an A_z value of 0.5. As discussed in Paper IV, the low number of nodules detected in the study may appear somewhat surprising compared to previously reported detectability and visibility of lung nodules in chest tomosynthesis [23, 27], but is probably due to the fact that thin CT slices and CAD software were used for the creation of the reference. Hence, many small nodules were detected in the clinical patient material. Based on the recommendations of the Fleischner Society [93] it can be argued that the smallest nodules should have been excluded from the study. However, as the detectability of lung nodules in tomosynthesis is relatively high compared to that in conventional chest radiography, and one of the purposes of using simulated nodules is to evaluate limitations in detectability according to nodule size, it is important to verify that the method used to simulate lung nodules in chest tomosynthesis is also valid for small nodule sizes. One may even argue that it is of greater importance for the method to be valid for small nodules than for nodules larger than 8 mm in diameter, as it has been shown that the detection for these nodule sizes in chest tomosynthesis is close to 100 % [23]. Hence, nodules of these sizes will not determine the limit for detection.

The visual appearance of the simulated nodules was evaluated by pointing out all nodules in the patient material (both real and simulated) to the observers and instructing the observers to rate their confidence for each nodule being a real nodule (not simulated). The differences in rating distributions between real and simulated nodules were analysed both qualitatively (histogram plots) and quantitatively (ROC analysis). The nodules could also have been visually evaluated using the AFC method [121]. One way of doing this would have been to show pairs of images to the observers, each pair consisting of an image containing a real nodule and an image containing a simulated nodule, and asking the observers to determine which image contained the simulated nodule (i.e. a two-alternative forced choice (2AFC) study). Alternatively, more than two images could have been presented to the observers at a time, one containing a simulated nodule and the rest containing real nodules.

The results obtained using the ROC and the 2AFC method are comparable as the area under the curve obtained from the ROC analysis is equivalent to the proportion of correct responses in a 2AFC study [121]. However, the 2AFC method has been shown to have a lower statistical power than the ROC method, for a given number of decisions (images or image pairs), while the statistical power is higher when more than two images at a time are presented to the observers in the AFC study [121]. As a lung nodule can usually be visualized in several adjacent tomosynthesis section images, using the AFC method to evaluate the visual appearance of the simulated

nodules would have been quite cumbersome as each AFC image set should consist of several image stacks, one for each of the nodules that is to be shown to the observer at the same time. The solution of only including the one section image in which the nodule is most clearly visible may have caused a loss of important information on the nodule characteristics, and would thus have reduced the benefit of using tomosynthesis for nodule detection.

The evaluation of the nodule simulation method indicated similar sensitivity for real and simulated nodules, while the results from the evaluation of the visual appearances of the nodules indicated a significant difference. The differences between the visual appearances of real and simulated nodules might partly be explained by the homogenous density of the simulated nodules. However, after the observers had completed their image evaluations, a discussion about the potential visual differences between real and simulated nodules took place. It was revealed that several of the observers used an overall assessment of the status of the patient when rating their confidence of a nodule being real. Although no proper statistical analysis was made, the data from the observer performance study also indicated that simulated nodules found in patients who also had real nodules present in the lung were more likely to be given a higher rating than simulated nodules found in patients who in reality were normal. Patients with lung nodules in the parenchyma may show other signs of disease, such as, for example, enlarged lymph nodes or pleural fluid. Hence, if the image is completely normal, the probability of finding a lung nodule is smaller. This might be needed to take into consideration when using simulated nodules to evaluate a tomosynthesis system.

7.4 Overall discussion of the work

Evaluating and optimizing medical imaging systems are important tasks for the medical physicist. The optimization of an X-ray examination should include finding a reliable relationship between image quality and exposure, and identifying the optimum radiological procedure for each specific diagnostic purpose. The first task can be achieved by investigating the change in detectability with exposure, using images acquired at different dose levels. The second can only be achieved by comparing the radiation exposure and detection of pathology using different radiological procedures. Observer performance studies using clinical images are commonly used for both these optimization tasks. However, ethical considerations may prevent the possibility to acquire clinical images at multiple exposure levels. Furthermore, it may be difficult to find clinical images that fulfil the requirements for study inclusion. The solution could be to use hybrid images, e.g. images that are simulated to be acquired at a lower exposure level or images with simulated pathology. The development of methods for creating hybrid images is complicated and time-consuming. Specific methods are often needed for different imaging modalities to obtain a high validity of the hybrid images. However, once appropriate

methods have been developed, the evaluation and optimization of a medical imaging procedure can often be performed in a more systematic and thorough manner.

Methods of evaluating an imaging system were discussed in the Introduction of this thesis, where it was mentioned that hybrid images can be a valuable complement to real, clinical images in cases where it is difficult to acquire relevant clinical images, or in cases where ethical considerations limit the use of real patients. The use of hybrid images has many benefits, but the most important is perhaps that it provides the opportunity to control the variables to be studied. Furthermore, using simulated dose reduction instead of acquiring additional clinical images has the advantage that no unnecessary exposures of real patients are required. Hence, many different exposure levels can be used in the optimization study, without exposing patients to unnecessary risks.

A thorough evaluation of the limitation in detection using chest tomosynthesis is difficult without using simulated pathology. Using real pathology, e.g. lung nodules, will introduce several biases. For example, the true size and density of the real nodules may be difficult to determine, as described in Section 7.3. In addition, nodules of the desired sizes and densities for inclusion in the study may be difficult to find in a clinical patient material, and the purpose of the study may have to be adapted according to the patient material available. Using simulated nodules provides the possibility of controlling and changing both the size and density of the nodules included in the detection study, as well as investigating whether the detectability changes with the location of the nodule in the parenchyma. In this way, a systematic and thorough evaluation of the imaging system can be carried out.

As also mentioned in the Introduction, it is important that the methods used for the creation of hybrid images result in images that have the same visible appearance of anatomical structures and the same detectability of pathology found in real clinical images. The results of a study based on hybrid images will not be valid unless the results obtained are comparable to the results that would be obtained using clinical images. The main drawback of using simulated pathology is probably the fact that reality can never be fully imitated. As pointed out in Section 7.3, observers subconsciously use an overall assessment of the patient's status to estimate the probability of the patient having a disease. Simulating pathology, e.g. lung nodules, in patients that are in reality normal, may introduce a bias due to the fact that other anatomical structures in the patient remain unchanged after the insertion of the simulated nodule.

The characteristics of lung nodules were described in Section 6.1. As can be understood from these descriptions, real lung nodules are found with a wide variety of densities, shapes and internal structures. Hence, the varieties of nodule characteristics found among real nodules are difficult to imitate in the nodule

simulation. The results of the validation study indicate that the simulated nodules, created using the method described in Papers III and IV, can be interpreted as real by radiologists. Furthermore, the sensitivity of real and simulated nodules was shown to be comparable. Despite these encouraging results, the fact that the method can only be used to simulate nodules of homogeneous density is perhaps its largest drawback. Hence, using only simulated nodules to evaluate chest tomosynthesis would not be entirely reliable. Therefore, in order to make a thorough evaluation of chest tomosynthesis, a combination of real clinical images and hybrid images should be used. By using real clinical images, the aspect of different lung nodule characteristics can be taken into account, while detailed evaluations of the limitations in the detection of lung nodules can be accomplished by the use of hybrid images.

7.5 Future work

Most studies concerned with evaluating chest tomosynthesis have until today been based on clinical images. The results of these studies have indicated that the use of tomosynthesis, instead of conventional radiography, increases the chance of detecting a lung nodule, with only a small increase in effective dose to the patient. However, in order to perform a thorough evaluation of the potential of chest tomosynthesis, the effects of nodule size, density and location in the parenchyma should be further investigated. The use of clinical images for such purposes will be associated with difficulties regarding the exact size and density of the nodules. Although these problems could be overcome, investigating the variation in detectability between different regions of the lung would still be difficult. The use of simulated nodules provides a solution to these problems as it provides unlimited control of the factors requiring investigation.

Previous studies have shown that overlapping anatomy rather than quantum noise limits the detection of pathology in conventional radiography [3-11], and as much of the obscuring anatomy is removed in a tomosynthesis section image, one may expect that it would be possible to reduce the patient exposure used in chest tomosynthesis even further, without loosing the diagnostic accuracy of the examination. The method of simulating dose reduction in tomosynthesis could be a valuable tool in investigating this possibility. By combining simulated dose reduction with simulated lung nodules, it may also be possible to investigate whether a reduction in exposure would lead to different changes in the detectability of lung nodules in different regions of the lung.

In addition to optimizing the exposure used for a tomosynthesis examination and evaluating the limitations of lung nodule detection, the optimum system configuration to use for different diagnostic questions should be evaluated. Such an evaluation should, for example, include an investigation of the effect of using different angular intervals for the collection of the tomosynthesis projection images

and the effect of using different tube voltages. Also for this evaluation the method for lung nodule simulation in tomosynthesis might be a valuable tool, as simulated nodules can be used to estimate the differences in nodule detection between various chest tomosynthesis system configurations. Furthermore, the E_{KAP} values presented in Paper I can be used to estimate the effective dose to the patients from the different tomosynthesis system configurations evaluated.

According to the Fleischner Society, all nodules larger than 4 mm in diameter should be followed up by CT after a maximum period of 6 months. As the visibility for these nodule sizes in chest tomosynthesis is comparable to CT, the question of using tomosynthesis for follow-up instead of CT has been raised. For this to be possible, two important criteria must be met: firstly, the lung nodule must be clearly visible in the chest tomosynthesis images, and secondly, it must be possible to estimate any possible changes in nodule size. Several benefits are associated with the use of simulated lung nodules for this purpose. For example, when using simulated nodules the true size of the nodule will be known exactly. Furthermore, the possibility of estimating changes in nodule size using chest tomosynthesis can be easily investigated by simply simulating nodules of increasing size. In addition, it would also be possible to investigate whether the accuracy of measured nodule size changes with nodule density or location in the parenchyma.

The evaluation of chest tomosynthesis should, of course, not only be focused on the detectability of lung nodules, but also other lung diseases. Especially patients who suffer from lung diseases that require continuous follow-up may benefit from the use of tomosynthesis. If it could be shown that the diagnostic information obtained from tomosynthesis examinations of these patients is sufficient, many of the follow-ups today carried out using CT could be replaced by tomosynthesis, thus significantly reducing the exposure of these patients. The amount of exposure needed for a tomosynthesis examination might vary depending on the diagnostic purpose of the examination, and the exposure used should be optimized for each specific diagnostic purpose. The method of simulating dose reduction in tomosynthesis will probably also be a valuable tool for this purpose

The reduction of exposure resulting from diagnostic examinations is attracting considerable interest, and much work is focused on exploring the possibilities of lowering the effective doses from common high-dose radiological examinations. For many CT examinations, the radiation exposure has been optimized according to the diagnostic purpose of each examination. It may be argued that the low-dose benefit of tomosynthesis will be overshadowed by the highly optimized CT examinations. Another possibility is however that tomosynthesis still will be a valuable complement to CT examinations in some specific situations, as the technique is cheaper and faster. The answer to these speculations will only be found by, for different radiological tasks, comparing the diagnostic outcome from a chest

tomosynthesis examination and an optimized CT examination. Apart from establishing the diagnostic value of examinations, evaluations should include comparisons of radiation exposure, examination time and financial cost. By identifying the optimal examination procedure for each patient, it can be ensured that they receive the best medical care, while resources available on the radiological department are put to the best use.

8 Summary and conclusions

In this thesis, methods developed for the evaluation and optimization of chest tomosynthesis are presented. The main conclusions of this work can be summarized as follows.

- A simplified method for estimation of the effective dose from a chest tomosynthesis examination was developed. By using the PCXMC 2.0 software, the resulting effective dose from chest tomosynthesis examinations, performed using different tomosynthesis system configurations, were determined for various patient sizes. Conversion factors between KAP and effective dose were calculated for each system configuration and patient size. Using these conversion factors the effective dose resulting from a tomosynthesis examination can be estimated by only using information of the total KAP of the examination. In addition it was found that the assumption that all the exposure in a tomosynthesis examination is delivered to the patient in the zero-degree projection results in an error of less than 10 % compared to the case when the exposure from each individual projection image is taken into account in the dose calculation.

- A method for simulating dose reduction in tomosynthesis was developed. The method is based on the creation of a noise image that can be added to an image to simulate acquisition of the image at a lower dose. By determining the NPS at different dose levels using flat-field images acquired using different levels of exposure, the NPS of the created noise image can be determined. Furthermore, by establishing the relationship between pixel value and pixel variance as a function of dose, the pixel values in the created noise image can be adjusted according to the dose variations over the image that is to be dose reduced. By adjusting the pixel values according to the pixel variation, differences in the magnitude of the DQE are taken into account, and the method was concluded to be appropriate for simulating dose reduction of tomosynthesis projection images. The method is also appropriate for performing simulated dose reductions in other digital radiographic systems where possible variations in DQE due to detector dose might be a problem.

- A method of simulating lung nodules in chest tomosynthesis was developed and evaluated. The method is based on the creation of three-dimensional artificial nodules that are inserted into the tomosynthesis projection images before reconstruction of the section images. In order to mimic reality, the signal spread in the detector, the scattered radiation and the patient motion are accounted for in the simulation process. In this way, the pixel values at the

location where the simulated nodule is inserted can be changed according to the reduction in pixel value that would have occurred if the nodule had actually been present in the patient at the time of the acquisition of the tomosynthesis projection images. The validity of the method revealed no difference in sensitivity between real and simulated nodules. It was however found that the observers graded the real nodules as slightly more realistic than the simulated nodules when judging the visual appearances of the nodules. Despite this difference the results from the present study indicate that the method for simulating nodules can be used for investigations of the limitations in detections of lung nodules in tomosynthesis section images without introducing any substantial bias compared to the clinical situation.

"Friendship," said Christopher Robin,
"is a very comforting thing to have."

-A.A. Milne

Acknowledgements

Without the help and support of my colleagues, friends and family, this thesis would never have become a reality. I wish to express my sincere gratitude to all of you.

- My principal supervisor, **Magnus Båth**. With your never-ending enthusiasm for scientific work, you have been a true inspiration to me throughout my time as a PhD student. By trying to follow your, often very insightful and clear thoughts (sometimes given to me in much less clear hand-writing), I have been forced to develop my knowledge and my scientific mind in a way I never would have managed to do on my own. Thank you for believing in me, and for giving me the opportunity to be part of the tomosynthesis research group.
- My assistant supervisor **Lars Gunnar Månsson**. Despite your busy schedule, you always found the time to answer my questions, read my manuscripts and provide me with insightful comments and thoughts. Thank you for all the encouraging words of advice you have given me during my time as a PhD student.
- My co-authors on the papers included in this thesis: **Markus Håkansson, Gustaf Ullman, Åse Allasdotter Johnsson, Jenny Vikgren, Susanne Kheddache, Marianne Boijsen, Agneta Flinck, Valeria Fisichella** and **David Molnar.** Thank you for sharing your experience and knowledge with me. Through our collaboration, I have had the opportunity to obtain basic understanding in other areas outside medical physics. I would especially like to thank **Åse** and **Jenny** for your hard work on the creation of the reference to Paper IV and for always having the time to answer my, sometimes very fuzzy, questions. Thank you also for your patience with my lack of medical knowledge when describing things from the clinical point-of-view.
- My long-term roommates **Sara Asplund** and **Kerstin Ledenius.** Thank you for all the good times, for all your support during the not so good times, and for the best company I could have whished for. **Sara**: having someone like you to share life as a PhD student with has been priceless. When feelings of anxiety and insecurity came over me you were always able to relate to them and help me feel better. **Kerstin:** by always being a few steps ahead of me in your work, you have been a never-ending source of good advice. Thank you for being patient with all my questions, and for always trying to find an answer to them.

- All my colleagues and friends at the Department of Radiation Physics, University of Gothenburg and at the Department of Medical Physics and Biomedical Engineering, Sahlgrenska University Hospital. Thank you for your good company, for all the rewarding discussions, regarding both science and life, and for all the laughter during coffee breaks (well, tea breaks for me). I am so grateful

that I have been given the opportunity to continue to have you all as my colleagues also in the future. I would especially like to thank: **Åke Cederblad, Jonny Hansson, Anne Thilander Klang, Charlotta Lundh, Patrik Sund** and **Christina Söderman,** for taking the time to read and provide valuable comments on this thesis; and **Elin Cederkrantz, Johanna Dalmo, Anders Josefsson, Maria Larsson, Mikael Montelius, Jenny Nilsson** and **Nils Rudqvist** for making the, sometimes less fun, PhD courses enjoyable. Thanks to **Niclas Pettersson** for helping me find the right perspective.

- All the people I have had the pleasure to collaborate with and who have helped me during my years as a PhD student. **Gudrun Alm Carlsson, Michael Sandborg** and **David Dance**, for co-authoring the SPIE paper on scattered radiation in chest tomosynthesis. The breast tomosynthesis research group in Malmö, **Sören Mattsson**, **Anders Tingberg, Pontus Timberg, Tony Svahn, Daniel Förnvik** and **Sophia Zackrisson**, for all the interesting discussions and exchange of experiences concerning tomosynthesis. Thank you also for your good company during both conferences and PhD courses. Thanks to **Gerhard Brunst** from GE Healthcare for your kind support and for providing valuable answers to my questions regarding the GE tomosynthesis system. Thanks also to **Sune Svensson** for your help with ViewDEX, and **Dev Chakraborty** for providing statistical advice whenever needed.
- **All my friends** who were there to help me get my mind off work any time when needed. I feel very fortunate to have you all in my life.
- **My beloved family**. Even though we live so far apart you are never more than a phone call away and always in my thoughts. I would especially like to thank my mother **Ann-Louise,** my father **Willy** and my sister **Therese** for always being there for me, for believing in me and for giving me their complete support. I am sorry I am always so far away and never able to be physically there with you during all the moments of joy and sadness that make up everyday life.
- **Erik**. For everything you are and everything you do, I love you.

This work was supported by grants from the Health and Medical Care Committee of the Region Västra Götaland, the King Gustav V Jubilee Clinic Cancer Research Foundation, the Swedish Federal Government under the LUA/ALF agreement, the Swedish Radiation Safety Authority and the Swedish Research Council.

"A quotation is a handy thing to have about,
saving one the trouble of thinking for oneself."

-A.A. Milne

References

1. Geitung, J.T., Skjaerstad, L.M., and Göthlin, J.H., *Clinical utility of chest roentgenograms.* Eur Radiol, 1999. **9**(4): p. 721-3.
2. Speets, A.M., van der Graaf, Y., Hoes, A.W., Kalmijn, S., Sachs, A.P., Rutten, M.J., Gratama, J.W., Montauban van Swijndregt, A.D., and Mali, W.P., *Chest radiography in general practice: indications, diagnostic yield and consequences for patient management.* Br J Gen Pract, 2006. **56**(529): p. 574-8.
3. Kundel, H.L., Nodine, C.F., Thickman, D., Carmody, D., and Toto, L., *Nodule detection with and without a chest image.* Invest Radiol, 1985. **20**(1): p. 94-9.
4. Bochud, F.O., Valley, J.F., Verdun, F.R., Hessler, C., and Schnyder, P., *Estimation of the noisy component of anatomical backgrounds.* Med Phys, 1999. **26**(7): p. 1365-70.
5. Samei, E., Flynn, M.J., and Eyler, W.R., *Detection of subtle lung nodules: relative influence of quantum and anatomic noise on chest radiographs.* Radiology, 1999. **213**(3): p. 727-34.
6. Burgess, A.E., Jacobson, F.L., and Judy, P.F., *Human observer detection experiments with mammograms and power-law noise.* Med Phys, 2001. **28**(4): p. 419-37.
7. Båth, M., Håkansson, M., Börjesson, S., Kheddache, S., Grahn, A., Ruschin, M., Tingberg, A., Mattsson, S., and Månsson, L.G., *Nodule detection in digital chest radiography: introduction to the RADIUS chest trial.* Radiat Prot Dosimetry, 2005. **114**(1-3): p. 85-91.
8. Båth, M., Håkansson, M., Börjesson, S., Kheddache, S., Grahn, A., Bochud, F.O., Verdun, F.R., and Månsson, L.G., *Nodule detection in digital chest radiography: part of image background acting as pure noise.* Radiat Prot Dosimetry, 2005. **114**(1-3): p. 102-8.
9. Båth, M., Håkansson, M., Börjesson, S., Hoeschen, C., Tischenko, O., Kheddache, S., Vikgren, J., and Månsson, L.G., *Nodule detection in digital chest radiography: effect of anatomical noise.* Radiat Prot Dosimetry, 2005. **114**(1-3): p. 109-13.
10. Håkansson, M., Båth, M., Börjesson, S., Kheddache, S., Grahn, A., Ruschin, M., Tingberg, A., Mattsson, S., and Månsson, L.G., *Nodule detection in digital chest radiography: summary of the RADIUS chest trial.* Radiat Prot Dosimetry, 2005. **114**(1-3): p. 114-20.
11. Tingberg, A., Båth, M., Håkansson, M., Medin, J., Besjakov, J., Sandborg, M., Alm-Carlsson, G., Mattsson, S., and Månsson, L.G., *Evaluation of image quality of lumbar spine images: a comparison between FFE and VGA.* Radiat Prot Dosimetry, 2005. **114**(1-3): p. 53-61.
12. UNSCEAR, *Medical radiation exposures, annex D, United Nations Scientific Committee on the Effects of Atomic Radiation Report to the General Assembly.* 2000, New York, USA: United Nations.
13. Shrimpton, P.C., Hillier, M.C., Lewis, M.A., and Dunn, M., *National survey of doses from CT in the UK: 2003.* Br J Radiol, 2006. **79**(948): p. 968-80.

14. Martin, C.J., *Radiation dosimetry for diagnostic medical exposures.* Radiat Prot Dosimetry, 2008. **128**(4): p. 389-412.
15. ICRP, *ICRP Publication 103: The 2007 Recommendations of the International Commission on Radiological Protection*. Annals of the ICRP, 2007. **37**(2-4), Oxford UK: Elsevier Ltd.
16. Webb, S., *From the watching of shadows - the origins of radiological tomography*, ed. A.J. Meadows. 1990, Bristol and New York: Adam Hilger
17. Ziedses des Plantes, B.G., *Eine neue methode zur differenzierung in der roentgenographie (planigraphie).* Acta Radiol, 1932. **13**: p. 182-92.
18. Ziedses des Plantes, B.G., *Planigraphy, a röntgenographic differentiation method. Doctoral thesis*. 1934, Utrecht: Kemmink Utrecht.
19. Garrison, J.B., Grant, D.G., Guier, W.H., and Johns, R.J., *Three dimensional roentgenography.* Am J Roentgenology, 1969. **105**: p. 903-8.
20. Miller, E.R., McCurry, E.M., and Hruska, B., *An infinite number of laminagrams from a finite number of radiographs.* Radiology, 1971. **98**: p. 249-55.
21. Grant, D.G., *Tomosynthesis: A three-dimensional radiographic imaging technique.* IEEE Trans Biomed Eng, 1972. **19**: p. 20-8.
22. Dobbins III, J.T. and Godfrey, D.J., *Digital x-ray tomosynthesis: current state of the art and clinical potential.* Phys Med Biol, 2003. **48**(19): p. R65-106.
23. Vikgren, J., Zachrisson, S., Svalkvist, A., Johnsson, Å.A., Boijsen, M., Flinck, A., Kheddache, S., and Båth, M., *Comparison of chest tomosynthesis and chest radiography for detection of pulmonary nodules: human observer study of clinical cases.* Radiology, 2008. **249**(3): p. 1034-41.
24. Quaia, E., Baratella, E., Cioffi, V., Bregant, P., Cernic, S., Cuttin, R., and Cova, M.A., *The value of digital tomosynthesis in the diagnosis of suspected pulmonary lesions on chest radiography: analysis of diagnostic accuracy and confidence.* Acad Radiol, 2010. **17**(10): p. 1267-74.
25. Kim, E.Y., Chung, M.J., Lee, H.Y., Koh, W.J., Jung, H.N., and Lee, K.S., *Pulmonary mycobacterial disease: diagnostic performance of low-dose digital tomosynthesis as compared with chest radiography.* Radiology, 2010. **257**(1): p. 269-77.
26. Jung, H.N., Chung, M.J., Koo, J.H., Kim, H.C., and Lee, K.S., *Digital tomosynthesis of the chest: Utility for detection of lung metastasis in patients with colorectal cancer.* Clin Radiol, 2011(doi: 10.1016/j.crad.2011.08.017).
27. Dobbins III, J.T., McAdams, H.P., Song, J.W., Li, C.M., Godfrey, D.J., Delong, D., Paik, D., and Martinez-Jimenez, S., *Digital tomosynthesis of the chest for lung nodule detection: interim sensitivity results from an ongoing NIH-sponsored trial.* Med Phys, 2008. **35**: p. 2554-7.
28. Yamada, Y., Jinzaki, M., Hasegawa, I., Shiomi, E., Sugiura, H., Abe, T., Sato, Y., Kuribayashi, S., and Ogawa, K., *Fast scanning tomosynthesis for the detection of pulmonary nodules: diagnostic performance compared with chest radiography, using multidetector-row computed tomography as the reference.* Invest Radiol, 2011. **46**(8): p. 471-7.
29. Zachrisson, S., Vikgren, J., Svalkvist, A., Johnsson, Å.A., Boijsen, M., Flinck, A., Månsson, L.G., Kheddache, S., and Båth, M., *Effect of clinical experience of chest tomosynthesis on detection of pulmonary nodules.* Acta Radiol, 2009. **50**(8): p. 884-91.

30. Asplund, S., Johnsson, Å.A., Vikgren, J., Svalkvist, A., Boijsen, M., Fisichella, V., Flinck, A., Wiksell, A., Ivarsson, J., Rystedt, H., Månsson, L.G., Kheddache, S., and Båth, M., *Learning aspects and potential pitfalls regarding detection of pulmonary nodules in chest tomosynthesis and proposed related quality criteria.* Acta Radiol, 2011. **52**(5): p. 503-12.
31. Johnsson, Å.A., Svalkvist, A., Vikgren, J., Boijsen, M., Flinck, A., Kheddache, S., and Båth, M., *A phantom study of nodule size evaluation with chest tomosynthesis and computed tomography.* Radiat Prot Dosimetry, 2010. **139**(1-3): p. 140-3.
32. Sabol, J.M., *A Monte Carlo estimation of effective dose in chest tomosynthesis.* Med Phys, 2009. **32**(12): p. 5480-7.
33. Båth, M., Svalkvist, A., Wrangel, A.V., Ohlsson, H.R., and Cederblad, Å., *Effective dose to patients from chest examinations with tomosynthesis.* Radiat Prot Dosimetry, 2009. **139**(1-3): p. 153-8.
34. Dobbins III, J.T., McAdams, H.P., Godfrey, D.J., and Li, C.M., *Digital tomosynthesis of the chest.* J Thorac Imaging, 2008. **23**(2): p. 86-92.
35. Dobbins III, J.T. and McAdams, H.P., *Chest tomosynthesis: technical principles and clinical update.* Eur J Radiol, 2009. **72**(2): p. 244-51.
36. Dobbins III, J.T., *Tomosynthesis imaging: at a translational crossroads.* Med Phys, 2009. **36**(6): p. 1956-67.
37. Johnsson, Å.A., Vikgren, J., Svalkvist, A., Zachrisson, S., Flinck, A., Boijsen, M., Kheddache, S., Månsson, L.G., and Båth, M., *Overview of two years of clinical experience of chest tomosynthesis at Sahlgrenska University Hospital.* Radiat Prot Dosimetry, 2010. **139**(1-3): p. 124-9.
38. Svahn, T., Ruschin, M., Hemdal, B., Nyhlén, L., Andersson, I., Timberg, P., Mattsson, S., and Tingberg, A., *In-plane artifacts in breast tomosynthesis quantified with a novel contrast-detail phantom.* Proc SPIE, 2007. **6510**: p. 65104R.1-12
39. Dainty, J.C. and Shaw, R., *Image science - Principles, analysis and evaluation of photographic-type imaging processes*. 1974, London: Academic Press.
40. Sund, P., Båth, M., Kheddache, S., and Månsson, L.G., *Comparison of visual grading analysis and determination of detective quantum efficiency for evaluating system performance in digital chest radiography.* Eur Radiol, 2004. **14**(1): p. 48-58.
41. Båth, M., *Evaluating imaging systems: practical applications.* Radiat Prot Dosimetry, 2010. **139**(1-3): p. 26-36.
42. Burgess, A.E., *Visual perception studies and observer models in medical imaging.* Semin Nucl Med, 2011. **41**(6): p. 419-36.
43. Metz, C.E., Wagner, R.F., Doi, K., Brown, D.G., Nishikawa, R.M., and Myers, K.J., *Toward consensus on quantitative assessment of medical imaging systems.* Med Phys, 1995. **22**(7): p. 1057-61.
44. Båth, M., Håkansson, M., Hansson, J., and Månsson, L.G., *A conceptual optimization strategy for radiography in a digital environment.* Radiat Prot Dosimetry, 2005. **114**(1-3): p. 230-35.
45. Kroft, L.J., Veldkamp, W.J., Mertens, B.J., van Delft, J.P., and Geleijns, J., *Detection of simulated nodules on clinical radiographs: dose reduction at digital posteroanterior chest radiography.* Radiology, 2006. **241**(2): p. 392-8.

46. Ruschin, M., Timberg, P., Båth, M., Hemdal, B., Svahn, T., Saunders, R.S., Samei, E., Andersson, I., Mattsson, S., Chakraborty, D.P., and Tingberg, A., *Dose dependence of mass and microcalcification detection in digital mammography: free response human observer studies.* Med Phys, 2007. **34**(2): p. 400-7.
47. Ledenius, K., Gustavsson, M., Johansson, S., Stålhammar, F., Wiklund, L.M., and Thilander-Klang, A., *Effect of tube current on diagnostic image quality in paediatric cerebral multidetector CT images.* Br J Radiol, 2009. **82**(976): p. 313-20.
48. Hart, D., Jones, D.G., and Wall, B.F., *Estimation of Effective Dose in Diagnostic Radiology from Entrance Surface Dose and Dose-Area Product Measurements*. 1994, National Radiological Protection Board, NRPB-R262.
49. Huda, W., Ogden, K.M., and Khorasani, M.R., *Converting dose-length product to effective dose at CT.* Radiology, 2008. **248**(3): p. 995-1003.
50. Saunders, R.S. and Samei, E., *A method for modifying the image quality parameters of digital radiographic images.* Med Phys, 2003. **30**(11): p. 3006-17.
51. Båth, M., Håkansson, M., Tingberg, A., and Månsson, L.G., *Method of simulating dose reduction for digital radiographic systems.* Radiat Prot Dosimetry, 2005. **114**(1-3): p. 253-9.
52. Veldkamp, W.J., Kroft, L.J., van Delft, J.P., and Geleijns, J., *A Technique for Simulating the Effect of Dose Reduction on Image Quality in Digital Chest Radiography.* J Digit Imaging, 2008. **22**(2): p. 114-25.
53. Mayo, J.R., Whittall, K.P., Leung, A.N., Hartman, T.E., Park, C.S., Primack, S.L., Chambers, G.K., Limkeman, M.K., Toth, T.L., and Fox, S.H., *Simulated dose reduction in conventional chest CT: validation study.* Radiology, 1997. **202**(2): p. 453-7.
54. Sennst, D.A., Kachelriess, M., Leidecker, C., Schmidt, B., Watzke, O., and Kalender, W.A., *An extensible software-based platform for reconstruction and evaluation of CT images.* Radiographics, 2004. **24**(2): p. 601-13.
55. Britten, A.J., Crotty, M., Kiremidjian, H., Grundy, A., and Adam, E.J., *The addition of computer simulated noise to investigate radiation dose and image quality in images with spatial correlation of statistical noise: an example application to X-ray CT of the brain.* Br J Radiol, 2004. **77**(916): p. 323-8.
56. Li, X., Samei, E., DeLong, D.M., Jones, R.P., Gaca, A.M., Hollingsworth, C.L., Maxfield, C.M., Colsher, J.G., and Frush, D.P., *Pediatric MDCT: towards assessing the diagnostic influence of dose reduction on the detection of small lung nodules.* Acad Radiol, 2009. **16**(7): p. 872-80.
57. Massoumzadeh, P., Don, S., Hildebolt, C.F., Bae, K.T., and Whiting, B.R., *Validation of CT dose-reduction simulation.* Med Phys, 2009. **36**(1): p. 174-89.
58. Samei, E., Flynn, M.J., and Eyler, W.R., *Simulation of subtle lung nodules in projection chest radiography.* Radiology, 1997. **202**(1): p. 117-24.
59. Li, X., Samei, E., Delong, D.M., Jones, R.P., Gaca, A.M., Hollingsworth, C.L., Maxfield, C.M., Carrico, C.W., and Frush, D.P., *Three-dimensional simulation of lung nodules for paediatric multidetector array CT.* Br J Radiol, 2009. **82**(977): p. 401-11.
60. Sun, S., Rubin, G.D., Paik, D., Steiner, R.M., Zhuge, F., and Napel, S., *Registration of lung nodules using a semi-rigid model: method and preliminary results.* Med Phys, 2007. **34**(2): p. 613-26.

61. ICRU, *ICRU report 60 - Fundamental Quantities and units for ionizing radiation*. Journal of the ICRU. 1998, Maryland, USA: International Commission on Radiation Units and Measurements.
62. IAEA, *Dosimetry in diagnostic radiology: an international code of practice*, in *Technical Report Series No. 457*. 2007, Vienna, Austria: International Atomic Energy Agency.
63. ICRU, *ICRU Report 74: Patient dosimetry for x rays used in medical imaging*. Journal of the ICRU. 2005, Maryland, USA: International Commission on Radiation Units and Measurements.
64. ICRP, *ICRP Publication 26: Recommendations of the International Commission on Radiological Protection*. Annals of the ICRP, 1977. **1**(3), Oxford, UK: Pergamon Press.
65. ICRP, *ICRP Publication 60: 1990 Recommendations of the International Commission on Radiological Protection*. Annals of the ICRP, 1991. **21**(1-3), Oxford UK: Pergamon Press.
66. Johansson, L., *Hormesis, an update of the present position.* Eur J Nucl Med Mol Imaging, 2003. **30**(6): p. 921-33.
67. Preston, D.L., Cullings, H., Suyama, A., Funamoto, S., Nishi, N., Soda, M., Mabuchi, K., Kodama, K., Kasagi, F., and Shore, R.E., *Solid cancer incidence in atomic bomb survivors exposed in utero or as young children.* J Natl Cancer Inst, 2008. **100**(6): p. 428-36.
68. ICRP, *ICRP Publication 89: Basic anatomical and physiological data for use in radiological protection: Reference values.* Annals of the ICRP, 2002. **32**(3-4), Oxford, UK: Pergamon Press.
69. Zankl, M., Eckerman, K.F., and Bolch, W.E., *Voxel-based models representing the male and female ICRP reference adult--the skeleton.* Radiat Prot Dosimetry, 2007. **127**(1-4): p. 174-86.
70. Tapiovaara, M., Lakkisto, M., and Servomaa, A., *A PC-based Monte Carlo program for calculating patient doses in medical X-ray examinations*, in *STUK-A139*. 1997, Helsinki, Finland: STUK.
71. Tapiovaara, M. and Siiskonen, T., *PCXMC - A Monte Carlo program for calculating patient doses in medical x-ray examinations (2nd Ed.)*, in *STUK-A231*. 2008, Helsinki, Finland: STUK.
72. Cristy, M. and Eckerman, K.F., *Specific absorbed fractions of energy at various ages from internal photon sources. I. Methods*. 1987, Oak Ridge, Tennessee: Oak Ridge National Laboratiory.
73. Eckerman, K.F. and Cristy, M., *Federal Guidance report no. 12 - External exposure to radionuclides in air, water and soil*. 1993, Oak Ridge, Tennessee: Oak Ridge National Laboratory.
74. Cristy, M., *Mathematical phantoms representing children of various ages for use in estimates of internal dose, NUREG/CR-1159, ORNL/NUREG/TM-367.* 1980, Oak Ridge, Tennessee: Oak Ridge National Laboratory.
75. Saxeböl, G., Olerud, H.M., Hjardemaal, O., Leitz, W., Servomaa, A., and Walderhaug, T., *Nordic guidance levels for patient doses in diagnostic radiology. Report on Nordic radiation protection co-operation No. 5*. 1996, Østerås, Norway:

The radiation protection and nuclear safety authorities in Denmark, Finland, Iceland, Norway and Sweden.

76. Li, C.M. and Dobbins III, J.T., *Methodology for determining dose reduction for chest tomosynthesis.* Proc SPIE, 2007. **6510**: p. 65102D.1-10.
77. Söderberg, M., Gunnarsson, M., and Nilsson, M., *Simulated dose reduction by adding artificial noise to measured raw data: a validation study.* Radiat Prot Dosimetry, 2010. **139**(1-3): p. 71-7.
78. Båth, M., Sund, P., and Månsson, L.G., *Evaluation of the imaging properties of two generations of a CCD-based system for digital chest radiography.* Med Phys, 2002. **29**(10): p. 2286-97.
79. Illers, H., Buhr, E., and Hoeschen, C., *Measurement of the detective quantum efficiency (DQE) of digital X-ray detectors according to the novel standard IEC 62220-1.* Radiat Prot Dosimetry, 2005. **114**(1-3): p. 39-44.
80. Cunningham, I.A., *Applied Linear-Systems Theory*, in *Handbook of Medical Imaging*, J. Beutel, H.L. Kundel, and R.L. Van Metter, Editors. 2000, Bellingham, USA: SPIE Press. p. 79-162.
81. James, J.F., *A Student's Guide to Fourier Transforms - With Applications in Physics and Engineering*. 2nd ed. 2002, New York: Cambridge University Press.
82. Dobbins III, J.T., *Image Quality Metrics for Digital Systems*, in *Handbook of Medical Imaging*, J. Beutel, H.L. Kundel, and R.L. Van Metter, Editors. 2000, Bellingham, USA: SPIE Press. p. 161-222.
83. Dobbins III, J.T., *Effects of undersampling on the proper interpretation of modulation transfer function, noise power spectra, and noise equivalent quanta of digital imaging systems.* Med Phys, 1995. **22**(2): p. 171-81.
84. Erasmus, J.J., Connolly, J.E., McAdams, H.P., and Roggli, V.L., *Solitary pulmonary nodules: Part I. Morphologic evaluation for differentiation of benign and malignant lesions.* Radiographics, 2000. **20**(1): p. 43-58.
85. Tang, A.W., Moss, H.A., and Robertson, R.J., *The solitary pulmonary nodule.* Eur J Radiol, 2003. **45**(1): p. 69-77.
86. Wormanns, D. and Diederich, S., *Characterization of small pulmonary nodules by CT.* Eur Radiol, 2004. **14**(8): p. 1380-91.
87. Winer-Muram, H.T., *The solitary pulmonary nodule.* Radiology, 2006. **239**(1): p. 34-49.
88. Brandman, S. and Ko, J.P., *Pulmonary nodule detection, characterization, and management with multidetector computed tomography.* J Thorac Imaging, 2011. **26**(2): p. 90-105.
89. Gould, M.K., Fletcher, J., Iannettoni, M.D., Lynch, W.R., Midthun, D.E., Naidich, D.P., and Ost, D.E., *Evaluation of patients with pulmonary nodules: when is it lung cancer?: ACCP evidence-based clinical practice guidelines (2nd edition).* Chest, 2007. **132** (3 Suppl): p. 108S-130S.
90. Wahidi, M.M., Govert, J.A., Goudar, R.K., Gould, M.K., and McCrory, D.C., *Evidence for the treatment of patients with pulmonary nodules: when is it lung cancer?: ACCP evidence-based clinical practice guidelines (2nd edition).* Chest, 2007. **132** (3 Suppl): p. 94S-107S.
91. Henschke, C.I., Yankelevitz, D.F., Mirtcheva, R., McGuinness, G., McCauley, D., and Miettinen, O.S., *CT screening for lung cancer: frequency and significance of part-solid and nonsolid nodules.* AJR Am J Roentgenol, 2002. **178**(5): p. 1053-7.

92. Grewal, R.G. and Austin, J.H., *CT demonstration of calcification in carcinoma of the lung.* J Comput Assist Tomogr, 1994. **18**(6): p. 867-71.
93. MacMahon, H., Austin, J.H., Gamsu, G., Herold, C.J., Jett, J.R., Naidich, D.P., Patz, E.F., Jr., and Swensen, S.J., *Guidelines for management of small pulmonary nodules detected on CT scans: a statement from the Fleischner Society.* Radiology, 2005. **237**(2): p. 395-400.
94. Niklason, L.T., Sorenson, J.A., and Nelson, J.A., *Scattered radiation in chest radiography.* Med Phys, 1981. **8**(5): p. 677-81.
95. Floyd, C.E., Jr., Baker, J.A., Lo, J.Y., and Ravin, C.E., *Posterior beam-stop method for scatter fraction measurement in digital radiography.* Invest Radiol, 1992. **27**(2): p. 119-23.
96. Jordan, L.K., 3rd, Floyd, C.E., Jr., Lo, J.Y., and Ravin, C.E., *Measurement of scatter fractions in erect posteroanterior and lateral chest radiography.* Radiology, 1993. **188**(1): p. 215-8.
97. Ullman, G., Sandborg, M., Dance, D.R., Hunt, R., and Alm Carlsson, G., *Distributions of scatter-to-primary and signal-to-noise ratios per pixel in digital chest imaging.* Radiat Prot Dosimetry, 2005. **114**(1-3): p. 355-8.
98. Wolbarst, A.B., *Physics of Radiology*, ed. E. Ryan. 1993, Norwalk, Connecticut: Appleton & Lange.
99. Ullman, G., Dance, D.R., Sandborg, M., Carlsson, G.A., Svalkvist, A., and Båth, M., *A Monte Carlo-based model for simulation of digital chest tomosynthesis.* Radiat Prot Dosimetry, 2010. **139**(1-3): p. 159-63.
100. Svalkvist, A., Ullman, G., Håkansson, M., Dance, D.R., Sandborg, M., Carlsson, G.A., and Båth, M., *Investigation of the effect of varying scatter-to-primary ratios on nodule contrast in chest tomosynthesis.* Proc SPIE, 2011. **7961**: p. 79615Y.1-10.
101. Fujita, H., Tsai, D.Y., Itoh, T., Doi, K., Morishita, J., Ueda, K., and Ohtsuka, A., *A simple method for determining the modulation transfer function in digital radiography.* IEEE Trans Med Imaging, 1992. **11**(1): p. 34-9.
102. Samei, E., Flynn, M.J., and Reimann, D.A., *A method for measuring the presampled MTF of digital radiographic systems using an edge test device.* Med Phys, 1998. **25**(1): p. 102-13.
103. IEC, *Medical electrical equipment - Characteristics of digital X-ray imaging devices - Part 1: Determination of the detective quantum efficiency. Document no. 62220-1.* 2003, Geneva, Switzerland: International Electrotechnical Commission.
104. Dobbins III, J.T., Ergun, D.L., Rutz, L., Hinshaw, D.A., Blume, H., and Clark, D.C., *DQE(f) of four generations of computed radiography acquisition devices.* Med Phys, 1995. **22**(10): p. 1581-93.
105. Samei, E. and Flynn, M.J., *An experimental comparison of detector performance for direct and indirect digital radiography systems.* Med Phys, 2003. **30**(4): p. 608-22.
106. Chakraborty, D.P., *New developments in observer performance methodology in medical imaging.* Semin Nucl Med, 2011. **41**(6): p. 401-18.
107. Bunch, P.C., Hamilton, J.F., Sanderson, G.K., and Simmons, A.H., *A free-response approach to the measurement and characterization of radiographic-observer performance.* J Appl Photog Eng, 1978. **4**: p. 166-71.
108. Burgess, A.E., Xing, L., and Abbey, C.K., *Nodule detection in two component noise: toward patient structure.* Proc SPIE, 1997. **3036**: p. 2-13.

109. Samei, E., Flynn, M.J., Beute, G.H., and Peterson, E., *Comparison of observer performance for real and simulated nodules in chest radiography.* Proc SPIE, 1996. **2712**: p. 60-70.
110. Karadi, C., Beaulieu, C.F., Jeffrey, R.B., Jr., Paik, D.S., and Napel, S., *Display modes for CT colonography. Part I. Synthesis and insertion of polyps into patient CT data.* Radiology, 1999. **212**(1): p. 195-201.
111. Hsieh, J., *Computed tomography - Principles, design, artifacts and recent advances.* 2nd ed. 2009, Hoboken, USA: Wiley-Interscience.
112. Ullman, G., Sandborg, M., Dance, D.G., Hunt, R., and Carlsson, G.A., *Distributions of scatter-to-primary ratios in chest PA radiography using grid or air gap for scatter-rejection.* 2004, Linköping, Sweden: Department of medicine and Care, Depatment of Radiation Physics, Faculty of Health Sciences.
113. Börjesson, S., Håkansson, M., Båth, M., Kheddache, S., Svensson, S., Tingberg, A., Grahn, A., Ruschin, M., Hemdal, B., Mattsson, S., and Månsson, L.G., *A software tool for increased efficiency in observer performance studies in radiology.* Radiat Prot Dosimetry, 2005. **114**(1-3): p. 45-52.
114. Håkansson, M., Svensson, S., Zachrisson, S., Svalkvist, A., Båth, M., and Månsson, L.G., *ViewDEX: an efficient and easy-to-use software for observer performance studies.* Radiat Prot Dosimetry, 2010. **139**(1-3): p. 42-51.
115. Schlattl, H., Zankl, M., and Petoussi-Henss, N., *Organ dose conversion coefficients for voxel models of the reference male and female from idealized photon exposures.* Phys Med Biol, 2007. **52**(8): p. 2123-45.
116. Cranley, K., Gilmore, B.J., Fogarty, G.W.A., and Desponds, L., eds. *IPEM Report 78: Catalogue of diagnostic x-ray spectra and other data.* 1997: York, UK: The Institute of Physics and Engineering in Medicine.
117. Borras, C., Huda, W., and Orton, C.G., *Point/counterpoint. The use of effective dose for medical procedures is inappropriate.* Med Phys, 2010. **37**(7): p. 3497-500.
118. ICRP, *ICRP Publication 105: Radiation Protection in Medicine.* Annals of the ICRP, 2007. **37**(6), Oxford, UK: Elsevier Ltd.
119. Pauls, S., Kurschner, C., Dharaiya, E., Muche, R., Schmidt, S.A., Kruger, S., Brambs, H.J., and Aschoff, A.J., *Comparison of manual and automated size measurements of lung metastases on MDCT images: potential influence on therapeutic decisions.* Eur J Radiol, 2008. **66**(1): p. 19-26.
120. Gavrielides, M.A., Kinnard, L.M., Myers, K.J., and Petrick, N., *Noncalcified lung nodules: volumetric assessment with thoracic CT.* Radiology, 2009. **251**(1): p. 26-37.
121. Burgess, A.E., *Comparison of receiver operating characteristic and forced choice observer performance measurement methods.* Med Phys, 1995. **22**(5): p. 643-55.